



PhD THESIS

Development of temporally correlated photon pair sources

Csaba Tamás Holló

Supervisor: Gábor Erdei PhD,
associate professor
BME Institute of Physics
Department of Atomic Physics

BMEatomfizika

2025

Table of contents

1	Introduction	5
2	Former results related to photon pair sources	7
3	Theses	9
4	Theoretical background	10
4.1	Parametric down-conversion	10
4.2	Phase matching.....	11
4.2.1	Birefringent Phase Matching (BPM)	11
4.2.2	Quasi-Phase Matching (QPM).....	14
4.2.3	Factors influencing phase matching.....	16
4.3	Photon state description, entanglement	18
4.4	Implementation of polarization-state tomography.....	20
4.5	Characteristics of single-mode fibers	21
4.6	Components of the measurement apparatus	22
4.6.1	Single-photon detection	22
4.6.2	Time tagging and coincidence counting	23
4.6.3	Polarization optics	24
5	Compact single-mode fiber-coupled photon pair source	26
5.1	Design of the optical system	26
5.2	Maximizing fiber-coupling efficiency for SPDC light.....	28
5.3	Elimination of pump photon-related coincidences.....	32
5.4	Physical implementation and opto-mechanical alignment.....	34
5.5	Measured source performance	38
5.6	Summary and Thesis 1.....	42
6	Conversion of transverse momentum correlation into polarization entanglement	44
6.1	Presentation of the physical concept.....	45
6.2	Experimental setup	47
6.2.1	Segmented Half-Wave Plates.....	48
6.2.2	Polarization Control	49
6.3	Alignment process.....	51
6.4	Measured source performance	52
6.5	Summary and Thesis 2.....	55

7	Phase-tunable inverse Hong-Ou-Mandel interference for photon pair separation	56
7.1	Description of the concept.....	56
7.2	Phase tuning via dispersion.....	58
7.3	Adjustment process and experimental results	61
7.4	Summary and Thesis 3.....	64
8	Polarization entanglement utilizing inverse HOM interference	65
8.1	Working principles	65
8.2	Experimental demonstration	68
8.3	Potential possibilities for improvement	70
8.4	Summary and Thesis 4.....	71
9	Conclusions	72
	Acknowledgement	73
	References	74
10	Appendix	80
10.1	Probabilities computed with Poissonian distribution	80
10.2	Parallel beam shift of tilted glass plate	81
10.3	Transforming fitting function parameters	83
10.4	Manufacturing drawings.....	84

1 Introduction

The rapidly evolving fields of telecommunications and information processing broadly utilize technologies based on both classical and quantum optical solutions. Several data transfer protocols and computational schemes have been proposed, many already tested, using individual photons as bits of information. Two notable application areas are: 1) quantum key distribution, which is a prospective way of secure data transmission [1][2], and 2) all-optical quantum computing [3], that is believed to provide a solution to enigmatic problems, such as factorization to primes. The temporal correlation of specific photon states, widely known as entanglement, is a fundamental basis of the underlying technologies, such as quantum state teleportation [4] or repetition [5].

Systems serving any of the previous purposes require an appropriate source of single photons or correlated photon pairs. Such devices can be realized via different approaches, each having strengths and weaknesses. Some rely on spontaneous emission of isolated two-level systems, such as atoms [6], molecules [7], or quantum dots [8], excited with electrical or optical pulses. Though these provide photons on demand, the achievable flux (i.e., the total number of photons over the beam cross section per unit time) is quite limited. Another type utilizes spontaneous parametric down-conversion (SPDC) occurring in highly nonlinear optical materials, such as β -barium borate (BBO) [9], whereby a high-energy pump photon splits into a pair of lower energy ones. These so-called signal and idler photons exhibit temporally correlated properties: energy and momentum entanglement are inherent due to conservation laws, and in case the circumstances of their generation are carefully selected, polarization entanglement is also realizable [10]. Since the arrival moment of a signal photon is heralded by the coincident detection of its idler, SPDC is often used for single-photon generation too [11].

For the above purposes alternative solutions exist both in the literature and in the form of industrial products [12]-[14]. They share common drawbacks, such as low level of integration, instability, sensitivity to environmental effects, lack of modularity, complicated setup, long and awkward alignment process. In addition, most industrial and laboratory applications require photons to be coupled into single-mode fibers, which poses further challenges in terms of coupling efficiency.

The Department of Atomic Physics took part in the HunQuTech (National Quantum Technology Program) project and is a contributor to the still ongoing QNL (Quantum Information National Laboratory Hungary) program for the study and development of quantum optical processes and technologies. My research centers on the design and optimization of SPDC sources to address these issues. In collaboration with colleagues of the quantum optics research team at the Department, I aimed to develop solutions to as many of the aforementioned challenges as possible. I investigated various nonlinear materials and source configurations to identify optimal operational parameters. Modularity and flexibility were key priorities, enabling easy transitions between operational modes to support diverse experimental and educational

applications. Portability was another focus, ensuring the sources could be utilized beyond the confines of the laboratory.

Beyond overcoming technical obstacles, my work also emphasizes the development of novel principles for photon source operation. This thesis presents the design schematics and underlying physics of each source, along with detailed descriptions of alignment procedures. By integrating practical improvements with theoretical advancements, the goal is to contribute versatile and high-performance photon sources to the expanding field of quantum optics.

My thesis begins with a concise theoretical overview of the fundamental physics required to understand the operation of SPDC sources. This is followed by a brief literature review summarizing the most relevant developments and results in the field. The core of the thesis is dedicated to the design and implementation of the SPDC sources I have developed. This section is structured around the motivation for each design goal, followed by a detailed account of the successive steps taken towards their realization and performance optimization. Emphasis is placed on the iterative nature of the development process, highlighting both the challenges encountered and the solutions devised.

2 Former results related to photon pair sources

The generation of polarization-entangled photon pairs via SPDC has been standing as a cornerstone of experimental quantum optics, quantum information processing, and quantum communication since the end of the 20th century. The unique correlations exhibited by these photon pairs are fundamental to realizing protocols such as quantum key distribution [1][32], quantum teleportation [4], and foundational tests of quantum mechanics [33]. SPDC taking place in nonlinear crystals became the dominant method due to its relative simplicity and the high quality of entanglement achievable [34][35].

Several configurations for generating polarization-entangled states using SPDC are well-established. One of the oldest utilizes type-II phase matching, where entangled pairs can be extracted from the overlapping orthogonally polarized down-converted beams [34].

A popular and robust method involved using two thin, orthogonally oriented type-I phase-matched crystals [24][35]. A pump photon could down-convert in either the first crystal (e.g., producing horizontally polarized pairs) or the second (producing vertically polarized pairs). If these two possibilities are indistinguishable, a polarization-entangled state is formed. This scheme was valued for its high fidelity and brightness.

For practical applications, especially those requiring fiber coupling, collinear generation (where signal, idler, and often the pump travel along the same path) was highly desirable. Separating the entangled pair from the strong pump beam was a key technical challenge in these setups, often addressed with dichroic mirrors and filters.

To enhance stability and compactness, Sagnac interferometer-based SPDC sources gained significant attention [36][37]. In these configurations, the pump beam traverses a nonlinear crystal (or crystals) in both clockwise and counter-clockwise directions. The counter-propagating down-converted pairs are then coherently superimposed at a polarizing beam splitter, producing entanglement. The inherent common-path nature of Sagnac interferometers provides excellent passive stability against thermal fluctuations and mechanical vibrations, addressing a major drawback of earlier sources.

The invent of periodically-poled nonlinear crystals, such as ppKTP or ppLN, became increasingly prevalent. QPM in these materials allowed for the use of higher nonlinear coefficients, leading to significantly higher pair generation rates for a given pump power and crystal length. ppKTP, in particular, was used for bright, collinear, Type-II SPDC sources of polarization entanglement [38][39].

Since the initial demonstrations, a wide variety of polarization-entangled photon pair sources has been developed to address different experimental and practical demands. These include interferometric configurations for enhanced stability and phase control [30][40], sources operating at telecommunication wavelengths for fiber-based quantum networks [31], and designs optimized for deployment in space environments [41]. Pulsed pump implementations have been introduced to improve timing resolution and enable synchronization with other quantum systems [42], while all-fiber-based architectures offer compact, robust, and alignment-free operation[43].

These sources have been successfully applied in experimental quantum key distribution field trials, including terrestrial free-space links [44], long-distance optical fiber channels [45][46], and satellite-to-ground communication scenarios [47][48], demonstrating the viability of entanglement-based quantum key distribution under real-world conditions. The development of such sources and their applications continues to progress through national initiatives and international collaborations, aiming to enhance their efficiency, stability, and integration into future quantum communication networks.

With the present work, I aim to contribute to the ongoing development of entangled photon sources by expanding the range of available implementations and proposing novel design solutions. My goal is to support the advancement of platforms for future quantum communication technologies.

3 Theses

Below I summarize my theses as the core messages and main achievement of this work:

- 1) I designed and built a compact, portable, single-mode fiber-coupled correlated photon pair source based on noncollinear, frequency-degenerate spontaneous parametric down-conversion utilizing critical type-I phase matching, that has a higher photon pair flux ($1.3 \cdot 10^5$ pairs/s/mW), and a larger bandwidth (202 nm) compared to sources of similar approach. [H1],[H2],[H3]
- 2) I proposed a method for converting the transverse momentum correlation of photon pairs into polarization entanglement by using wavefront-splitting interference and single-mode fibers, demonstrated the operation of the technique by incorporating it into the photon pair source presented in Thesis 1) and validated the method by determining state fidelity yielding $F = 0.95$. [H4]
- 3) For the phase tuning of inverse Hong-Ou-Mandel interference in a Sagnac loop I proposed a simple and reliable method based on the wavelength dispersion of optical glass, described its theoretical background and experimentally demonstrated the effect in a custom-built photon pair source by using it for the separation of frequency-degenerate correlated photon pairs. [H5]
- 4) I described an approach to implement polarization entanglement with two, consecutively placed type-0 collinearly phase-matched nonlinear crystals in a Sagnac interferometer without the need of (dual-wavelength) polarization optics utilizing the inverse Hong-Ou-Mandel effect, and experimentally demonstrated its operation by tuning the source of Thesis 3) to produce a Bell state with $F = 0.914$ fidelity. [H5]

4 Theoretical background

All the theories and effects collected in this chapter are well described in the referenced literature, therefore I will only give a short overview to summarize the necessary concepts I have used in the following description of my work. Throughout this dissertation I will use the term “photon” in the sense of a certain discrete energy quantity of light. A propagating photon in free space or in a material can be best imagined as an impulse of electromagnetic radiation with a finite temporal length corresponding to the coherence time, the overall energy of which equals $\hbar\omega$ integrated for the entire pulse, where ω denotes the mean angular frequency. The point-like detection of a photon is random within its coherence time.

4.1 Parametric down-conversion

During my PhD, I studied and utilized spontaneous parametric down-conversion, a quantum optical process occurring in nonlinear crystals when a strong pump beam propagates through them [9]. In SPDC, pump photons are split into two lower-energy photons, termed the signal and idler photons. This process is conceptually similar to classical nonlinear phenomena such as sum-frequency generation or frequency doubling [15], where the initially non-existent field indexed by “l” is created through the P_1^{NL} nonlinear polarization of the material through its second-order nonlinear susceptibility $\chi_{\text{lnm}}^{(2)}$, when the present, finite-amplitude E_n, E_m fields interact according to:

$$P_1^{\text{NL}} = \sum_n \sum_m \chi_{\text{lnm}}^{(2)} E_n E_m \quad (1)$$

However, while classical effects involve the mixing of finite-amplitude electric fields through the nonlinear polarization of the material, SPDC uniquely relies on the electromagnetic signal and idler vacuum field interacting with the pump field. The presence of this vacuum field is a purely quantum mechanical phenomenon, requiring a quantum mechanical description.

In SPDC, the initial quantum state is typically $\psi(t=0) = |0_s, 0_i, N_p\rangle$, indicating zero photons in the signal and idler fields and N_p photons in the pump field. The process is governed by the effective Hamiltonian, which is in plane-wave formalism [9]:

$$\hat{H}_{\text{SPDC}}(t, \mathbf{r}) = i\hbar \frac{2 d_{\text{eff}}}{3 \epsilon_0 V} \sqrt{\frac{\omega_p \omega_s \omega_i}{2 \epsilon_0 V}} (\hat{a}_s^\dagger \hat{a}_i^\dagger \hat{a}_p e^{i\Delta\omega t - i\Delta\mathbf{k}\mathbf{r}} + h.c.), \quad (2)$$

where $\hat{a}_s^\dagger, \hat{a}_i^\dagger$ are the photon creation operators of the signal and idler fields, \hat{a}_p is the photon annihilation operator for the pump, while $h.c.$ stands for their Hermitian conjugate. $d_{\text{eff}} = \chi_{\text{eff}}^{(2)}/2$ is the effective second-order nonlinear coefficient, while $\chi_{\text{eff}}^{(2)}$ is the projection of the $\chi_{\text{lnm}}^{(2)}$ tensor to its subspace determined by the interacting waves. $\Delta\omega = \omega_p - \omega_s - \omega_i$ is the angular frequency mismatch and $\Delta\mathbf{k} = \mathbf{k}_p - (\mathbf{k}_s + \mathbf{k}_i)$ is the wave vector mismatch between the pump and the down-converted beams. $\omega_p, \omega_s, \omega_i$ are the angular frequencies of the pump, signal, idler, ϵ_0 is the vacuum dielectric permittivity and V is the interaction volume. This form of the operator efficiently

addresses the fact that in an SPDC process, the signal and idler photons are generated at the expense of the annihilation of a photon from the pump field.

The quantum state evolves according to the time-dependent Schrödinger equation:

$$\psi(t, \mathbf{r}) = \exp\left(\frac{1}{i\hbar} \int_0^t \hat{H}_{\text{SPDC}}(t', \mathbf{r}) dt'\right) |0_s, 0_i, N_p\rangle. \quad (3)$$

The SPDC process, corresponding to the creation of a single photon pair, arises from the first-order term in the Taylor series expansion of Eq. (3).

$$\psi(t, \mathbf{r}) \approx C_0 |0_s, 0_i, N_p\rangle + C_1 \frac{1}{i\hbar} \int_0^t \hat{H}_{\text{SPDC}}(t', \mathbf{r}) dt' |0_s, 0_i, N_p\rangle + \text{higher order} \quad (4)$$

where C_0, C_1, \dots are the coefficients of the Taylor series accounting for the normalization of the wave function. The higher-order terms correspond to the creation of more than one photon pair. Since higher-photon number states are usually unwanted, the experimental circumstances (pump power, integration time) should be carefully selected so that their probabilities are negligible.

After integrating over both the crystal's interaction volume and the t measurement time, and applying creation and annihilation operators, the resulting quantum state is:

$$\psi(t) = C_1 \frac{2 d_{\text{eff}}}{3 \epsilon_0 V} \sqrt{\frac{\omega_p \omega_s \omega_i}{2 \epsilon_0 V}} \int_0^t e^{i\Delta\omega t'} dt' \int e^{-i\Delta\mathbf{k}\mathbf{r}} d\mathbf{r} |1_s, 1_i, N_p - 1\rangle. \quad (5)$$

Since the values of the temporal and spatial integrals rapidly tend to zero as the coefficients in the exponent grow, from (5) it is apparent that both $\Delta\omega = 0$ (energy conservation) and $\Delta\mathbf{k} = 0$ (momentum conservation, or phase matching) are necessary conditions for an efficient SPDC.

Energy conservation is not problematic, since any frequency combination of signal and idler vacuum fields are always present. Momentum conservation is challenging though, especially when the beams propagate in dispersive media (where the refractive index n varies with ω). Therefore, the direction of propagation and polarization of all pump, signal and idler beams, as well as the respective refractive indices require a careful preparation.

4.2 Phase matching

The two primary techniques to achieve the phase matching condition ($\Delta\mathbf{k} = 0$) are Birefringent Phase Matching (BPM)[16] and Quasi-Phase Matching (QPM)[17][18].

4.2.1 Birefringent Phase Matching (BPM)

BPM utilizes the property of birefringence found in many nonlinear crystals. Birefringent materials exhibit different refractive indices for light with different polarizations relative to the optic axes of the crystal. In the most frequently used so-called uniaxial crystals plane waves can propagate in two distinct linearly polarized

states that are orthogonal to each other. The corresponding propagation velocities can be described by the ordinary refractive index (n_o) and extraordinary refractive index (n_e). The extraordinary refractive index varies with the angle the propagation makes to the optic axis, while the ordinary refractive index does not [19].

By appropriately choosing the polarization of the pump, signal, and idler photons, and fine-tuning the refractive indices by changing the propagation direction through the crystal (angle tuning) or its temperature (temperature tuning), the different wave vectors of the interacting beams can be balanced to satisfy $\Delta\mathbf{k} = \mathbf{0}$, as seen in Figure 1. Angle tuning involves physically rotating the crystal to change the angle of the incident pump beam with respect to the crystal optic axis. This modifies the extraordinary refractive index experienced by the e-polarized waves until phase matching is achieved. Temperature tuning refers to the temperature control of the nonlinear crystal. The refractive indices of the crystal are temperature-dependent. By carefully adjusting the temperature, the phase-matching condition can be met for a specific set of wavelengths and polarizations.

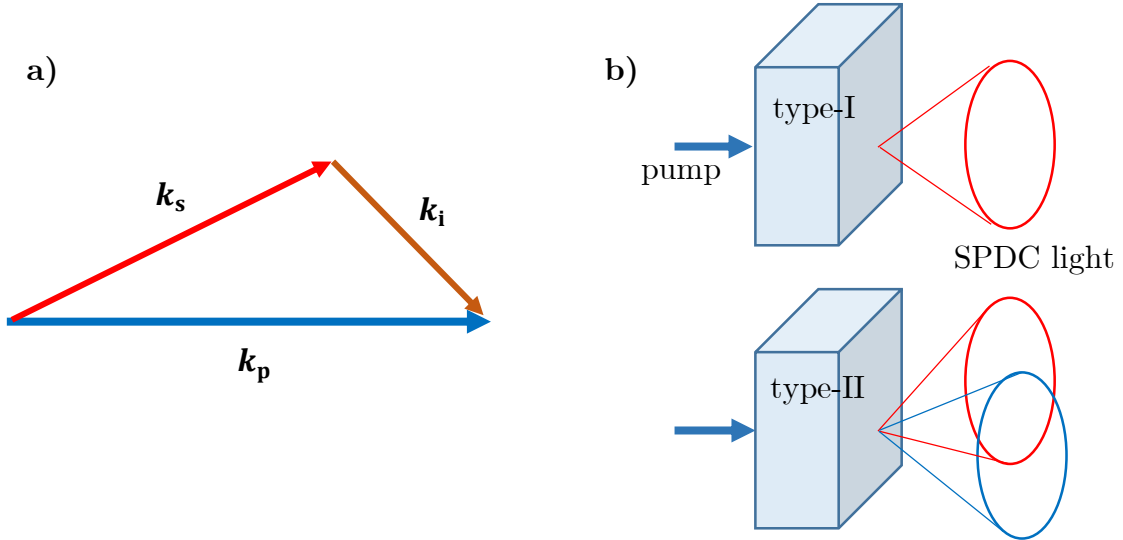


Figure 1. a) General case of BPM, $\mathbf{k}_{p,s,i}$ denote the wave vectors of the pump signal and idler beams respectively. b) conical shape of down-converted light in case of type-I and type-II phase matching.

While Figure 1 a) is a planar k-vector diagram, it represents an axially symmetric situation in the case of type-I phase matching, where down-converted photons form a cone around the pump beam. An example of this is shown in Figure 1. a) General case of BPM, $\mathbf{k}_{p,s,i}$ denote the wave vectors of the pump signal and idler beams respectively. b) conical shape of down-converted light in case of type-I and type-II phase matching. Figure 1 b). In contrast, for type-II phase matching, the signal and idler photons can emerge in two separate cones.

BPM is sorted into the two broad categories of Type-I and Type-II phase matching:

- **Type-I Phase Matching:** In this scheme, the signal and idler photons have the same polarization, which is orthogonal to that of the pump photon. For example, in a negative uniaxial crystal (where $n_e < n_o$), if the pump is extraordinary:

Pump photon (e) \rightarrow Signal photon (o) + Idler photon (o).

The phase-matching condition becomes $\mathbf{k}_p^e(\theta_p) = \mathbf{k}_s^o + \mathbf{k}_i^o$, which translates to $n_p^e(\theta_p)\omega_p = n_s^o\omega_s + n_i^o\omega_i$. The angle θ_p (measured between the pump wave vector and the crystal optic axis) is adjusted to satisfy this condition.

- **Type-II Phase Matching:** Here, the signal and idler photons have orthogonal polarizations. For example, in a negative uniaxial crystal:

Pump photon (e) \rightarrow Signal photon (o) + Idler photon (e).

The phase-matching condition is $\mathbf{k}_p^e(\theta_p) = \mathbf{k}_s^o + \mathbf{k}_i^e(\theta_i)$. This type is particularly useful for generating polarization-entangled photon pairs directly. The distinct polarizations allow for easy separation or manipulation of the signal and idler photons.

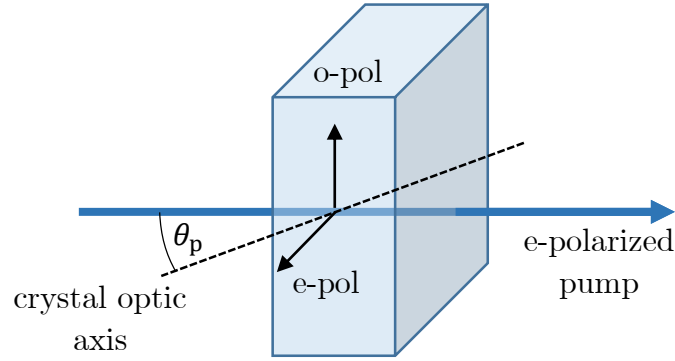


Figure 2. Angle tuning of BPM in a uniaxial birefringent crystal. The refractive index for the extraordinary pump beam depends on the angle between the optic axis and the pump θ_p .

Considering the direction of the pump beam relative to the crystal optic axis phase matching can be further categorized into the following two groups:

- **Critical Phase Matching:** It occurs when phase matching is achieved for propagation directions different from the crystal optic axis (i.e. $\theta_p \neq 0^\circ$ or 90° in uniaxial crystals). In this case the direction of energy flow (Poynting vector) is generally not collinear with the wave vector direction, where phase matching provides a condition for the wavefront normals. For the type-I case the pump and signal/idler beams, for type-II case the signal and idler beams have orthogonal polarization, which results in a difference in their direction of energy flow, known as the Poynting vector walk-off. This can limit the effective interaction length of the beams, reduce efficiency, and affect the spatial quality of the generated beams. Acceptance angles (the range of incident angles for which phase matching is reasonably efficient) are typically small in critical phase matching.
- **Non-Critical Phase Matching (NCPM):** It occurs when phase matching is achieved for propagation along a principal axis of the crystal (e.g. at 90° to the optic axis, often called 90° phase matching). In NCPM, the Poynting vector walk-off effect is minimized or eliminated for the involved extraordinary waves. This leads to larger acceptance angles and potentially higher conversion efficiencies due to longer effective interaction lengths. Temperature tuning is commonly used for NCPM.

Besides the Poynting vector walk-off, temporal walk-off is also present in the type-II configuration. This arises from the difference in refractive indices experienced by the signal and idler beams, leading to a temporal delay between them as they propagate through the crystal. Such a delay can cause issues when the pump has a short coherence length and coherent interference between the two beams is required — for example, in certain entanglement generation schemes (see later sections).

4.2.2 Quasi-Phase Matching (QPM)

Quasi-Phase Matching is a more flexible and often more efficient technique that does not rely on intrinsic material birefringence to the same extent as BPM. Instead, QPM involves periodically modulating the sign of the nonlinear coefficient $\chi^{(2)}$ (therefore also $d_{\text{eff}}^{(2)}$) along the direction of propagation within the crystal. This is typically achieved by fabricating a periodic domain structure in ferroelectric crystals like potassium titanyl phosphate (ppKTP – periodically poled potassium titanyl phosphate) or lithium niobate (ppLN – periodically poled lithium niobate).

In QPM, the phase mismatch $\Delta\mathbf{k}$ that would naturally occur is compensated by an additional vector \mathbf{K}_G provided by the periodic grating. The QPM condition is:

$$\Delta\mathbf{k}_{\text{QPM}} = \mathbf{k}_p - \mathbf{k}_s - \mathbf{k}_i - \mathbf{K}_G = 0 \quad (6)$$

where $K_G = 2\pi/\Lambda_G$ and Λ_G is the grating period. By carefully choosing Λ_G , one can achieve phase matching for virtually any interaction within the transparency window of the material, often utilizing the largest component of the nonlinear susceptibility tensor (e.g., d_{33} in ppKTP or ppLN), which might not be accessible with BPM due to polarization constraints.

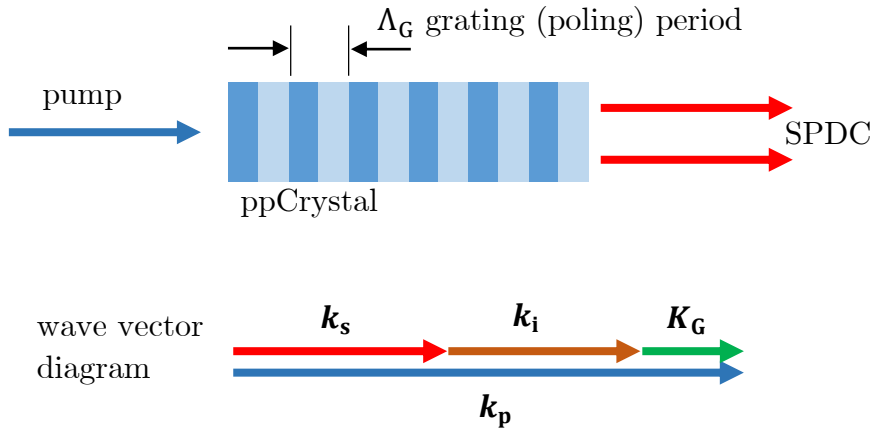


Figure 3. Example of QPM, $\mathbf{k}_{p,s,i,G}$ denote the wave vectors of the pump signal and idler beams and grating vector respectively in a collinear phase-matching condition.

Advantages of QPM:

- **Access to larger nonlinear coefficients:** QPM allows the use of diagonal tensor elements of χ^2 (like d_{33}), which are often much larger than the off-diagonal elements typically used in BPM. This is the so called type-0 phase matching condition, when all pump, signal and idler beams have the same polarization. This can lead to significantly higher conversion efficiencies.
- **Flexibility in wavelength selection:** The grating period Λ_G can be engineered to phase-match specific pump, signal, and idler wavelengths, offering great design freedom.
- **Collinear or non-collinear interactions:** QPM can be designed for both collinear propagation (all beams travel in the same direction) and non-collinear propagation.
- **Engineered spectral properties:** By designing more complex QPM grating structures (e.g., chirped or apodized gratings), the spectral and temporal properties of the down-converted photons can be tailored for specific applications.
- **No Poynting vector walk-off:** Since all interacting waves can have the same polarization (e.g., all extraordinary in ppLN), the walk-off issues inherent in critical BPM can be avoided.

Table 1 presents a comparative overview of the key properties of BPM and QPM.

Feature	Birefringent Phase Matching (BPM)	Quasi-Phase Matching (QPM)
Mechanism	Natural birefringence	Periodic modulation of χ^2
Tunability	Angle or temperature tuning	Grating period design, temperature tuning
Nonlinear Coeff.	Often uses smaller, off-diagonal χ^2 components	Can utilize the largest χ^2 component (e.g., d_{33})
Wavelengths	Limited by material birefringence and transparency	Flexible within transparency range, engineered by Λ_G
Walk-off	Can be significant (critical BPM)	Typically negligible
Fabrication	Simpler crystal preparation	Requires complex periodic poling/structuring
Efficiency	Generally lower	Potentially much higher

Table 1. Comparison between BPM and QPM

4.2.3 Factors influencing phase matching

Several factors intricately influence the phase-matching condition and consequently, the efficiency and properties of the SPDC process.

1. **Dispersion:** The primary challenge in achieving phase matching is the natural dispersion of refractive indices $n(\omega)$, where ω denotes angular frequency. Accurate knowledge of the material dispersion, often modeled by Sellmeier's equation, is crucial for calculating the required crystal orientation, temperature, or QPM grating period.
2. **Crystal Properties:**
 - **Choice of Nonlinear Crystal:** Different crystals (BBO, LBO, KTP, KDP, LN, etc.) offer varying nonlinear coefficients, transparency ranges, damage thresholds, and birefringence. The selection depends heavily on the desired wavelengths and power levels.
 - **Crystal Cut and Orientation:** For BPM, the crystal must be precisely cut and polished at a specific angle relative to its crystallographic axes to allow for angle tuning.
 - **Crystal Length (l):** A longer crystal generally increases the interaction length and thus the number of generated photon pairs. However, it also makes the phase matching condition more stringent (narrower bandwidth for phase matching).
3. **Temperature:** Refractive indices are temperature-dependent. This allows for temperature tuning of the phase matching condition. Maintaining a stable temperature with at least 0.1°C precision is crucial for stable SPDC output.
4. **Pump Beam Characteristics:**
 - **Pump Wavelength (λ_p):** The choice of pump wavelength directly dictates the possible range of signal and idler wavelengths through energy conservation and influences the phase-matching parameters.
 - **Pump Beam Focusing:** As shown in [19], slightly altering the direction of a plane-wave pump beam relative to the crystal surface normal (z) modifies both the apex angle and the axis direction of the SPDC light cone, illustrated in Figure 4 as discrete rings. When the pump beam is convergent, with its focus located inside the crystal, the resulting down-converted light is the integral of all corresponding light cones. In case of critical phase matching (when the optic axis is neither parallel nor perpendicular to the pump) this produces an asymmetrically widened cone, visible in Figure 4 when the ringlets are considered collectively. This can lead to non-collinear emission of signal and idler photons even if collinear phase matching is aimed at with a plane-wave approximation.

- **Pump Beam Bandwidth:** If the pump beam has a finite spectral bandwidth, this will transfer to the down-converted photons and can affect the precision of phase matching for different frequency components within the pump.

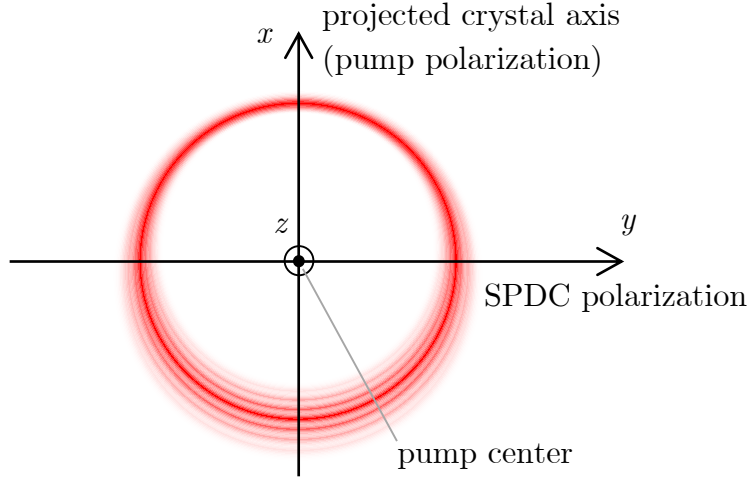


Figure 4. In type-I phase matching asymmetric widening of SPDC cone due to focused pump beam.

5. Angular Considerations:

- **Acceptance Angle:** The range of angles (for the pump beam or for the emission of signal/idler photons) over which phase matching remains efficient. NCPM and QPM generally offer larger acceptance angles than critical BPM.
- **Collinear vs. Non-collinear Phase Matching:** In collinear phase matching, \mathbf{k}_p , \mathbf{k}_s , and \mathbf{k}_i point all in the same direction. In non-collinear phase matching, they form a triangle, leading to signal and idler photons emitted at distinct angles relative to the pump. Non-collinear geometries are often used to spatially separate signal and idler photons or to generate momentum-entangled pairs.

The efficiency of the SPDC process is proportional to the square of the interaction length l and the nonlinear coefficient, but it is also critically modulated by the phase-mismatch factor. For a plane-wave interaction in a crystal of length l , the intensity of the generated light I_{SPDC} is proportional to [16]:

$$I_{\text{SPDC}} \propto l^2 \text{sinc}^2\left(\frac{\Delta k_z l}{2}\right) \quad (7)$$

where $\text{sinc}(x) \equiv \sin(x)/x$ and Δk_z is the component of the phase mismatch vector $\Delta \mathbf{k}$ along the principal direction of propagation (usually the z-axis).

The sinc^2 function has a central peak at $\Delta k_z = 0$ (perfect phase matching) and drops off rapidly as Δk_z increases. The width of this central peak is inversely proportional to l , meaning that longer crystals require more precise phase matching.

4.3 Photon state description, entanglement

In quantum optics, the Dirac (bra-ket) notation [19] is a standard formalism due to its compact and expressive nature. The wave function can be expressed by its relevant parameters (a, b, \dots) as ket: $|a, b, \dots\rangle$ and its complex conjugate as bra: $\langle a, b, \dots|$. A coherent wave function (i.e. a specific photon state) is usually formulated as a linear superposition of a set of basis states. In its finite dimensional, vectorial representation, the ket is considered as a column vector containing the complex coefficients of the bases (and the bra as a row vector). Scalar (inner) product of any two wave functions is written as $\langle a, b, \dots | c, d \dots \rangle$, while the application of the operator \hat{O} of a system on the wave function is expressed as $\hat{O}|a, b, \dots\rangle$. A convenient way to define linear operators on a Hilbert space is given by the outer product e.g. $\hat{O} = |c, d \dots\rangle\langle a, b, \dots|$. A typical example of this is the projection to a subspace. An orthogonal projection onto the subspace spanned by $|a, b, \dots\rangle$ is $|a, b, \dots\rangle\langle a, b, \dots|$. This framework allows focusing on specific properties of quantum systems while abstracting less relevant attributes. For example, when studying the polarization states of photons, the basic states $|H\rangle$ and $|V\rangle$ represent horizontally and vertically polarized photon states, respectively. This formalism emphasizes polarization while disregarding details such as the spatial or temporal distribution of the wavepacket of the photon.

From these fundamental states, other notable polarization states can be constructed:

$$\begin{aligned}
 |D\rangle &= \frac{|H\rangle + |V\rangle}{\sqrt{2}} && \text{(Diagonal)} \\
 |A\rangle &= \frac{|H\rangle - |V\rangle}{\sqrt{2}} && \text{(Anti - diagonal),} \\
 |R\rangle &= \frac{|H\rangle + i|V\rangle}{\sqrt{2}} && \text{(Right - circular),} \\
 |L\rangle &= \frac{|H\rangle - i|V\rangle}{\sqrt{2}} && \text{(Left - circular).}
 \end{aligned} \tag{8}$$

An arbitrary polarization state can be expressed as a coherent superposition:

$$|\psi\rangle = a|H\rangle + b|V\rangle, \tag{9}$$

where $a, b \in \mathbb{C}$ and $|a|^2 + |b|^2 = 1$ implying that after a measurement along the $|H\rangle$ and $|V\rangle$ bases the photon must be in one of these two states with 1 probability in total.

While this representation suffices for pure states, describing systems that are probabilistic mixtures of pure states (mixed states) requires the density matrix formalism [22]:

$$\rho = \sum_i p_i |\psi_i\rangle\langle\psi_i|, \tag{10}$$

where p_i is the probability associated with the i -th pure state $|\psi_i\rangle$, and $\sum_i p_i = 1$.

This formalism enables a complete description of quantum systems and their transformations. Operations or measurements are represented as operators acting on the density matrix. For example:

- **Unitary operations** \hat{U} , where $\hat{U}\hat{U}^\dagger = \hat{U}^\dagger\hat{U} = \hat{I}$ i.e. the unit matrix, therefore they can be inverted and preserves the norm of the state. E.g. polarization changes induced by birefringent waveplates preserve wave energy, as they are reversible transformations.
- **Projective measurements** \hat{P} , where $\hat{P} = |\psi\rangle\langle\psi|$ constrain the state to the eigenstate of the measurement operator $|\psi\rangle$, thereby not preserving the norm. These operations cannot be inverted, see photons passing through a polarizing filter.

In quantum mechanics, multipartite systems, such as photon pairs, are described by extending the Hilbert space to include the subspaces of all constituent particles. The state of such systems can generally fall into one of two categories:

- **Product States:** When the multipartite system can be represented as a Kronecker (tensor) product of the individual subsystems, such as $|\psi\rangle = |\psi_1\rangle \otimes |\psi_2\rangle$ or $\rho = \rho_1 \otimes \rho_2$. In this case, the subsystems are independent and uncorrelated.
- **Entangled States:** When strong correlations exist between the subsystems, making it impossible to describe them independently. These correlations define entanglement, a fundamental feature of quantum systems with no classical counterpart.

A well-known example of entangled states in two-photon systems are the Bell states, given as [23]:

$$|\Phi^\pm\rangle = \frac{|HH\rangle \pm |VV\rangle}{\sqrt{2}}, \quad (11)$$

$$|\Psi^\pm\rangle = \frac{|HV\rangle \pm |VH\rangle}{\sqrt{2}}, \quad (12)$$

where $|HH\rangle \equiv |H\rangle \otimes |H\rangle$.

The process to reconstruct the density matrix of an arbitrary state is called photonic state tomography [24], which requires performing a complete set of projective measurements. For a single photon, this could involve measurements in bases like $|H\rangle, |V\rangle, |D\rangle, |R\rangle$. For multi-photon systems, this extends to correlations between photons. Photonic state tomography is crucial for characterizing entangled states generated by a photon pair source.

State fidelity serves as a quantitative measure of the similarity between two quantum states. It is defined as:

$$F(\rho, \sigma) = \left(\text{Tr} \sqrt{\sqrt{\rho}\sigma\sqrt{\rho}} \right)^2, \quad (13)$$

where ρ and σ are the density matrices of the states being compared and $\text{Tr}(A)$ is the trace of A . Fidelity can be interpreted as the average probability of obtaining the same outcomes for arbitrary measurements performed on the two systems. It is frequently used to evaluate how closely an experimentally prepared quantum state matches a target state.

4.4 Implementation of polarization-state tomography

Full polarization state tomography requires at least a minimal set of polarization basis states capable of mapping the entire state space. I performed my measurements in the most common mutually unbiased polarization bases: $|H\rangle, |V\rangle, |D\rangle$ and $|R\rangle$ [24]. These polarization measurements were realized using Glan-Thompson polarizers (Newport 10GT04) with a high extinction ratio of 100,000:1. The polarizers were mounted in rotatable holders, allowing for easy switching between $|H\rangle, |V\rangle$ and $|D\rangle$. The circular basis $|R\rangle$ was measured using a zero-order quarter-wave plate (QWP) with a vertical fast axis, followed by a linear polarizer aligned to the $|D\rangle$ state. (The fast axis of a wave plate corresponds to the linear polarization state that propagates with a lower refractive index in the wave plate.)

State tomography of a two-particle system, such as an entangled photon pair, requires correlation measurements in all possible combinations of the aforementioned bases. Therefore, I measured coincidence counts in each of them using single-photon detectors (SPADs) and time-correlation electronics (Time Tagger), as detailed in Subsections 4.6.1 and 4.6.2. I corrected my measurements for accidental coincidence counts according to Subsection 5.5.

The output of my photon-pair sources was delivered through single-mode fibers. I collimated the beams emerging from the fibers to allow the use of free-space optics as described above, and then focused the beams onto the surfaces of the single-photon detectors. During the measurements, I blocked ambient light by enclosing the tomography setup in a custom box placed in a darkened lab, thereby reducing the background noise on the detectors. A schematic of the tomography setup is shown in Figure 5. Using the acquired data, I reconstructed the density matrix with the online tomography interface provided by the Kwiat group [25].

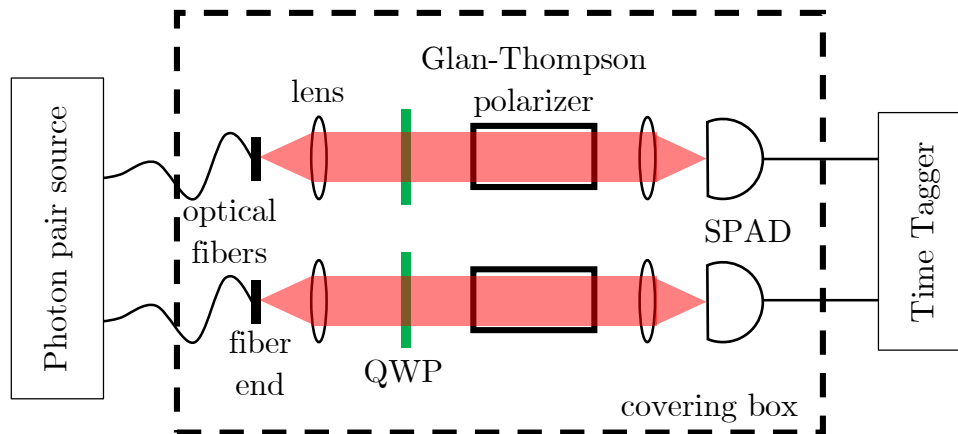


Figure 5. Schematics of the two photon polarization tomography measurement.

4.5 Characteristics of single-mode fibers

Long-distance, high-bandwidth telecommunication systems are built by using single-mode optical fibers made of high-purity fused silica. Being easily available, cost-effective and providing a low-loss, noise-insensitive medium for light transmission, these became widely used components in optical systems. Light is confined in the central core region of optical fibers by total internal reflection. When the core diameter reduces to the order of magnitude of the wavelength, waveguiding properties become pronounced. This results in the formation of waveguide modes, that are only allowed to propagate in the fiber. These have different amplitude distributions in cross section of and velocity along the fiber. The latter is known as mode dispersion. In order to reduce temporal widening of short light pulses sent through a fiber, the core diameter is usually set so small that for a given wavelength range only one fundamental (LP_{01}) mode can propagate through the fiber – these are called single-mode fibers. A key goal of my work was to couple SPDC photons into single-mode optical fibers (SMFs). To accomplish this, it is essential to analyze the field propagating within the fiber and design an optimal coupling system for the free-space down-converted field.

The transverse amplitude distribution of the fundamental mode in an SMF is a Bessel function of the first kind and zero order (which is Gaussian-like) in the core, while in the cladding it follows the modified Bessel function of the second kind and zero order (with exponential-like shape). The normalized frequency parameter for the set of available propagating modes in the SMF is defined as [26]:

$$V = \frac{2\pi}{\lambda} a \sqrt{n_1^2 - n_2^2}, \quad (14)$$

where a is the core radius, λ is the wavelength of light, and n_1 and n_2 are the refractive indices of the core and its surrounding medium called cladding, respectively. The single-mode regime of an optical fiber is achieved when the fiber core diameter and the wavelength of light satisfy the condition $V < 2.405$. This means that only the fundamental mode or no modes at all is allowed to propagate, higher-order modes are not guided.

When coupled to free space, the fundamental mode diffracts as a Gaussian beam [27] with an electric field distribution given by:

$$\mathbf{E}(x, y, z) = \mathbf{E}_0 \frac{w_0}{w(z)} \cdot \exp\left(-\frac{x^2 + y^2}{w(z)^2}\right) \cdot \exp\left(-i\left(kz + k\frac{(x^2 + y^2)}{2R(z)} - g(z)\right)\right), \quad (15)$$

where \mathbf{E}_0 incorporates the magnitude of the field, and also the direction of polarization, w_0 is the beam waist radius, $w(z)$ is the beam radius at a given z position from the beam waist, $R(z)$ is the radius of curvature, k is the wavenumber and $g(z)$ is the Gouy phase. The waist of the free space Gaussian beam is aligned with the SMF input face (at $z = 0$), with w_0 equalling to the propagating mode field radius in the fiber. The same is true for incoupling, therefore, efficient coupling can only be realized if w_0 is known, and the incident beam on the fiber closely approximates the Gaussian beam of

(15). If the geometrical and optical parameters of the SMF are known, then the mode field radius for a given wavelength can be estimated using Marcuse's equation [28]:

$$w_0 = a \left(0.65 + \frac{1.619}{V^{3/2}} + \frac{2.879}{V^6} \right) \quad (16)$$

The SMF coupling efficiency (η_{fib}) can be numerically calculated if the wavefront of the incident radiation is known. This involves evaluating the normalized overlap integral between the fiber mode and the wavefront amplitude (orthogonal projection):

$$\eta_{\text{fib}} = \frac{|\langle W|F \rangle|^2}{\langle W|W \rangle \langle F|F \rangle} \quad (17)$$

where $|F\rangle$ describes the complex amplitude of the fiber mode, and $|W\rangle$ represents the complex amplitude of the wave propagating from the exit pupil of the optical system at the input end of the fiber. The nominator represents a normalization by the intensities of both fields.

In my work I used ZEMAX OpticStudio [29], a powerful optical design tool, to determine both $|F\rangle$ and η_{fib} for a given system. This makes it an invaluable resource for designing effective coupling optics between the SPDC beam and the SMF.

There is a special type of SMF known as the polarization-maintaining SMF. Such slightly anisotropic fibers have two well-defined axes, both perpendicular to the direction of propagation and to each other. The unique property of this fiber is that if the coupled light is linearly polarized along one of these axes, it maintains its linear polarization during propagation. This is not generally the case for standard SMFs, where the polarization of the propagating light is strongly affected by mechanical deformations of the fiber (see Subsection 4.6.3.).

4.6 Components of the measurement apparatus

The experimental setup utilized for the development and characterization of correlated photon pair sources relies on precision instrumentation designed to detect and time-stamp single-photon events with high accuracy. This section outlines the key components of the measurement apparatus, detailing their roles in ensuring reliable data collection and analysis.

4.6.1 Single-photon detection

Central to the detection scheme are single-photon avalanche photodiode (SPAD) detectors. Two types of SPAD detectors were employed: the ID Quantique ID100 and the Excelitas SPCM-AQRH-44. These detectors are operating in the visible to near-infrared spectrum. Both detectors are avalanche photodiodes operated in Geiger mode, enabling the detection of individual photon events. The IDQ detector has superior timing resolution, while the Excelitas detector offers higher detection efficiency. These characteristics make them complementary for different experimental conditions. See the specifications in the Table 2.

A notable feature of the ID100 is its exceptional timing resolution, ensuring that photon arrival times can be registered with high precision. The low noise characteristics and

fast response time contribute to minimizing spurious counts, enhancing the signal-to-noise ratio in coincidence measurements. The Excelitas SPCM-AQRH-44 is widely recognized for its high detection efficiency and reliability. Its superior efficiency makes it particularly suitable for photon correlation experiments with low photon pair flux.

Both detectors operate in free space by default. To enable the measurement of fiber-coupled photon beams, I used an adapter to interface the fibers with the detectors. Each adapter comprises two identical aspheric lenses (Roithner Lasertechnik CAY046). The first lens collimates the beam emerging from the fiber, while the second focuses it onto the detector surface. Beam alignment is achieved by adjusting the position of the second lens in a plane perpendicular to the optical axis using an actuator (Thorlabs SCP05). The schematics of the design for this adapter is depicted in Figure 6. The detector efficiencies listed in Table 2 were measured using these adapters. These adapters are particularly practical, as they allow for the placement of arbitrary polarizers and phase plates in the collimated beam, facilitating convenient polarization measurements of the photons.

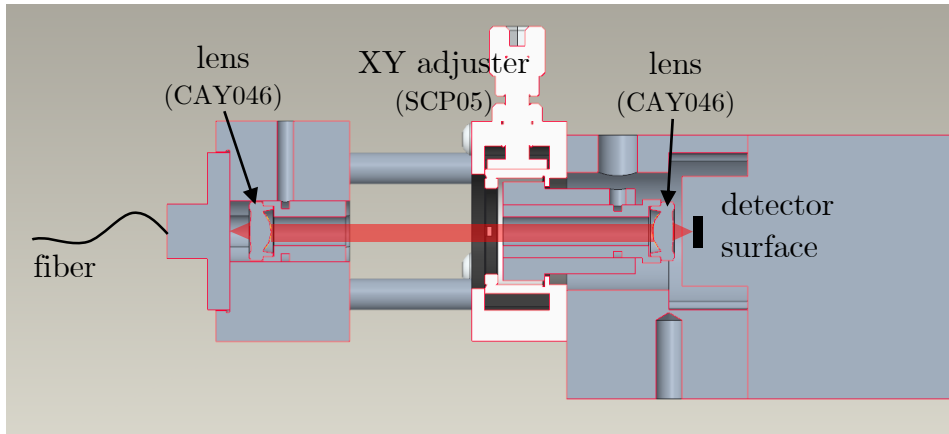


Figure 6. Schematic design of the fiber interface to Excelitas SPCM-AQRH-44 detectors.

4.6.2 Time tagging and coincidence counting

Temporal correlation measurements between photon pairs are facilitated by the quTools quTAU, and the Schwabian Instruments Time Tagger Ultra, versatile and high-performance time-to-digital converters. These devices record the arrival times of detection events with picosecond precision, making them an indispensable tool for coincidence counting and time-resolved measurements. Our quTAU has 8, while our Time Tagger Ultra features 4 input channels, allowing simultaneous monitoring of multiple detectors. This flexibility supports complex experimental configurations, including those involving multi-photon detection schemes.

Time taggers operate by registering digital pulses generated by the SPAD detectors each time a photon is detected. By correlating detection events across multiple channels, these devices are able to capture up to four-fold coincidence events, create histograms of arrival times between channels, determine intensity correlation functions, etc.

Setting up the Time Tagger Ultra for a given measurement is more flexible compared to the quTAU device, since all processing of the raw temporal data is performed on the computer. As a result, an arbitrary number and combination of coincidence or correlation channels can be defined between the physical input channels. In contrast, our quTAU device has fixed internal logic, limiting the number of possible channel combinations. Table 2 summarizes the key properties of these photon-counting devices.

Device	Measured Detection Efficiency at 810 nm	Dark Count Rate [cps]	Timing Jitter [ps]
ID Quantique ID100	$4.8 \pm 0.5\%$	100	50
Excelitas SPCM-AQRH-44	$42 \pm 4.8\%$	100	350
quTools quTAU	N/A	N/A	~ 81
Schwabian Instruments Time Tagger Ultra	N/A	N/A	9

Table 2. Key specifications of the detectors and time taggers used in the experimental setup

4.6.3 Polarization optics

To conduct polarization state tomography, precise control and analysis of photon polarization are essential. The experimental setup incorporates Glan-Thompson prisms (usually indicated as P in measurement setup depictions) as high-extinction polarizers, ensuring accurate polarization filtering and state preparation. These prisms operate across a wide spectral range, making them optimal for quantum optics experiments at various wavelengths. Polarization state measurements are performed by rotating the Glan-Thompson prisms and combining them with phase retarding plates, allowing for the projection of photon states onto different polarization bases. This approach facilitates the reconstruction of the full polarization state of the photon pairs.

Polarization control is also important when the field propagates in a non-polarization maintaining SMF. This can be easily achieved by forming several appropriately sized loops on the fiber and rotating them with respect to each other. The loops serve a similar purpose as a phase plate. Mechanical stress due to bending induces birefringence, viz. a refractive index difference between the radial and axial directions of the loop [49]. The resultant phase shift Φ can be tailored by choosing the geometrical parameters of the loop according to Eq. (18):

$$\Phi = \frac{2\pi^2 a N d^2}{\lambda D} \quad (18)$$

where $a = 0.133$ is a constant applicable for silica-based optical fibers, N is the number of loops in a coil, d is the diameter of the cladding, λ is the design wavelength, and D is the diameter of the loop. By adjusting these parameters, the same functionality as a half- or quarter-wave plate can be achieved.

A device capable of forming and rotating three coils of the fiber ($\lambda/4$ loop, $\lambda/2$ loop, $\lambda/4$ loop) can produce an arbitrary polarization transformation. During my work, I designed and 3D-printed several of these fiber polarization compensators (FPCs), one of which is depicted in Figure 7.

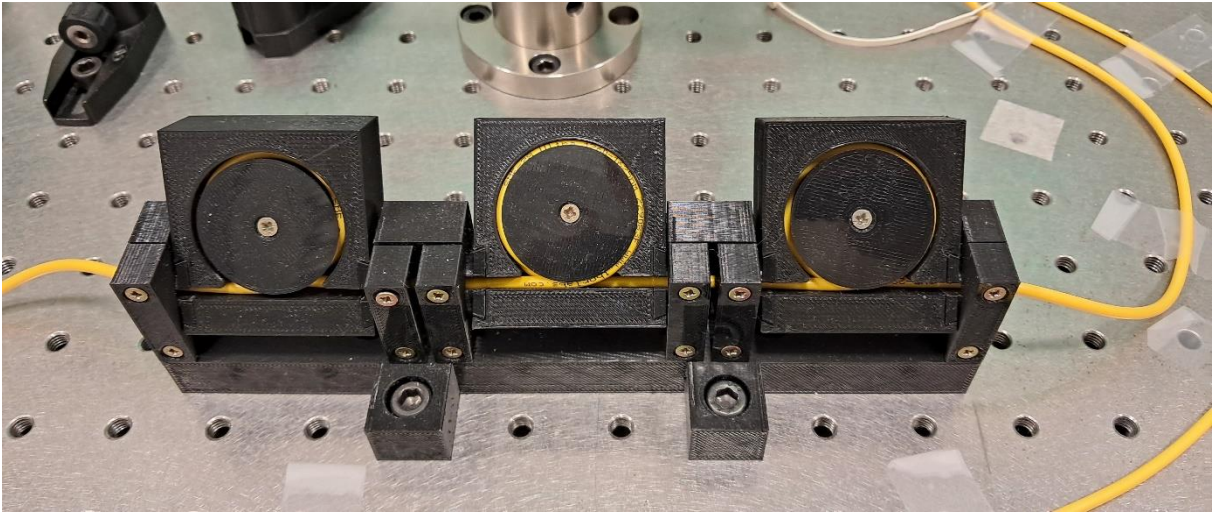


Figure 7. 3D printed fiber polarization compensator (FPC) consisting of three loops of fiber, forming a $\lambda/4$ loop, $\lambda/2$ loop, $\lambda/4$ loop, therefore capable of an arbitrary polarization transformation.

5 Compact single-mode fiber-coupled photon pair source

Type-I phase matching provides a relatively cheap, robust and simple means to produce correlated photon pairs. However, the conical shape of the resulting field gives rise to some problems. As mentioned in the Introduction, many applications require photons to be coupled into single-mode fibers. Theoretical calculations have already shown that it is possible to couple the cone-shaped light of type-I phase matching into single-mode fibers [50][51]. However, these considerations were based on the analytic evaluation of paraxial models, neither accounting for the aberrations of real lenses, nor the truncation and diffraction effects of their apertures. In our group, I was working on the construction of high-flux, small, portable, robust, single-mode fiber-coupled correlated photon-pair sources, the assembly and adjustment process of which are designed to be straightforward. In this section, I present the technology of a photon-pair source that utilizes type-I phase-matching to perform SPDC in a BBO crystal. Design considerations are given, system setup and alignment process are described in detail, measurement results are compared with theoretical calculations.

5.1 Design of the optical system

The technique for producing down-converted light using type-I BBO has been well known for a long time [52]. However, the resulting light cone is not optimal for fiber coupling: its opening angle is narrow, and the cross-section forms a ring with a thin wall. The angular extent of this ring is determined by the crystal length and the collimation state of the pump beam [53]. According to Dragan [50], focusing the pump beam appropriately into the crystal allows adjustment of the ring thickness to meet fiber-coupling requirements, even for relatively long crystals.

Another challenge is separating the weak down-converted light from the intense pump beam. To address these challenges, I developed a setup containing the minimum number of elements and degrees of freedom to simplify the design and alleviate the adjustment process. Figure 8. shows a schematic of the optical system, while Table 5 lists all elements utilized in the setup.

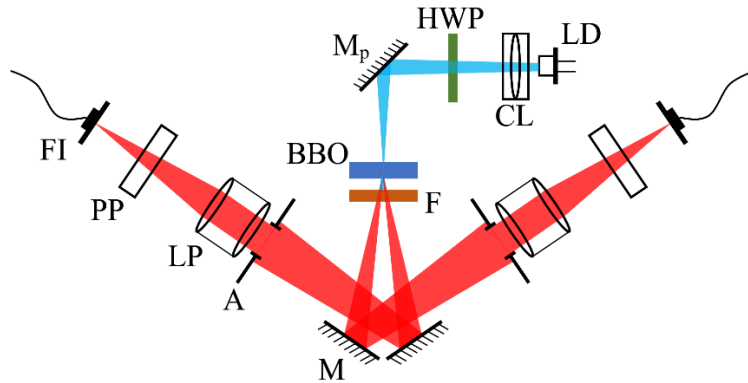


Figure 8. Schematics of the optical setup. Blue and red beams indicate pump and down-converted light, respectively. LD: laser diode, CL: focusing assembly, M_p : pump fold mirror, HWP: half-wave plate, F: long-pass filter, M: dielectric hot mirror, A: aperture (its actual shape is depicted in Figure 15), LP: relaying lens pair, PP: plane-parallel plate, FI: fiber input.

The pump beam is generated by a linearly polarized laser diode with a wavelength of λ_p , a measured polarization ratio of 30:1, and a spectral width of 0.54 ± 0.11 nm FWHM (full width at half maximum). Its light is focused into the crystal through a half-wave plate, enabling precise control of the polarization direction. The BBO crystal generates down-converted light centered at a wavelength of λ_s , corresponding to the degenerate photon state.

Immediately after the crystal, optical filters are placed to attenuate the pump beam as a first step. The SPDC cone is then folded by two mirrors, the purpose of which is fourfold:

- 1) They separate the thin light cone into two parts, creating space for the focusing optics.
- 2) They are long-pass (hot) mirrors that serve as the second step in pump attenuation.
- 3) Their edges almost touch each other, forming a narrow slit that allows the remnants of the pump to escape without significantly decreasing photon flux in the light cone.
- 4) They enable coarse adjustments of the light direction entering the focusing optics through tipping and tilting.

The focusing optics include specially designed apertures with baffles that block any remaining pump beam. The focus spots of light converging towards the single-mode, polarization-maintaining optical fibers must be aligned laterally with sub-micron accuracy to optimize and sustain coupling efficiency. To achieve this, I used plane-parallel plates positioned near the fiber adapters. Adjusting the tilt of these plates provides a precise method for fine-tuning the spot position relative to the fiber core. The main parameters of the system are summarized in Table 3.

Construction parameter	Short notation	Value
Pump wavelength	λ_p	405 nm
SPDC center wavelength	λ_s	810 nm
Phase-matching output angle	φ_0	3°
Light power of pump beam	P_p	44 mW
Down-conversion efficiency	$\eta_{dc} \cdot 10^9$	1.01±0.042
Filter transmittance for SPDC	$T_{\text{filt}}(\lambda_s)$	0.945±0.005
Filter transmittance for pump	$T_{\text{filt}}(\lambda_p)$	$< 10^{-5}$
Optics transmittance for SPDC	$T_{\text{opt}}(\lambda_s)$	0.985
Optics transmittance for pump	$T_{\text{opt}}(\lambda_p)$	0.235
Fiber numerical aperture	NA_{fib}	0.12
Crystal dimensions	$H \times W \times L$	5×5×3 mm
Long-pass filter cut-off	λ_{filt}	600 nm

Table 3. Fixed construction parameters of the optical system. For detailed explanation see the text and Figure 10. $T_{\text{filt}}(\lambda_s)$ was obtained by measurement, all other transmittance values were taken from manufacturer specifications.

5.2 Maximizing fiber-coupling efficiency for SPDC light

Single-mode fibers require the input field to match their mode profile in both intensity and phase distribution to achieve a high coupling efficiency. The intensity distribution in telecommunication fibers approximately follows that of the Gaussian LP_{01} mode. However, for type-I phase matching, only two opposite segments of the SPDC ring can illuminate the aperture of the coupling optics (see Figure 9) in order to separate the photon pairs. This light distribution initially appears unsuitable for single-mode fibers, necessitating an evaluation of its coupling properties.

Focusing the pump beam affects the distribution of the resultant SPDC light, see Subsection 4.2.3. My primary task was to optimize the resultant ring width to maximize coupling efficiency. Achieving this required algorithms incorporating ray-tracing and diffraction calculations, necessitating the development of an appropriate model for the down-converted light.

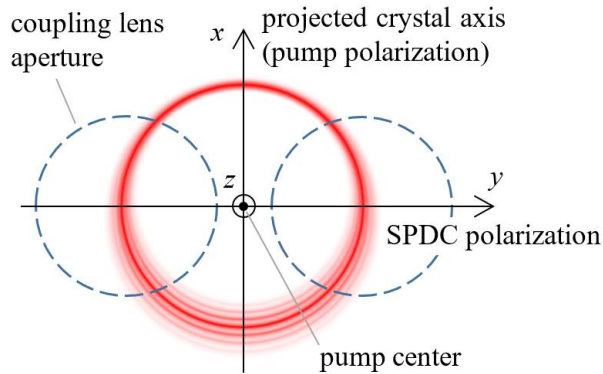


Figure 9. Schematic illustration of down-converted light distribution in wave-vector space for pump beams pointing to different directions (only the central pump direction is indicated). The crystal surface is orthogonal to the z axis.

Since SPDC is a parametric process (i.e. the beams involved are coherently interlocked), pumping a non-linear material, such as BBO, with a laser beam of LP_{01} mode produces such a down-converted light, the radial intensity distribution of which is also Gaussian [19]. To minimize the effects of illumination asymmetry observed in Figure 9, I selected a crystal orientation where the optic axis lies parallel to the $x - z$ plane, and aligned the coupling optics within the $y - z$ plane. To simplify my simulations, I neglected variations in ring thickness within the apertures of the coupling optics. Instead, I modeled the down-converted light as an axially symmetric cone with a half-angle of φ_0 and a constant ring thickness of $\Delta\varphi$ (see Figure 10). The intensity distribution is described by Eq. (19), where the polar angle φ is measured from the axis of the pump beam (z):

$$I(\varphi) = \exp\left(-2\left(\frac{\varphi - \varphi_0}{\Delta\varphi}\right)^2\right). \quad (19)$$

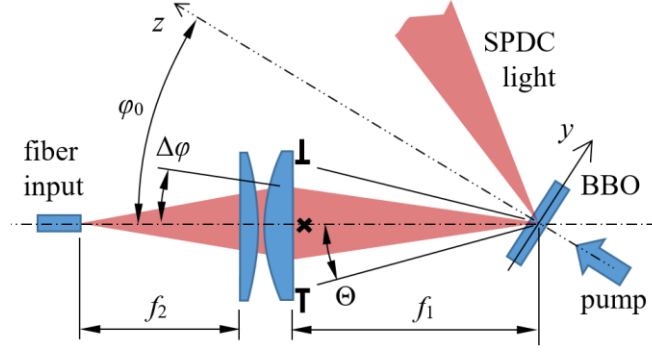


Figure 10. Relative positions of the BBO crystal, coupling LP and FI. φ_0 : output angle of type-I phase matching, $\Delta\varphi$: angular extension of down-converted light (ring thickness), Θ : angular aperture radius, f_1 ; f_2 : effective focal lengths of the LP components. The indicated coordinate system is the same as that of Figure 9. The fold mirror (M) in Figure 8 is omitted from this representation of the beam path.

The parametric nature of SPDC also guarantees that the wave function of the generated light remains phase-aligned with that of the pump source. Thus, if the source is spatially coherent, the down-converted light will exhibit the same coherence. In the Fraunhofer regime, where the source is sufficiently far away, the wavefronts of spatially coherent light can be approximated with high precision as spherical surfaces. This approximation is valid in our setup because the pump focal spot diameter is approximately $30\ \mu\text{m}$, while the object distance of the coupling optics is $f_1 \approx 150\ \text{mm}$ (as discussed later).

The merit function of my optimization procedure is coincidence efficiency (η_c), which represents the probability of transforming a down-converted photon pair into a fiber-coupled photon pair. Denoting the flux of coincidence events at the fiber outputs as Φ_s^c and the photon flux generated in the crystal as Φ_{s0} , η_c is defined as Eq. (20):

$$\eta_i(\lambda_s) \equiv \frac{\Phi_s^c}{\Phi_{s0}} = T_{\text{filt}}(\lambda_s)^{2n} \cdot T_{\text{opt}}(\lambda_s)^2 \cdot \eta_{\text{ap}}(\lambda_s) \cdot \eta_{\text{fib}}(\lambda_s)^2. \quad (20)$$

In the equation above, $T_{\text{filt}}(\lambda_s)$ and $T_{\text{opt}}(\lambda_s)$ represent the transmittance of a single filter and the rest of the optical system, respectively, at the SPDC center wavelength (λ_s). The parameter n denotes the number of filters applied. The term $\eta_{\text{ap}}(\lambda_s)$ represents the ratio of light power collected by the aperture of the coupling optics relative to that of the half-cone, while $\eta_{\text{fib}}(\lambda_s)$ signifies the fiber-coupling efficiency. While $T_{\text{filt}}(\lambda_s)$ and $T_{\text{opt}}(\lambda_s)$ are determined by measurements and manufacturer specifications, the term $\eta_{\text{ap}}(\lambda_s) \cdot \eta_{\text{fib}}(\lambda_s)^2$ in Eq. (20) can be optimized by adjusting three variables: $\Delta\varphi$ (the angular ring thickness), Θ (the angular aperture radius of the coupling lens), and the lateral magnification m .

The magnification is given by $m = f_2/f_1$, where f_1 and f_2 are the effective focal lengths of the first and second components of the coupling lens pair (LP) (see Figure 10). Adjusting m ensures that the focal spot size matches the fiber's mode diameter. Both $\Delta\varphi$ and m influence the diffraction intensity distribution of the focal spot at the fiber input, while Θ determines the fraction of the half-cone captured by the coupling optics. Increasing Θ allows the lens aperture to capture more light from the half-cone, thereby

increasing η_{ap} . However, this also curves the irradiance distribution, degrading the focal spot quality behind the lens and reducing η_{fib} . By finding a balance between these competing effects, I could maximize coincidence efficiency.

The efficiency term was evaluated in ZEMAX OpticStudio [29] using scalar diffraction simulations based on the above-described light source model. Not knowing the actual lens shapes yet, at this phase, an ideal (i.e., paraxial) LP was used as a relay. The coupling efficiency $\eta_{\text{fib}}(\lambda_s)$ was calculated as in Eq. (17), the scalar product of the focal spot irradiance distribution and the LP_{01} mode of the single-mode optical fiber with a numerical aperture of NA_{fib} . Optimization calculations were repeated for various pre-selected m magnifications and $\Delta\varphi$ ring thicknesses, with the aperture radius Θ as a free optimization variable. This process resulted in a map of the efficiency term, including the location of its maximum, as shown in Figure 11. For completeness, the tilt and decentration of the LP were also varied, but the optimum position proved to be when the coupling lenses were centered and set perpendicular to the direction of φ_0 .

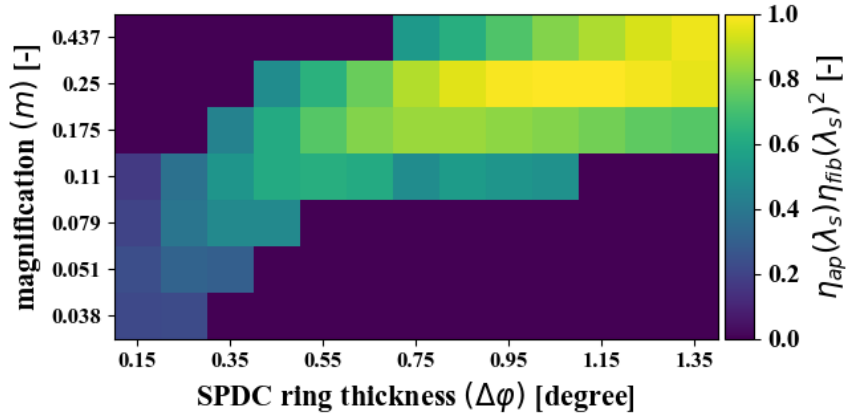


Figure 11. The $\eta_{\text{ap}}(\lambda_s) \cdot \eta_{\text{fib}}(\lambda_s)^2$ term of coincidence efficiency in Eq. (2), numerically evaluated for an ideal coupling LP. Values are normalized to unity at maximum. Indigo fields with zero efficiency indicate areas where no calculations were made. The vertical axis is exponential, each row is labeled with the corresponding magnification value.

The ideal magnification is $m = 0.25$ with an aperture radius of $\Theta = 1.92^\circ$. The physical LP must have a magnification close to this m , and an aperture that is not less than Θ . Additionally, it should produce a diffraction-limited image quality. For the sake of simplicity, I aimed to build the photon source mostly using off-the-shelf elements. Therefore, I sought an achromatic mounted LP as a relay. The only LP available in stock close to these requirements had focal lengths of $f_1 = 150$ mm and $f_2 = 75$ mm. Since its magnification is $m = 0.5$ according to its design intent, I re-optimized the system using the detailed optical model of the chosen LP in ZEMAX. The final system parameters, together with the calculated efficiency values, are listed in Table 4, while stock data of the specific lenses can be found in the component list (see Table 5). The irradiance distribution calculated at the fiber inputs for the optimum system parameters is shown in Figure 12. Calculations by Dragan [50] for the optimal SPDC beam waist show good agreement with these results.

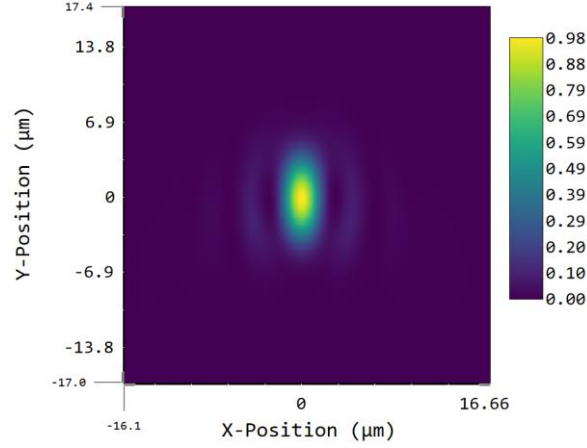


Figure 12. Irradiance distribution of the monochromatic diffraction Point Spread Function calculated at the fiber inputs for λ_s . The maximum value corresponds to the Strehl ratio, that is defined as the ratio of the peak intensity of the actual point spread function to that of an ideal, diffraction-limited system.

Optimized parameters	Short notation	Value
SPDC ring thickness	$\Delta\varphi$	1.05°
Pump num. aperture	NA_p	0.0085
Magnification	m	0.408
Aperture radius	θ	3.34°
Pump baffle radius	a	1.9°
Number of filters	n	2
Efficiencies calculated at optimum		
SPDC light inside aperture	$\eta_{\text{ap}}(\lambda_s)$	0.729
Fiber-coupling eff. for SPDC	$\eta_{\text{fib}}(\lambda_s)$	0.509
Coincidence efficiency	$\eta_c(\lambda_s)$	0.148
Pump light inside aperture	$\eta_{\text{ap}}(\lambda_p)$	$3.29 \cdot 10^{-14}$
Fiber-coupling eff. for pump	$\eta_{\text{fib}}(\lambda_p)$	$3.56 \cdot 10^{-6}$
Real to pump coincidences	SNR	$> 10^{15}$

Table 4. Optimal fiber-coupling optics parameters and the corresponding calculated efficiency terms.

In order to achieve the optimum value of $\Delta\varphi$, the pump beam has to be slightly convergent, which broadens the angular spectrum of down-converted light. I determined the connection between the $1/e^2$ intensity half-angle of the pump beam and the ring thickness experimentally. For this purpose, I designed and built a custom goniometer with which the angular distribution of the down-converted light could be studied. The schematics of this setup are depicted in Figure 13. I varied the numerical aperture of the pump (NA_p) and measured the corresponding ring thickness ($\Delta\varphi$). This measurement involved scanning the SPDC light with a small aperture (A) in the goniometer and fitting Eq. (19) to the acquired photon counts, as they are proportional to intensity. The obtained dependence of ring thickness versus pump focusing is plotted in Figure 14. By linear interpolation, I extracted a pump angle of 0.485° from the diagram, which corresponds to a numerical aperture of $\text{NA}_p = 0.0085$ (see the optimization results above).

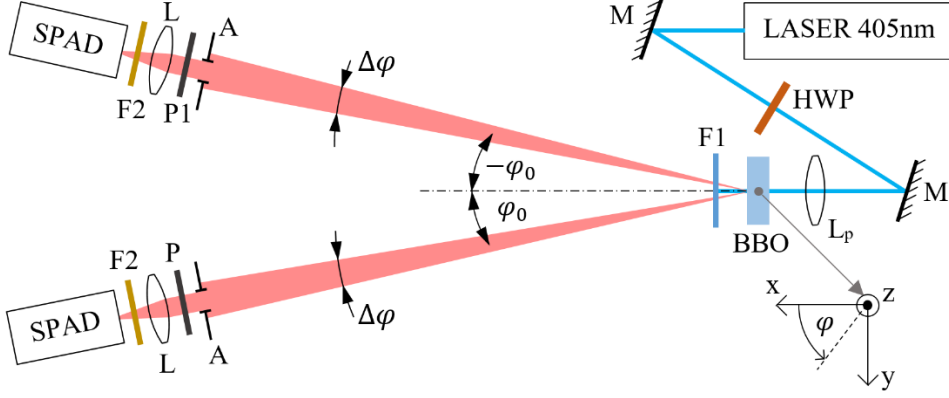


Figure 13. Schematics of the experimental setup for examining the angular distribution of SPDC light generated from a type-I BBO crystal. HWP: half-wave plate, M: mirror, L_p : pump focusing lenses, F1: $810 \pm 5 \text{ nm}$ bandpass filter, A: aperture P: linear polarizer, L: focusing lens, F2: 647 nm long-pass filter

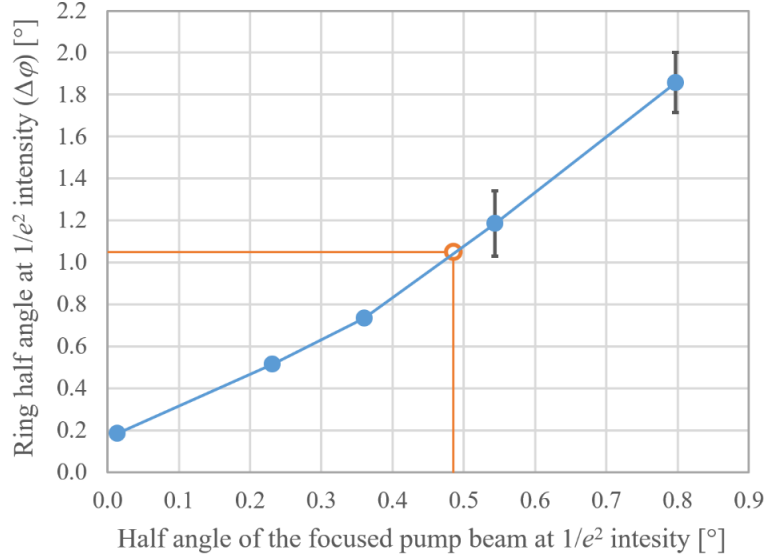


Figure 14. The measured relationship between pump convergence angle and ring thickness of down-converted light. Data points were determined by fitting Eq. (19) to radial profiles of the SPDC ring. The measuring error is represented by the 95% confidence interval of fitting parameters. Error bars of the first three data points are smaller than the marker size.

5.3 Elimination of pump photon-related coincidences

Unfortunately, alongside the useful SPDC light, a small amount of the pump beam also couples into the single-mode fibers. As a result, pump photons may cause unwanted coincidences with either a down-converted photon or another photon directly from the pump. Below, I calculate the flux of these so-called random events and provide an estimation for the highest achievable ratio of pure SPDC- to pump-photon-caused coincidences in the system. To keep the results detector-independent, I determine the flux values at the fiber outputs as if they were measured with perfect detectors of 100% efficiency. In this sense, the fluxes of the pump and signal photons are denoted by Φ_p and Φ_s , respectively. Their values can be calculated by Eq. (21) and Eq. (22), while the coincidence flux Φ_s^c coming from down-converted light can be expressed by Eq. (23):

$$\Phi_p = \frac{P_p}{h\nu_p} \cdot T_{\text{filt}}(\lambda_p)^n \cdot T_{\text{opt}}(\lambda_p) \cdot \eta_{\text{ap}}(\lambda_p) \cdot \eta_{\text{fib}}(\lambda_p), \quad (21)$$

$$\Phi_s = \frac{P_p}{h\nu_p} \cdot \eta_{\text{dc}} \cdot T_{\text{filt}}(\lambda_s)^n \cdot T_{\text{opt}}(\lambda_s) \cdot \eta_{\text{ap}}(\lambda_s) \cdot \eta_{\text{fib}}(\lambda_s), \quad (22)$$

$$\Phi_s^c = \Phi_s \cdot T_{\text{filt}}(\lambda_s)^n \cdot T_{\text{opt}}(\lambda_s) \cdot \eta_{\text{fib}}(\lambda_s). \quad (23)$$

In these formulae, P_p represents the power and ν_p the frequency of the pump beam, while η_{dc} stands for down-conversion efficiency. Since the laser I use for pumping is a coherent, continuous-wave source, and the integration time corresponding to my measurements ($\tau = 3.24$ ns) is much greater than the 11 fs coherence time of SPDC light (estimated from the spectrum depicted in Figure 20), the photon statistics at fiber outputs can be regarded as Poissonian [55][56]. The expected value of the distribution, so the mean number of counts is $\Phi_p \tau$ in a τ temporal window for the pump photons and accordingly $(\Phi_s + \Phi_p)\tau$ for the pump and SPDC combined. From this distribution, I derive:

$$\Phi_p^r = \frac{1}{\tau} [1 - \exp(-(\Phi_s + \Phi_p)\tau)] \cdot [1 - \exp(-\Phi_p\tau)] \cdot \exp(-\Phi_s\tau), \quad (24)$$

which shows the random coincidence flux Φ_p^r in the case when τ contains one or more photons of any kind at one fiber output and at least one pump photon at the other (with down-converted photons excluded). See detailed explanation in Subsection 10.1 of the Appendix. Equation (25) defines the corresponding signal-to-noise ratio.

$$SNR \equiv \frac{\Phi_s^c}{\Phi_p^r} \quad (25)$$

The optical system presented in the previous subsection has two remaining parameters to optimize for maximum SNR : the number of filters n and the angular baffle radius α , for an illustration of which see Figure 15. The baffle is centered on the pump axis, and the value of α was set to 1.9° . This corresponds to the inner $1/e^2$ intensity radius of down-converted light, as described in Eq. (19), reducing $\eta_{\text{ap}}(\lambda_s)$ by only 1%. Regarding the filters, the more of them I introduce, the higher the SNR will be; however, their presence also decreases η_c , as shown in Eq. (20). To achieve a resultant $SNR > 10^{15}$, I chose $n = 2$. The optimal parameter values are collected in Table 4, along with the numerical results for all efficiency terms. Having all these numbers, the heralding efficiency (aka. heralding ratio) \mathbb{P}_h can also be calculated, as given by Eq. (26). All simulated values are summarized in Table 6.

$$\mathbb{P}_h \equiv \frac{\Phi_s^c}{\Phi_s} = T_{\text{filt}}(\lambda_s)^n \cdot T_{\text{opt}}(\lambda_s) \cdot \eta_{\text{fib}}(\lambda_s). \quad (26)$$

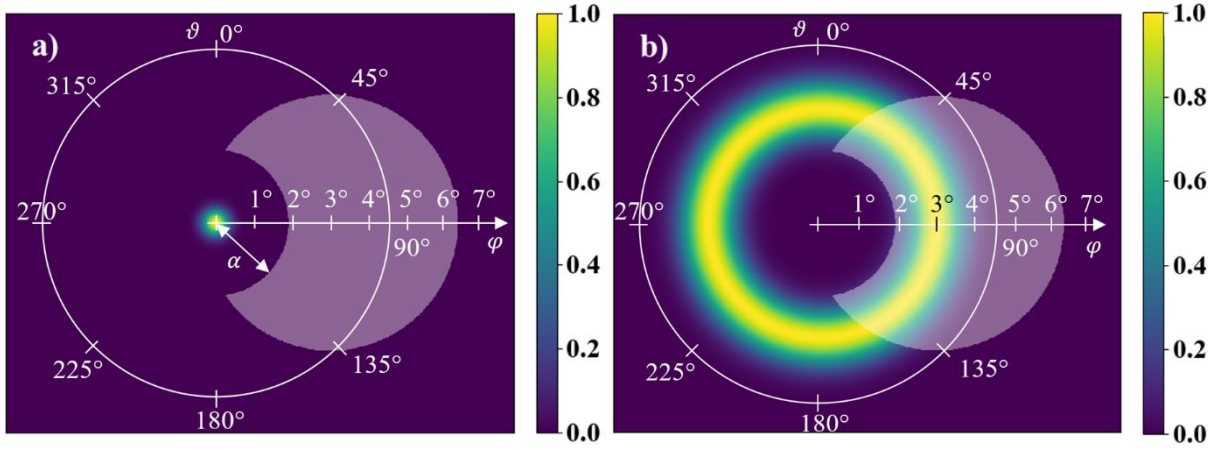


Figure 15. The crescent-shaped aperture of the fiber-coupling system, where light purple color denotes the transparent region. a) and b) show the pump and SPDC light beams, respectively. All dimensions are proportionally scaled. The pump beam axis is used as a polar reference, the azimuth angle ϑ is measured relative to the x-axis of Figure 10.

5.4 Physical implementation and opto-mechanical alignment

The first version of the realized photon-pair source is shown in Figure 16, while the components used to build it are listed in Table 5. The pump laser was a continuous-wave (CW) diode laser (LD) in a focusable mount containing a collimating lens (CL). Optimal NA_p was implemented by appropriately focusing the collimation optics of the laser diode at a finite image distance.

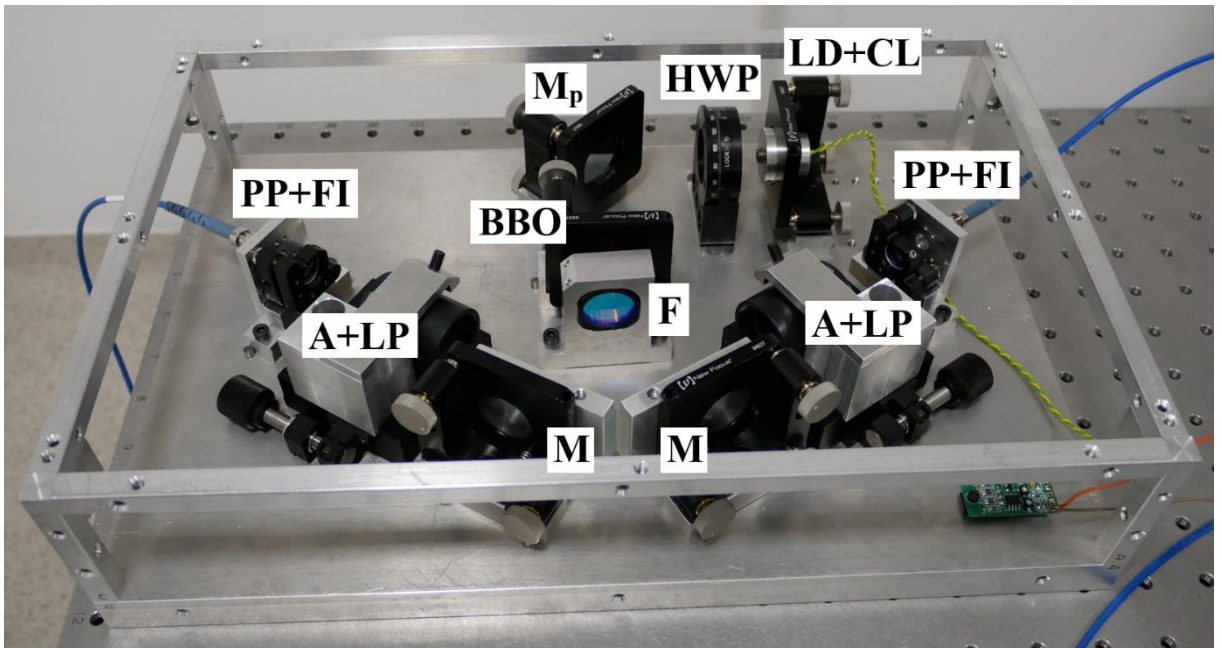


Figure 16. First version of the assembled compact, time-correlated photon-pair source, with SPDC light directly coupled into single-mode, polarization-maintaining fibers.

The alignment process comprises the following two main parts:

- 1) focusing the pump beam into the BBO,
- 2) projecting the image of this focal spot onto the end of the fibers.

To achieve these goals, I needed an appropriate position reference at the location of the crystal. Therefore, I first placed an opaque mask with a $50\ \mu\text{m}$ diameter pinhole at its center into the crystal holder. This aperture approximates the $30\ \mu\text{m}$ size of the diffraction-limited focal spot of the pump, as calculated from NA_p and λ_p . To compensate for the optical length of the crystal, I also positioned equivalent glass plates on both sides of the pinhole, see Figure 17.



Figure 17. Aperture used for the alignment process of the photon pair source. The $50\ \mu\text{m}$ diameter pinhole is located at the center marked by the crosshair. The crosshair serves beam aiming purposes, while the glass plates in front of and behind the aperture provide an equivalent optical length for this device compared to that of the real BBO crystal.

Component name	Abbr.	Supplier, serial number
Pump laser	LD	Roithner LaserTechnik, LD-405-200 MGS
Pump focusing assembly	CL	Roithner LaserTechnik, LDA-38
Half-wave plate	HWP	Newport, 10RP02-48
Nonlinear crystal	BBO	Newlight Photonics, NCBBO5300-405(I)-HA3
Long-pass filter	F	Thorlabs, FELH0600
Folding mirrors	M	Thorlabs, BBSQ1-E03
Fiber-coupling lens pair	LP	ThorLabs, MAP1075150-B
Plane-parallel plate	PP	Edmund Optics, #36-969
Optical fiber	FI	ThorLabs, P1-780PM-FC-2

Table 5. List of optical components with their abbreviations shown in Figure 8 and Figure 16.

Then, by using two $x - y$ tiltable kinematic mounts, I aligned the direction of the pump beam to be parallel to the top of the optical table and focused it on the pinhole. I used a standard power meter (Coherent, FieldMaxII-TO) to find the power maximum of light passing through the aperture. Since the SPDC cone emanates from the spot where the aperture is located, its position had to be conjugate to the fiber inputs. Instead of coupling the down-converted light directly into the fibers, I solved the reverse problem:

I projected the input end of the fibers onto the pinhole using the light of a red He-Ne laser coupled into the polarization-maintaining fibers from their output. By shifting/tilting the M mirrors shown in Figure 8 and using the longitudinal translator of the lens pair (LP), I imaged the fiber input onto the pinhole from the side opposite to the pump. The diffraction spot here was approximately $11\ \mu\text{m}$ (estimated from the fundamental mode diameter of the fiber using Marcuse's equation [28]), which was significantly smaller than the pinhole. For this reason, I could not seek for a maximized throughput; instead, I monitored the far-field symmetry of the beam passing through the aperture to align the focus spot to its center. Due to their significant optical thickness, the filters (F) were left in position throughout this process. To preserve the small operating range of the plane-parallel plates (PP), which can laterally move the focal spot on the fiber input by only $\pm 23\ \mu\text{m}$, I set them orthogonal to the beam and did not adjust them during this phase.

After completing the previous procedure, the aperture was removed and the BBO was put into its position. At this point, based on my consistent and repeatable observations, down-converted photons appeared instantaneously at the fiber outputs. I optimized the conversion efficiency by fine-tuning the pump polarization direction and the tilt of the BBO crystal. Since the rough alignment had been performed with 633 nm He-Ne laser light, the lens pairs (though constituted of achromatic doublets) had to be refocused to account for longitudinal chromatic aberration and maximize fiber-coupling efficiency. Finally, M and PP were carefully adjusted in each arm to maximize the photon flux in one fiber, as well as to optimize the coincidence flux across both fibers.

Coupling a coherent beam into a single-mode fiber requires submicron accuracy at maintaining the input beam at the center of the mode field. In case we have photon pairs, the system becomes even more sensitive to mechanical deformations, since both photons have to be incoupled at the same time. For my first experiments I used a heavy, 20 mm thick solid aluminum plate as a base for the optical setup, the rigidity of which proved to be insufficient, since if the device was moved even a little (tilted or lifted), it had to be slightly realigned. In consequence, I replaced the solid block by a custom-made, aluminum breadboard of 50 mm total thickness with an internal crate structure and 5 mm thick shells at the bottom and top, according to Figure 17.

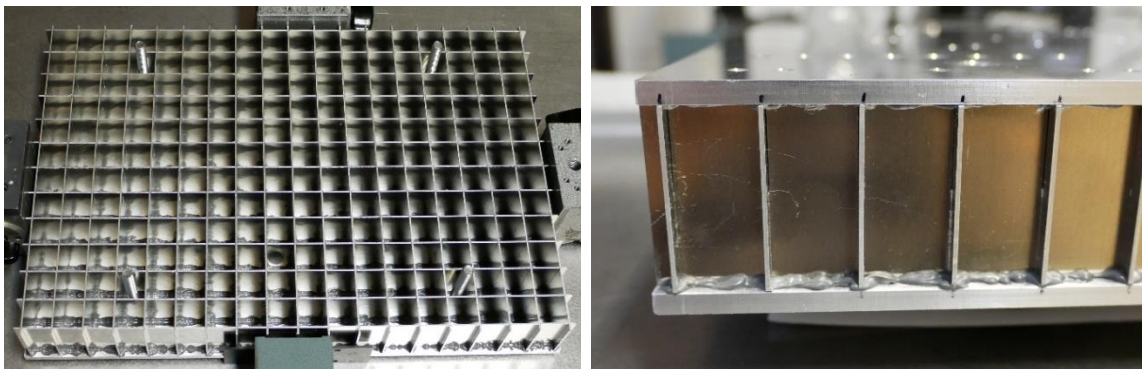


Figure 18. Custom-made stiff base of the fiber-coupled photon pair source.

The measured stiffness (i.e. linear distortion due to an external force) showed a 4.5 ± 0.3 times increment relative to the former solution, simultaneously, the weight decreased by 28%. The assembly is placed into a rack-cabinet compatible box (see Figure 19), with rubber absorbers in between the two in order to isolate it from external shocks. As a result, no consecutive realignment is necessary when moving the system.

To build such a device for laboratory tests - and potentially for field applications - the design and fabrication of numerous custom mechanical parts were required. To provide a glimpse into this process, I have included in the Appendix the manufacturing drawings of the components I personally designed for the source shown in Figure 19.

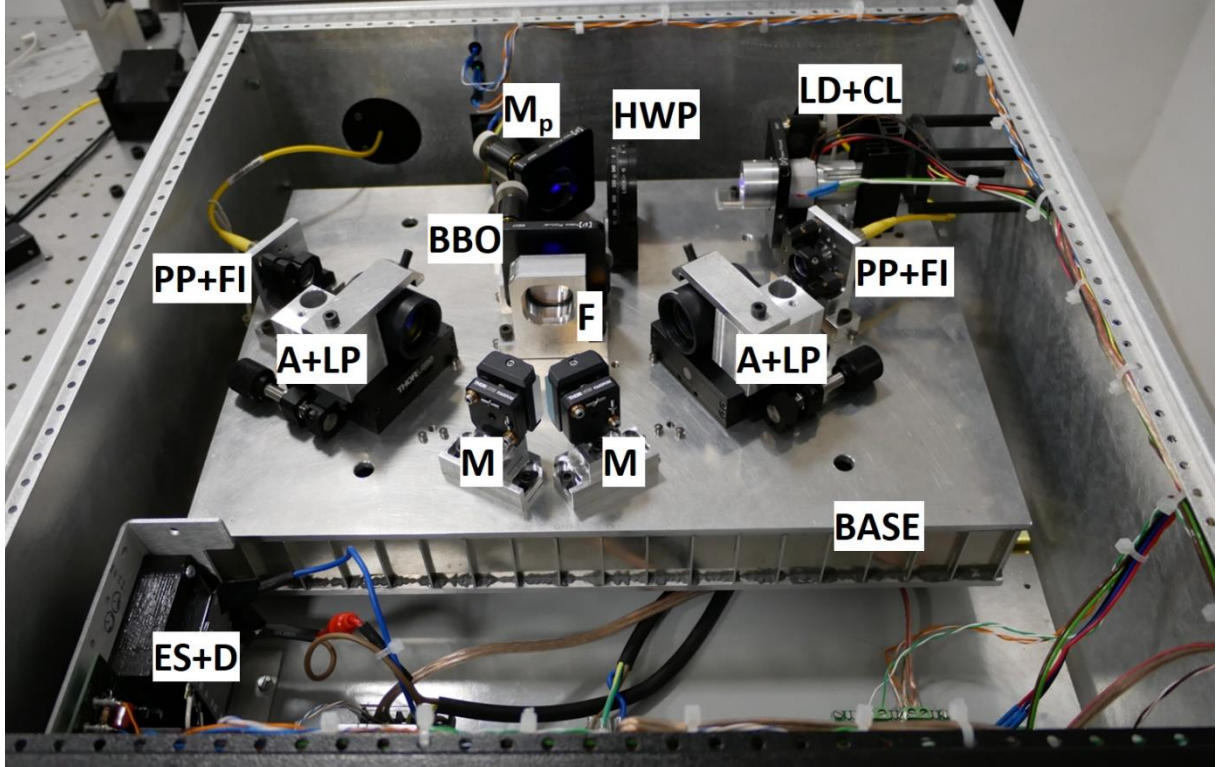


Figure 19. Improved version: Compact, portable, rack cabinet-compatible, time-correlated photon-pair source. BASE: mechanically isolated, stiff base for optical components, ES+D: electronic supply and driver circuits, A+LP: aperture with baffle and fiber-coupling lens pair. Other notations are described above.

Further reconsiderations led to additional improvements. The pump beam is attenuated in two stages: first, originally with two spectral filters (F) and second, with a baffle in the aperture (A) (depicted in Figure 15) before the fiber-coupling optics. The high pump photon rejection $\eta_{ap}(\lambda_p)$ of the baffle allows for using only one filter with 10^{-5} attenuation, instead of the original two filters, by sustaining the ratio between SPDC and random coincidence events at a level greater than 10^{13} . Decreasing the number of filters is beneficial in terms of the heralding ratio (\mathbb{P}_h), which decreases by the square of filter transmittance at λ_s . In the former system F were two long-pass filters with 600 nm cutoff wavelength, allowing the entire spectrum of SPDC light to couple into the fibers. With replacing it by a 810 ± 5 nm bandpass filter I could increase the coherence length of the source. In addition, the application of narrow-band light significantly decreases the effects of chromatic aberrations, which enhances fiber-

coupling efficiency and \mathbb{P}_h as well. However, even small variations in the ambient temperature affect the operation of our pumping laser diode (LD), causing shifts in its peak emission wavelength. Since the transmissive range of the bandpass filter is narrow, these changes would effect the photon fluxes directly. For this reason, in the improved setup I used temperature and current stabilization to maintain the pump wavelength produced by the laser diode at $\lambda_p = 405$ nm by ± 0.1 nm precision. These changes enable versatile operation, and by changing the filter F, one can switch between broad-band (202 nm) and narrow-band (10 nm) operation.

5.5 Measured source performance

For the measurements here I used ID100-type single-photon avalanche diode with the fiber adapters mentioned in Subsection 4.6. The time-tagger electronics was the quTools-made quTAU counter, with a coincidence window of $\tau = 3.24$ ns.

I have already shown in Subsections 5.3 and 5.4, that the signal-to-noise ratio is over 10^{13} , thus in the subsequent calculations I only deal with signal photons and neglect those leaking from the pump into the detectors. In order to distinguish it from the Φ_s photon flux at the fiber outputs, I quantify the rate of detected signal events by the so-called count rate \mathcal{R}_s . Their simple connection is represented by Eq. (27):

$$\Phi_s = \frac{\mathcal{R}_s}{\eta_{\text{det}}(\lambda_s)} \quad (27)$$

The measured value of coincidence flux Φ_s^c is not so straightforward to determine, since the total coincidence rate \mathcal{R}_s^t counted by the detectors also contains random coincidences with a rate of \mathcal{R}_s^r beside the real ones. Correspondingly, the expression for the real coincidence flux is:

$$\Phi_s^c = \frac{\mathcal{R}_s^t - \mathcal{R}_s^r}{\eta_{\text{det}}(\lambda_s)^2}. \quad (28)$$

Random coincidences occur when two independent photons hit the two detectors within the same τ time window. I consider those photons as independent, whose pair were not coupled into the other fiber. Using Poisson statistics again (detailed in Subsection 10.1 of the Appendix), the expected value of such detected photons in a τ time frame is $\mathcal{R}_s \cdot (1 - \mathbb{P}_h \cdot \eta_{\text{det}}) \cdot \tau$. The value of \mathcal{R}_s^r can be derived, taking the following form:

$$\mathcal{R}_s^r = (1 - \exp(-\mathcal{R}_s \cdot (1 - \mathbb{P}_h \cdot \eta_{\text{det}}) \cdot \tau))^2 \cdot \frac{1}{\tau}. \quad (29)$$

However, the measured value of the heralding ratio \mathbb{P}_h is unknown at this point. The expression by which it can be calculated from raw measurement data is given by Eq. (30).

$$\mathbb{P}_h = \frac{\mathcal{R}_s^t - \mathcal{R}_s^r}{\mathcal{R}_s \cdot \eta_{\text{det}}(\lambda_s)} \quad (30)$$

From this and Eq. (29), one can see that \mathcal{R}_s^r and \mathbb{P}_h are coupled quantities. In order to determine both, I solved the resulting transcendent system of equations by successive approximation.

Table 6 provides the photon and coincidence fluxes calculated from the measured count rates for both the initial broadband and the improved narrowband filtering configurations. These values are compared to the optimal simulated results. Examining Φ_s , it is evident that the total coupling efficiency [i.e., the product of all efficiency terms in Eq. (22)] matches the design value with less than 7% relative error.

However, both Φ_s^c and \mathbb{P}_h fall short of expectations. The reason for this discrepancy is that the design process was performed for a single wavelength $\lambda_s = 810$ nm, while the source, with broadband filtering applied, produces photons over a wide spectral range, as depicted in Figure 20. Therefore, the deviation of Φ_s^c and \mathbb{P}_h from the measured values may be attributed to any wavelength-dependent efficiency terms in Eq. (23), that are not spectrally symmetric around the 810 nm wavelength of the degenerate photon state, along with the wavelength dependence of the SPAD detectors. I have not yet studied these effects in detail, but a thorough examination of the spectral behavior could be part of subsequent research.

On the other hand, the 10 nm wavelength filtering reduces the useful photon-pair spectrum, naturally decreasing both the signal (Φ_s) and coincidence flux (Φ_s^c), while nearly doubling \mathbb{P}_h . This increased value approximates the simulated 45% within the margin of my measurement error. The explanation is that the narrowband operational mode better aligns with the design conditions, thereby minimizing the above detailed spectrally asymmetric responses of the apparatus.

	Φ_s [kcps/mW]	Φ_s^c [kcps/mW]	\mathbb{P}_h [%]	Bandwidth [nm]
Simulated	682	307	45	0
Measured with 600 nm longpass	636 ± 95	130 ± 39	20 ± 3	202
Measured with 810 ± 5 nm bandpass	17.3 ± 2.6	6.8 ± 1.1	39 ± 6	10

Table 6. Simulated and measured flux values at the single-mode fiber outputs, normalized to pump power. The significant difference between measured and simulated values of Φ_s^c and \mathbb{P}_h originates from the fact that the calculations were performed for monochromatic down-converted light of λ_s wavelength.

I performed a spectral measurement at the fiber outputs, where the spectral density $S(\lambda)$ is normalized to the pump power, as shown in Eq. (31). The curve was recorded using a custom-made, wavelength- and power-calibrated spectrometer, which consists of a reflective diffraction grating with 600 grooves/mm and a SPAD detector. The obtained result may initially seem unrealistic, but the explanation is straightforward. Due to the focusing of the pump beam, angular spectrum components spread in the BBO crystal at a finite solid angle, allowing type-I phase-matching to occur over an extended wavelength range. In this case, the range is remarkably wide, with $\Delta\lambda_{\text{FWHM}} = 202$ nm.

$$S(\lambda) \equiv \frac{d\Phi_s}{d\lambda} \cdot \frac{1}{P_p} \quad (31)$$

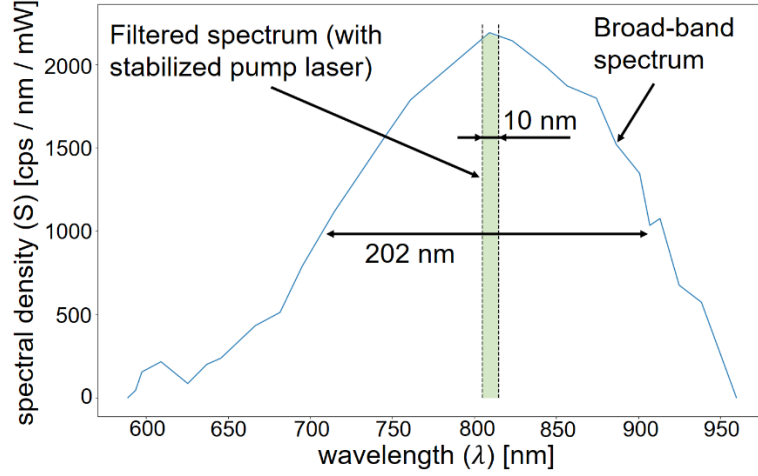


Figure 20. Power spectral density of the photon source with broad-band and narrow-band filtering, measured at the fiber output, normalized to pump power.

For narrow-band filtering, the indistinguishability between parts of the generated photon pairs was experimentally justified by Hong-Ou-Mandel (HOM) interference [61]. Spatial overlap of the interfering modes is a critical setting for HOM interference. Therefore, I chose to use a single-mode fiber-based 50% beam splitter (Thorlabs, TW805R5F2), which ensures that both incident fields occupy the same spatial mode (i.e., the propagating LP_{01} mode in the fiber). Polarization overlap was established by adjusting the polarization of one input port using a fiber polarization controller.

The other critical parameter of HOM interference is the temporal overlap of the incident photons. The interference occurs within the coherence length of the generated photon pair, which, with the 10 nm filter applied, is $65.6 \mu\text{m}$. This very short coherence length corresponds to a 0.219 ps coherence time, which is unresolved by the detection electronics (having a minimal jitter of ~ 71 ps). Therefore, I designed a custom optical retarder, depicted in Figure 21, consisting of two right-angle prisms and a piezoelectric linear actuator (Newport, AG-LS25-27P). The achievable minimal retardation is $0.2 \mu\text{m}$, corresponding to a 0.67 fs temporal delay between the two inputs. This resolution is sufficient to record the quantum interference. The measured HOM dip is depicted in Figure 22 and has a visibility of 67%.

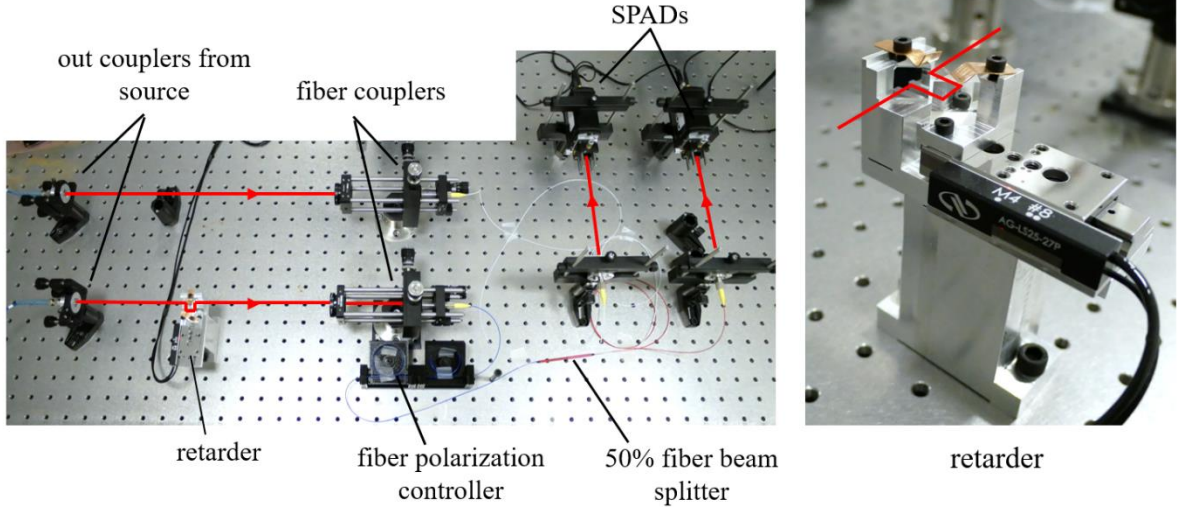


Figure 21. Setup of the Hong-Ou-Mandel measurement performed on the photon pair source. On the right is the custom made optical retarder.

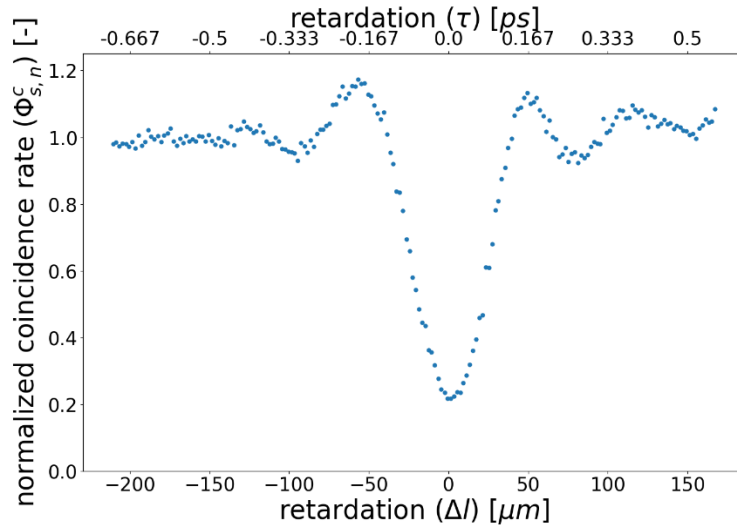


Figure 22. Hong-Ou-Mandel interference of the correlated photon pairs, with 10 nm filtering at 810 nm. The coincidence rate $\Phi_{s,n}^c$ is normalized by $\Phi_s^c/2$.

In Table 7, I have collected the most important characteristics of other well-documented approaches that utilize classical optical elements and critical type-I phase matching in bulk crystals, similar to my setup. However, direct comparison of my results with these setups is not straightforward, as they differ in many respects, such as geometry, crystal material, spectral bandwidth, etc. For this reason, I re-calculated certain values to align with my case, as indicated in the table by superscripts a) and b).

Wide-band sources of this type are scarce; I found only one such source [58]. Its heralding ratio is lower than mine, while its coincidence flux was not accessible. I found two narrow-band sources in the literature [51][57], which can be compared with my results when narrow-band filtering is applied. Among the sources I found, all have a lower \mathbb{P}_h except for one reference [57], where the authors coupled only a small portion

of the SPDC ring into the fiber, thereby losing photons. Applying the bandpass filter in my measurement led to similar results, causing a drop in the coincidence flux.

One of the two sources [57] with a measured coincidence flux has a smaller flux than mine, while the other [51] has a much larger flux. However, in the latter case, the authors used a collinear setup, which allows for more efficient fiber coupling, but their source cannot produce photons in the frequency-degenerate quantum state. It is also worth noting that none of the other systems have been reported to be as compact or portable as mine. Such a source can be utilized in quantum cryptography based on the BB84 protocol [59]. Additionally, its large bandwidth implies an ultra-short temporal correlation time between photon pairs, which is desirable for applications like distant clock synchronization [60].

Ref.	Type	Crystal	Φ_s^c [kcps/mW]	\mathbb{P}_h [%]	Bandwidth
My work (600 nm longpass)	Noncollinear, degenerate	BBO 3 mm	130 ± 39	20 ± 3	92.4 THz (202 nm)
My work (810±5 nm bandpass)			6.8 ± 1.1	39 ± 6	4.57 THz (10 nm)
[51]	Collinear, nondegenerate	BBO 10 mm	184.6 ^a	33.8	N.A.
[57]	Noncollinear, degenerate	BiBO 0.6 mm	5.2 ± 0.11^b	68.8	13.7 THz (23 nm)
[58]	Collinear, degenerate	BBO 2 mm	N.A.	17 ± 2	99 THz (139 nm)

Table 7. Comparison of my source with similar approaches in the literature, all utilizing critical type-I phase matching. \mathbb{P}_h is calculated to account for all optical losses in each setup. a) The flux is linearly proportional to the crystal length [51], so Φ_s^c is normalized to our 3 mm long crystal based on Fig. 6 in Kuniyil et. al. [51]. b) In case of flat-top spectral filtering applied by Guilbert et. al. [57] Φ_s^c is normalized to both crystal length and to 10 nm bandwidth. Note that the nonlinear coefficient of BiBO is greater than that of BBO [57].

5.6 Summary and Thesis 1

The present section investigated the possibilities for coupling the down-converted light of a type-I BBO crystal into polarization-maintaining, single-mode fibers. I have presented an efficient method that collects 73% of the photons in the SPDC light cone and achieves a fiber-coupling efficiency of 51%. The key to my approach was the appropriate focusing of the pump beam into the nonlinear crystal. Experimental results show that the total coupling efficiency is within 7% of the design goal, which is a reasonable agreement.

The setup consists solely of commercial elements and requires a straightforward and stable alignment process, making it a cost-efficient photon source alternative. Its 202 nm-wide spectrum is advantageous for applications that require a very short coherence length, such as those relying on short correlation times between photon pairs. The source can operate in either broad- or narrowband mode by replacing filter F. It is

assembled in a rack cabinet-compatible box on a mechanically isolated, stiff base. Additionally, it includes a temperature- and current-stabilized diode laser as the pump, ensuring a compact and portable design.

Thesis 1:

I designed and built a compact, portable, single-mode fiber-coupled correlated photon pair source based on noncollinear, frequency-degenerate spontaneous parametric down-conversion utilizing critical type-I phase matching, that has a higher photon pair flux ($1.3 \cdot 10^5$ pairs/s/mW), and a larger bandwidth (202 nm) compared to sources of similar approach. [H1],[H2],[H3]

6 Conversion of transverse momentum correlation into polarization entanglement

Sources of entangled photon pairs play a crucial role in both demonstrating and practically utilizing many quantum-optical phenomena. Today, their primary application is in quantum cryptography, as many secure key distribution protocols rely on entanglement [1][2][44], a typical manifestation of temporal quantum correlation. Other promising areas include optical quantum computing [3][62] and the distribution of entanglement between quantum computers [4][5]. Most of these applications require convenient and reliable sources with similar specifications, as well as photon pairs coupled into single-mode optical fibers.

A broad range of entangled photon pair generation methods exist, providing temporal correlation between various photon properties such as position, momentum, energy, phase, or polarization. Among these, polarization entanglement (with photon pairs being in a Bell state) appears to be the most useful for quantum cryptography, which is the primary focus of the research group. Polarization entanglement can be achieved via SPDC in several ways. One method utilizes momentum correlation in a non-collinear type-II phase-matching configuration by collecting photons at the intersection points of two orthogonally polarized light cones [34], as seen in Figure 23.

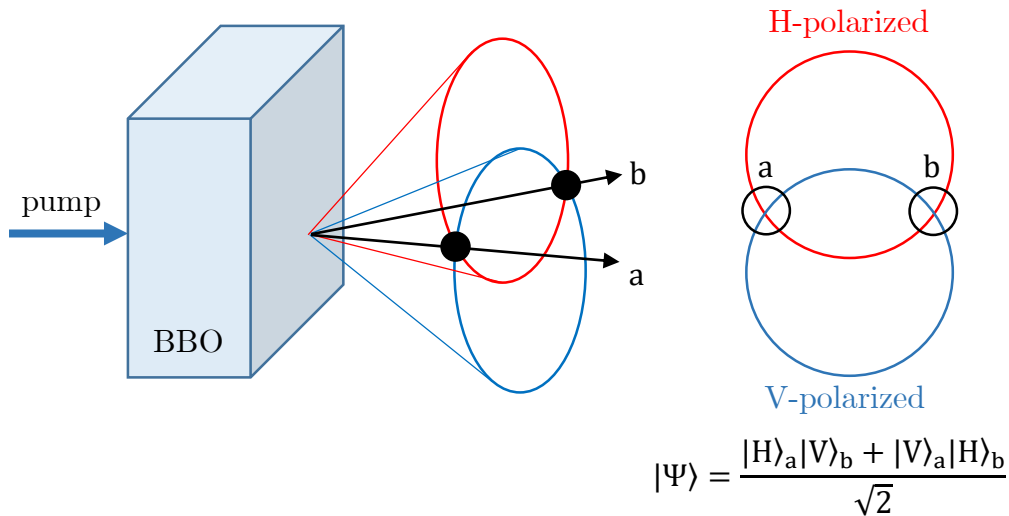


Figure 23. Obtaining polarization entanglement in non-collinear type-II SPDC. On the right side is the front view of the two cones, perpendicular to the pump. The black circles represent the collection apertures of polarization entangled pairs.

This method is the oldest one, offering a rather low conversion efficiency. Another approach involves generating SPDC in two sequential, independent crystals [35]-[63], which increases conversion and collection efficiency but requires twice the amount of nonlinear material and precise alignment of the two crystals relative to each other. A different strategy involves pumping the same crystal with multiple beams coherently [36]-[65], though this method presents significant challenges in aligning the beams and maintaining their relative phase. Another technique transforms the birth-position correlation of photon pairs into polarization entanglement using a wavefront-splitting

interferometer [66]. While this approach provides a robust setup, its collinear configuration prevents the separation of frequency-degenerate pairs.

Since frequency degeneracy is a key requirement in many applications, particularly in linear optical quantum computing and distributed quantum networks, both requiring sources of identical photons [67][68], I developed a novel setup that upgrades the above-described source. My design preserves the stability of wavefront-splitting interferometry while also allowing for frequency degeneracy.

This section presents how momentum correlation can be transformed into polarization entanglement in a non-collinear type-I phase-matching configuration using a wavefront-splitting interferometer. The concept and a specific demonstrative implementation of this method are detailed here, resulting in a single-mode fiber-coupled polarization-entangled photon pair source. The method does not inherently separate the optical paths of different polarization states, eliminating the need for active interferometric stabilization. Along with a description of the equipment, a straightforward alignment process is introduced for generating any of the Bell states on the detection side. Photon and coincidence rates, density matrix, and state fidelity of the source are measured.

6.1 Presentation of the physical concept

Besides energy conservation, photons generated in the type-I SPDC process must also obey momentum conservation, i.e., phase-matching. In a non-collinear setup, the wave function of the resulting photon pairs propagates in a cone centered on the pump axis, with both photons having the same polarization. The members of these pairs can be separated based on transverse momentum by collecting them with two apertures placed in the far field of the nonlinear crystal at axially symmetric positions along the cone, as previously described. Here, "transverse" refers to a direction orthogonal to the pump axis.

Considering the transverse momentum of SPDC photons, we can categorize them into two states, $|k_u\rangle$ and $|k_l\rangle$, propagating in the upper and lower parts of the light cone, respectively (i.e., above or below the dashed meridional line in Figure 24). The corresponding momentum-correlated wave function is expressed as:

$$|\psi\rangle = \frac{|k_u\rangle|k_l\rangle \otimes |h\rangle|h\rangle + |k_l\rangle|k_u\rangle \otimes |h\rangle|h\rangle}{\sqrt{2}}, \quad (32)$$

where $|h\rangle$ represents the horizontal polarization of the SPDC cone.

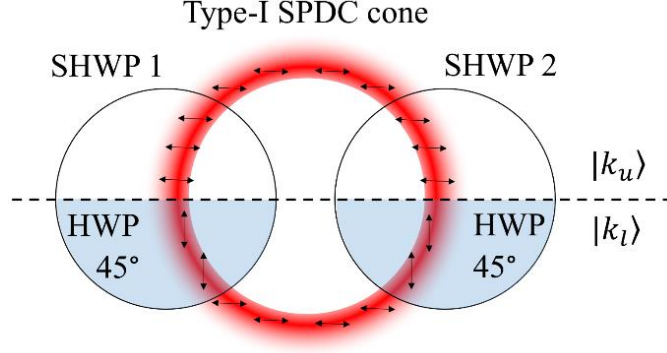


Figure 24. Segmented half-wave plates (SHWP) in the far-field of the SPDC light source, both having two sections. The lower one contains a quartz half-wave plate (HWP) oriented at 45° with respect to the horizontal polarization of down-converted photons, and the upper part is isotropic fused silica of the same thickness. In consequence, the polarization of light propagating through the upper segment in $|k_u\rangle$ momentum state remains unchanged, while in the lower segment (i.e. $|k_l\rangle$ state) it is transformed to vertical direction. Arrows indicate the direction of polarization along the SPDC cone.

In my design, illustrated in Figure 24, a segmented half-wave plate (SHWP) is placed in front of both apertures, each consisting of two equal-area sections. The lower half contains a zero-order quartz half-wave plate (HWP) with its optic axis oriented at 45° relative to the $|h\rangle$ horizontal polarization of the SPDC cone. The upper section is filled with fused silica of equivalent optical thickness to that of the quartz, compensating for the phase shift accumulated by the beam passing through the lower section. The operation of these rotated HWPs is best described in the basis of the diagonal $|d\rangle$ and anti-diagonal $|a\rangle$ state vectors. Retarders introduce a phase shift α between these states, which is π in the case of ideal half-wave plates:

$$|h\rangle \rightarrow |d\rangle + e^{i\alpha}|a\rangle = |d\rangle - |a\rangle = |v\rangle, \quad (33)$$

meaning that a half-wave retarder transforms $|h\rangle$ into vertical polarization $|v\rangle$. From Eq. (33), it follows that both orientation and retardation accuracy are crucial, as any deviation from the optimal settings deteriorates state fidelity. The wave function $|\psi'\rangle$ after the SHWPs is given by Eq. (34):

$$|\psi'\rangle = \frac{|k_u\rangle|k_l\rangle \otimes |h\rangle|v\rangle + |k_l\rangle|k_u\rangle \otimes |v\rangle|h\rangle}{\sqrt{2}} \quad (34)$$

After passing through both apertures, the photons are focused and coupled into single-mode optical fibers using appropriate imaging systems. The mode overlap between the focused $|k_u\rangle_1 \otimes |h\rangle$ SHWP1 upper segment, and the $|H\rangle$ horizontally polarized propagating mode in the fiber can be described as a complex c_{h1} coupling amplitude:

$$c_{h1} = \langle H | (|k_u\rangle_1 \otimes |h\rangle). \quad (35)$$

A similar expression holds for the vertically polarized lower segment of SHWP1, as well as for the two segments of SHWP2, with coupling amplitudes c_{v1} , c_{h2} and c_{v2} , respectively. The absolute squares of these amplitudes determine the fiber coupling efficiency of each segment. Using these definitions, the fiber-coupled wave function $|\Psi\rangle$ can be expressed as:

$$|\Psi\rangle = \frac{c_{h1}|H\rangle c_{v2}|V\rangle + c_{v1}|V\rangle c_{h2}|H\rangle}{\sqrt{|c_{h1}c_{v2}|^2 + |c_{v1}c_{h2}|^2}}, \quad (36)$$

where $|V\rangle$ represents the vertically polarized fiber mode. Eq. (36) can be interpreted as the focusing lenses coherently couple the $|h\rangle|v\rangle$ and $|v\rangle|h\rangle$ states into the fibers with amplitudes $c_{h1}c_{v2}$ and $c_{v1}c_{h2}$, respectively. For simplification, I introduce:

$$ce^{i\Delta\phi} \equiv \frac{c_{v1}c_{h2}}{c_{h1}c_{v2}} \quad (37)$$

$$\phi = \arg(c_{h1}c_{v2}) \quad (38)$$

Using these definitions, the entangled state can be rewritten as:

$$|\Psi\rangle = e^{i\phi} \frac{|H\rangle|V\rangle + ce^{i\Delta\phi}|V\rangle|H\rangle}{\sqrt{1+c^2}}. \quad (39)$$

It is important to note that ϕ does not affect the operation of the photon source and will therefore not be considered further in this discussion.

6.2 Experimental setup

The schematic illustration of the fiber coupling and measurement system is shown in Figure 25. The source setup remains the same as described in Section 5. Distinct differences from my previous implementation are the use of standard single-mode fibers instead of polarization-maintaining ones to minimize phase shifts between polarization modes, and an increased pump power of 150 mW.

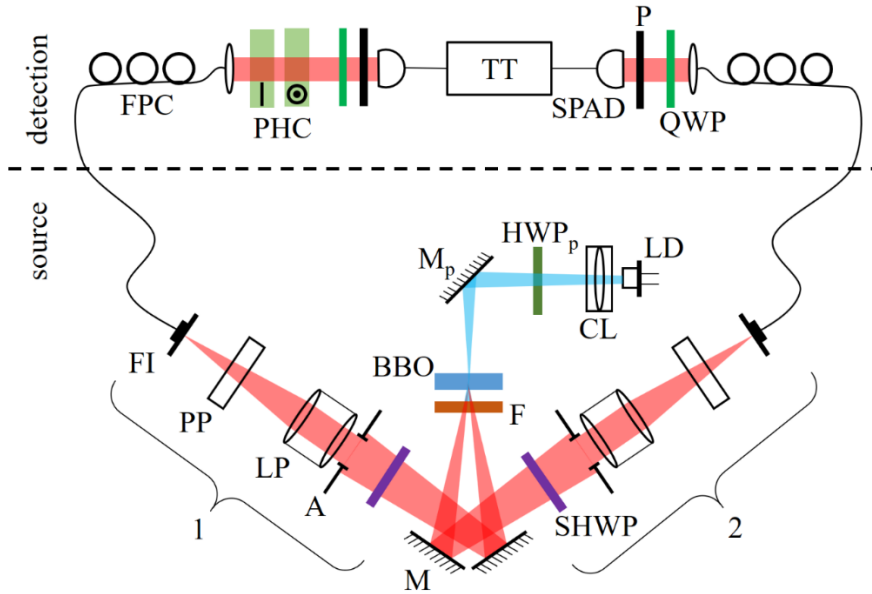


Figure 25. Schematics of the experimental setup. Blue and red beams indicate pump and down-converted light, respectively. LD: laser diode, CL: focusing assembly, M_p : pump fold mirror, HWP_p : half-wave plate for the pump, F: spectral filter, M: dielectric “hot” mirror (reflects wavelengths between 750-1100 nm), SHWP: segmented half-wave plate, A: aperture, LP: relaying lens pair, PP: plane-parallel plate, FI: fiber input, FPC: fiber polarization controller, PHC: anisotropic phase compensator with optical axis indicated, SPAD: single-photon avalanche detector, TT: time tagger, QWP: quarter-wave plate, P: linear polarizer. The implementation of the source is the one depicted in Figure 19, but supplemented with the SHWP-s.

6.2.1 Segmented Half-Wave Plates

Since segmented half-wave plates were not commercially available, they were fabricated in the optical workshop of the Department of Atomic Physics, primarily for demonstrative purposes. I designed 3 mm-thick, 20×20 mm rectangular glass slabs as substrates, onto which a properly oriented single-crystal quartz and a fused silica plate were cemented in adjacent positions. This construction creates a sharp boundary between the two parts, minimizing photon loss. Both plates were of 10×20 mm size and were ground and polished together to ensure identical thicknesses and a diffraction-limited transmitted wavefront. To achieve true zero-order phase retarders on 810 nm, I determined a target thickness of 45.5 μm. Multiple SHWPs were manufactured, and I characterized them using an 809 nm laser (Coherent Surelock LM-808-PLR-120-3) and linear polarizers to determine their thickness and orientation.

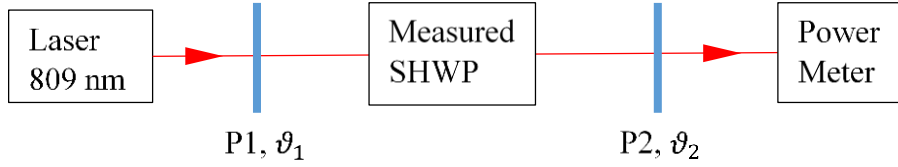


Figure 26. Measurement setup for determining the thickness and orientation of the SHWPs. $P1$ and $P2$ are linear polarizers rotated at angles ϑ_1 and ϑ_2 .

I positioned the measured SHWP with its optical axis approximately diagonal. Then, I rotated $P1$ to around 45° and fine-tuned it while adjusting $P2$ around 315° until the transmitted intensity reached a minimum. This ensured that the incident linear polarization was aligned with one of the plate’s polarization eigenstates. Next, I rotated $P1$ back so that the incident polarization was at 45° relative to the optical axis of the plate. By rotating $P2$ and analyzing the transmitted intensity, I could characterize the phase shift. It can be shown that for a uniaxial birefringent phase plate with an arbitrary phase shift φ , the transmitted intensity of the setup follows the equation:

$$I(\varphi, \vartheta_2) = I_0 \cdot (1 + \cos \varphi (2 \cos^2 \vartheta_2 - 1)). \quad (40)$$

I fitted Eq. (40) to the measured intensity data. Using the ordinary and extraordinary refractive indices of quartz at $\lambda = 809$ nm, $n_{o,\text{quartz}} = 1.5382$ and $n_{e,\text{quartz}} = 1.5470$, with a difference of $\Delta n_{\text{quartz}} = 0.0089$, the thickness d of the phase plate was determined by using the following equation:

$$d = \frac{\varphi \lambda}{2\pi \cdot \Delta n}. \quad (41)$$

SHWP	φ [π]	d [μm]	Δd [μm]
1	1.017	46.2	0.7
2	0.964	43.8	-1.7
3	0.962	43.7	-1.8

Table 8. Measured phase shift at 809 nm and thickness of the HWP segment of the SHWP-s

According to Table 8, the manufactured pieces met the design thickness with an accuracy of $\pm 2 \mu\text{m}$. Based on these evaluations, the two similar plates (2. and 3.) were selected for the source. The consequences of fabrication errors and further measurements of the SHWPs, assessed through their performance in the source, are discussed in Subsection 6.4.

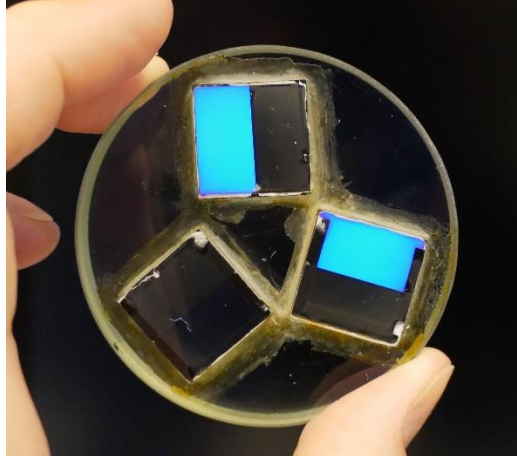


Figure 27. Image of the SHWPs during the manufacturing process. At the time the image was taken, their thickness was approximately $68 \mu\text{m}$. The background is a polarized white LCD screen, and the SHWPs were photographed through an orthogonal polarizing filter. The two SHWPs with optical axes approximately diagonal to the screen polarization rotated the blue component of the screen light, allowing it to be transmitted through the second polarizer. The completely black SHWP has its optical axes parallel to the screen polarization.

6.2.2 Polarization Control

Polarization had to be controlled in the experimental setup in two ways: rotating the linear polarization basis to ensure consistency between the source and detection sides, and compensating for the phase shift of the entangled state. I separated these adjustments. The FPCs shown in Figure 25 were used for polarization rotation, while phase compensation was achieved using the anisotropic phase compensator (PHC). This latter element consists of two birefringent lithium-niobate (LN) crystals of equal thickness d , placed sequentially with their optical surfaces perpendicular to the incident beam. Although the plates are parallel, their optical axes are oriented perpendicularly to each other. As a result, the phase shift introduced by the first crystal is canceled by the second. However, tilting one of the crystals around its optic axis does not affect the extraordinary refractive index, but it does alter the optical path length in that crystal. Consequently, the resulting phase shift $\Delta\varphi$ becomes nonzero. In this manner, the tilt angle α determines the overall phase shift introduced by the PHC.

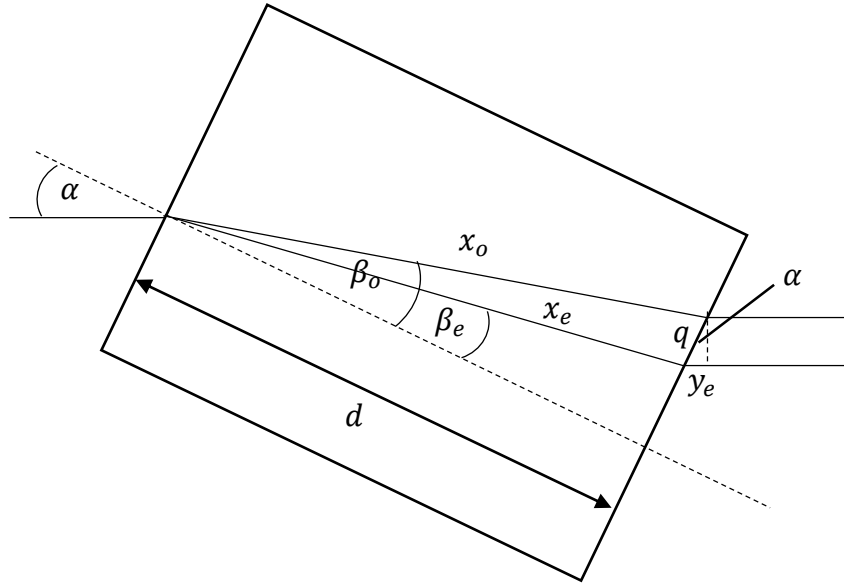


Figure 28. Optical path of the ordinary and extraordinary beams in a positive birefringent material, for α angle of incidence.

Given a positively birefringent material ($n_e > n_o$), the corresponding refraction angles follow $\beta_e < \beta_o$, and Snell's law gives:

$$\beta_{o,e} = \arcsin\left(\frac{\sin \alpha}{n_{o,e}}\right) \quad (42)$$

The path length of the beam inside the crystal is:

$$x_{o,e} = \frac{d}{\cos \beta_{o,e}} \quad (43)$$

The extraordinary beam exits the crystal at a different position than the ordinary beam, resulting in an additional path in air:

$$\begin{aligned} y_e &= q \cdot \sin \alpha \\ q &= d \cdot (\tan \beta_o - \tan \beta_e) \\ y_e &= d \cdot (\tan \beta_o - \tan \beta_e) \cdot \sin \alpha \end{aligned} \quad (44)$$

The optical path length is calculated up to the point where the ordinary beam exits the material. Beyond this point, both beams propagate in air and accumulate no further phase difference.

$$OPL_o = x_o n_o = \frac{d n_o}{\cos \beta_o} \quad (45)$$

$$OPL_e = x_e n_e + y_e = \frac{d n_e}{\cos \beta_e} + d \cdot (\tan \beta_o - \tan \beta_e) \cdot \sin \alpha \quad (46)$$

The optical path difference, and thus the phase shift $\Delta\varphi$ between the two polarization components, is:

$$\Delta\varphi = \frac{2\pi}{\lambda} (OPL_e - OPL_o) = \frac{2\pi d}{\lambda} \left[\frac{n_e}{\cos \beta_e} + d \cdot (\tan \beta_o - \tan \beta_e) \cdot \sin \alpha - \frac{n_o}{\cos \beta_o} \right] \quad (47)$$

To adjust the phase over the full range $\Delta\varphi \in [0, 2\pi]$, I used lithium niobate (LN), a negatively birefringent material. In this case, the roles of OPL_o and OPL_e are reversed compared to those in Figure 28. By substituting the refractive indices of LN [69] at 810 nm $n_{o, \text{LN}} = 2.2540$, $n_{e, \text{LN}} = 2.1744$ along with the crystal thickness $d = 1.5$ mm into Eq. (47), I calculated the necessary tilt range of $\alpha \in [0, 9^\circ]$.

The PHC was designed for both manual and automated operation in a detection system at BME VIK. To enable this dual functionality, I equipped its mounting mechanics with a motorized adjuster. The final implementation of the PHC is shown in Figure 29.

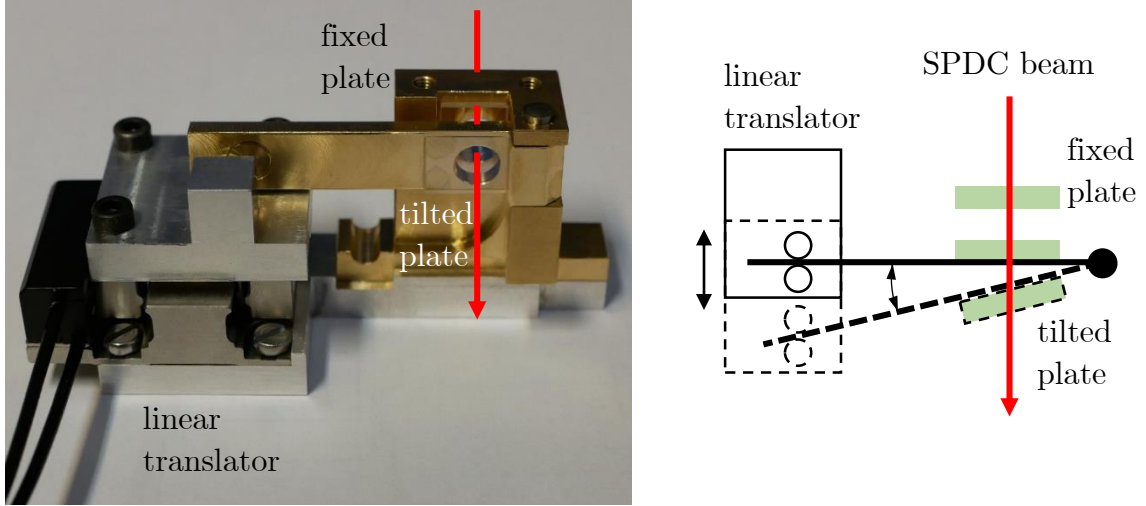


Figure 29. Realization of the PHC in Figure 25, and its schematic working principle.

Due to the high refractive index of LN, it exhibits a high average reflectance of $R_{\text{LN}} = 14.3\%$. As the PHC has four optical surfaces, this results in a low overall transmittance of $T_{\text{PHC}} = 53.9\%$. Since minimizing losses is crucial for the detection of correlated photon pairs, I designed an anti-reflection coating using fused silica with a nominal thickness of 139 nm [70]. Theoretically, this reduces the single-surface reflectance to 0.5%. The coatings were fabricated at ELI-ALPS¹. According to measurements, the average reflectance of the coated surfaces was reduced to $R'_{\text{LN}} = 0.9\%$ at 810 nm, significantly increasing the overall device transmittance to $T'_{\text{PHC}} = 96.4\%$.

6.3 Alignment process

Strictly speaking, Eq. (39) holds only at the fiber input. Losses can reduce the magnitude of c if they occur asymmetrically in the two fibers, but based on manufacturing tolerances, I consider these effects negligible. Stress-induced anisotropy and axial twisting of the fibers act together as an arbitrary unitary polarization transformation, which influences both $\Delta\varphi$ and the polarization correlation basis. These effects can be exploited to prepare the desired Bell state at the detection side using the FPCs and the PHC. A key advantage of my wavefront-splitting interferometer is that $\Delta\varphi$ remains insensitive to any optical path length differences between the arms,

¹ ELI-ALPS, ELI-HU Non-Profit Limited, Wolfgang Sandner u. 3, H-6728 Szeged, Hungary

including those caused by mechanical vibrations or thermal expansion. Therefore, only time-dependent perturbations inside the fibers require compensation, and no active stabilization is needed in the source itself.

I set the measurement basis for the desired Bell state at the detection side. Since measurements in different Bell states can be performed using simple polarization transformations, I present the adjustment procedure for a single example: the $|\Psi^-\rangle$ (negatively anti-correlated) Bell state, where $\Delta\varphi = \pi$ and $c = 1.0$ in Eq. (39). Thanks to the wavefront-splitting interferometry used in the source, this adjustment is relatively straightforward and requires only two steps.

Step 1: I begin by configuring the polarization analyzers (depicted in Figure 25) — each consisting of a quarter-wave plate (QWP) and a linear polarizer (P) — in front of the detectors to exclusively measure the $|V\rangle$ state. I then cover the lower part of both SHWPs and tune the fiber polarization controllers (FPCs) to minimize the detector counts on both sides. This ensures that the entire system, including the fibers, transforms the polarization of light incident on the upper segments of the SHWPs into the $|H\rangle$ state. The lower segments of the SHWPs inherently generate an orthogonal polarization with respect to the upper (as long as the transformation introduced by the fibers is unitary), which in this case corresponds to $|V\rangle$. (Setting the linear polarization on one detector orthogonal relative to the other corresponds to the adjustment of a correlated Bell state.) Although the appropriate polarization basis is now established, the adjustment of $\Delta\varphi$ remains necessary.

Step 2: I begin by removing the baffles that cover the lower halves of the SHWPs. Next, both polarization analyzers are reoriented to measure the $|DD\rangle$ state. In this configuration, I fine-tune the phase $\Delta\varphi$ using the PHC, as described previously, until the coincidence counts are minimized — corresponding to $\Delta\varphi = \pi$. (Maximum coincidence in the $|DD\rangle$ state would indicate $\Delta\varphi = 0$.)

The source is modular with respect to both the bandwidth of the generated photon pairs and the presence of polarization entanglement. One can easily reconfigure the setup by replacing the F filter or inserting/removing the SHWPs. Only minor realignment is required, involving the adjustment of the focus position of the LP lenses and the tilt of the PP plane-parallel plates placed in front of the fiber inputs (see Section 5.4).

6.4 Measured source performance

I measured several key properties of the demonstrator device in various modes of operation. All values listed in Table 9 were determined at the fiber outputs and were corrected for detector efficiency, as if measured with detectors of 100% efficiency. The details of this correction are provided in Section 5.5.

Filtering	Polarization entanglement	Φ_s [kcps/mW]	Φ_s^c [kcps/mW]	\mathbb{P}_h [%]	Bandwidth [nm]
600 nm longpass	No	636 ± 95	130 ± 39	20 ± 3	202
810 ± 5 nm bandpass	No	17.3 ± 2.6	6.8 ± 1.1	39 ± 6	10
810 ± 5 nm bandpass	Yes	8.33 ± 1.27	1.47 ± 0.23	17 ± 3	10

Table 9. Optical properties of the photon source in different operational modes. Photon flux Φ_s , coincidence flux Φ_s^c and heralding ratio \mathbb{P}_h are measured at the single-mode fiber outputs, normalized to pump power. All values are corrected for detector efficiency, the errors indicated correspond to $1 \times$ standard deviation.

The results clearly show that spectral filtering improves the heralding ratio \mathbb{P}_h , the explanation of which originates in losses. Absorption, scattering, reflection, and low fiber-coupling efficiency all contribute to a decrease in \mathbb{P}_h , but in my setup, the coupling efficiency has by far the largest impact. Even in achromatic systems, some residual chromatic aberration is present; however, the wavefunction of narrowband photons can be more effectively focused onto the fiber inputs. This leads to improved coupling efficiency and, consequently, a higher \mathbb{P}_h .

The presence of the SHWPs similarly decreases the heralding efficiency. The segmented half-wave plates bisect the apertures, causing the upper and lower halves to couple to orthogonal polarization modes independently. This results in a reduction in coupling efficiency, as the focus spot size of the LP lenses doubles in the vertical direction due to diffraction by the smaller apertures. In Section 5.2, I calculated a fiber-coupling efficiency of 50.9% for a light cone section covering the entire aperture A, whereas the same calculation yielded 23.4% for a half-aperture. Since the heralding efficiency and Φ_s photon flux have a linear, and the Φ_s^c coincidence flux has a quadratic dependence on the fiber-coupling efficiency, I expected Φ_s and \mathbb{P}_h to drop to 46.0%, while Φ_s^c would decrease to 21.1% of their original values when inserting the SHWPs. These changes agree with the values found in Table 9, within the error margin, confirming that the ZEMAX simulation provides a plausible explanation for my experimental observations.

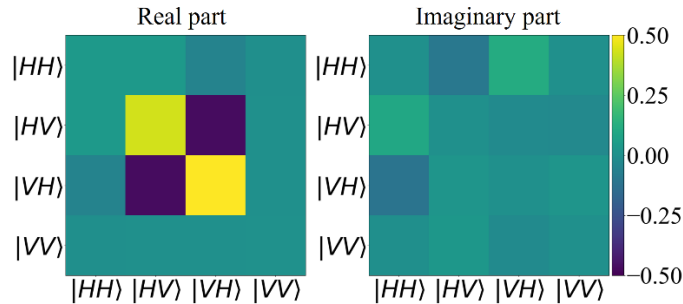


Figure 30. Measured ρ density matrix of the generated polarization entangled state.

I also measured the ρ density matrix of the system. For this, I adjusted the setup to produce the previously mentioned $|\Psi^-\rangle$ Bell state and performed a full state

tomography [24]. The results are depicted in Figure 30. The state fidelity towards the $|\Psi^-\rangle$ state, with the corresponding theoretical density matrix $\sigma = |\Psi^-\rangle\langle\Psi^-|$, was calculated using the definition in Eq. (13) and found to be 0.945.

I could also calculate it from visibility V measurements [71]. In the horizontal-vertical basis I got $V_{H/V} = 0.921 \pm 0.008$, in the diagonal-antidiagonal basis $V_{D/A} = 0.971 \pm 0.006$, while in the left-right circular basis $V_{R/L} = 0.913 \pm 0.013$. Fidelity $F(\rho, \sigma)$, as defined by Eq.(48), was found to be:

$$F(\rho, \sigma) = \frac{1 + V_{H/V} + V_{D/A} + V_{R/L}}{4} = 0.951 \pm 0.004 \quad (48)$$

Neither the density matrix, nor the fidelity shows a perfect match with the desired $|\Psi^-\rangle$ state. According to the operation principle of SHWPs (described by Eq. (33)), I have identified their manufacturing errors as the major cause of deviation. Inaccuracies during the fabrication of the crystalline quartz lower half of the segmented half-wave plates result in thickness and orientation variations from the nominal values, which deteriorates the linear polarization of SPDC photons. To determine the source and magnitude of polarization errors, I performed additional supplementary measurements.

The polarization states were analyzed at the fiber outputs using a rotatable linear polarizer with an extinction ratio of 1:1000. During the measurements, only the lower or upper half of the SHWPs was allowed to transmit light, while the other half was covered. This approach enabled me to determine the power ratio between the major and minor axes (i.e., the extinction ratio) and the orientation angle of the polarization ellipse relative to the horizontal-vertical basis in each SHWP segment. The results are summarized in Table 10, where the values corresponding to the upper fused silica plates serve as a reference.

Segment	Extinction ratio	Orientation [deg]
SHWP1 _u	401 ± 71	0 ± 1
SHWP2 _u	410 ± 81	0 ± 1
SHWP1 _l	29.1 ± 0.71	12.5 ± 1
SHWP2 _l	511 ± 65	3 ± 1

Table 10. Experimentally obtained polarization states after each segment of the SHWPs. Power ratio between the major and minor axes (extinction ratio), and orientation angle of the polarization ellipse with respect to the horizontal-vertical basis were measured. SHWP1(2)_{u(l)} denote the upper (lower) part of the first (second) segmented wave-plate, respectively.

The data obtained for the lower apertures — where the crystalline quartz HWPs are located — revealed significant misorientation in the case of SHWP1, along with a notably low extinction ratio. This suggests that SHWP1 was not fabricated to the intended thickness. As a result, during coincidence measurements, the highly linear polarization emerging from the upper section of SHWP2 becomes correlated with a slightly elliptical and not perfectly orthogonal polarization from the lower section of SHWP1. Consequently, product states appear in the experimentally generated mixture,

degrading both the state fidelity and the density matrix. Replacing these demonstrative SHWPs with more precisely fabricated ones would obviously overcome this problem.

6.5 Summary and Thesis 2

I presented a method for the realization of polarization entanglement in a wavefront-splitting interferometric setup consisting of the minimum number of optical elements and without a need for active phase stabilization. The demonstrator device is compact, modular and offers convenient applicability by providing photon pairs coupled directly into single-mode fibers. The measurable entangled state purity is only a matter of fabrication accuracy of the used segmented half-wave plates. Its current characteristics make the equipment suitable for e.g. free-space telecommunication purposes [72] due to the 810 nm wavelength of generated photons, or clock synchronisation [60], just to mention a few possible applications. My new approach can also be adopted to any other non-collinear SPDC geometries, applying even different nonlinear crystals. For instance, the photon flux can be easily boosted by replacing the BBO with a periodically-poled potassium titanyl phosphate crystal that has greater down-conversion efficiency. The currently achieved heralding efficiency might be increased by dividing the SHWP-s into more segments, thereby symmetrizing the radiation incident on the fiber coupling optics to fill its aperture evenly, hence raising the fiber-coupling efficiency.

Thesis 2:

I proposed a method for converting the transverse momentum correlation of photon pairs into polarization entanglement by using wavefront-splitting interference and single-mode fibers, demonstrated the operation of the technique by incorporating it into the photon pair source presented in Thesis 1) and validated the method by determining state fidelity yielding $F = 0.95$. [H4]

7 Phase-tunable inverse Hong-Ou-Mandel interference for photon pair separation

Hong-Ou-Mandel (HOM) interference became famous for proving the indistinguishability of photons [73]. In the classic experiment, spatially separated indistinguishable photons are united. It is also known that the inverse process has the ability to divide degenerate photon pairs, because under the right circumstances quantum interference can occur in the wave function of a two-particle system, independently of the direction of propagation. Former publications have revealed how to utilize this quantum optical effect to separate frequency-degenerate photon pairs in a polarization-controlled fiber loop [74], or by using a Sagnac interferometer that includes a polarization beam splitter element [75]. In order to split the members, the same pair should enter the two different input ports of a beam splitter (BS) in coherent superposition, see Figure 31. The process only results in separated pairs when the wave functions of the two photon states are in phase relative to each other before the beam splitter, providing constructive interference after it. In consequence, phase tuning is a crucial adjustment that should be solved in such arrangements.

In this section, I present a solution that does not exploit any polarization-dependent device or effect, hence is applicable even for polarization-entangled frequency-degenerate photon pairs. The main idea of my method is a robust, simple and reliable way for phase tuning the HOM interference based on the wavelength dispersion of optical glass. An experimental demonstration is given together with measurement data taken by a customized photon pair source that uses type-0 spontaneous parametric down-conversion and a Sagnac interferometer.

7.1 Description of the concept

High-visibility inverse HOM interference can be observed by using an ideal (i.e. lossless) 50% division-ratio neutral beam splitter, as illustrated in Figure 31. The wave function $|\psi\rangle_{\text{in}}$ of the incoming two-particle system can be expressed as Eq. (49), where symbols “a” and “b” denote the input ports, and φ represents an arbitrary phase difference between the two photon states.

$$|\psi\rangle_{\text{in}} = \frac{|a, a\rangle + e^{i\varphi}|b, b\rangle}{\sqrt{2}} \quad (49)$$

The effect of a real, symmetric BS on the wave function of a single photon entering one of its “a” and “b” input ports is formulated as Eq. (50), where $|c\rangle$ and $|d\rangle$ refer to wave functions exiting either the “c” and “d” output ports. The complex τ and ρ are the transmission and reflection coefficients of the beam splitter, respectively. Their values depend on the splitting ratio of the beam splitter, which we will assume to be ideal in the following discussion with 50% splitting ratio.

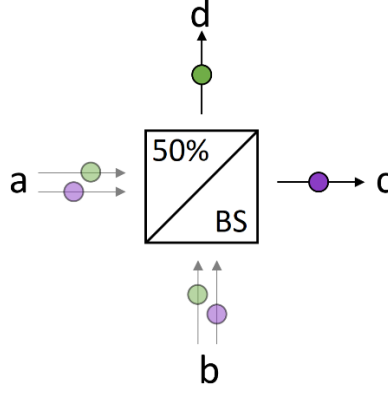


Figure 31. Schematic illustration of inverse HOM interference in case of a 50% neutral beam splitter prism (BS). Green and purple circles represent the members of a photon pair. Lighter colors indicate that both photons arrive in superimposed state with 50-50% probability at both “a” and “b” inputs. The twin photons exit the “c” and “d” outputs separated from each other.

$$\begin{aligned}
 |a\rangle &\rightarrow \tau|c\rangle + \rho|d\rangle \\
 |b\rangle &\rightarrow \rho|c\rangle + \tau|d\rangle
 \end{aligned} \tag{50}$$

For an ideal neutral BS of 50% transmittance and reflectance $\tau = 1/\sqrt{2}$ and $\rho = i/\sqrt{2}$ as follows from the continuity conditions of Maxwell's equations at boundaries. Passing the wave function of the above-described photon pair through the BS, the output state $|\Psi\rangle_{\text{out}}$ can be determined by substituting Eq. (50) to Eq. (49):

$$\begin{aligned}
 |\Psi\rangle_{\text{out}} &= \frac{i}{2\sqrt{2}}(|c, d\rangle + |d, c\rangle + e^{i\varphi}[|c, d\rangle + |d, c\rangle]) + \\
 &\quad \frac{1}{2\sqrt{2}}(|c, c\rangle - |d, d\rangle + e^{i\varphi}[|d, d\rangle - |c, c\rangle])
 \end{aligned} \tag{51}$$

From the equation it is clear that by varying φ it is possible to tune the coincidence probabilities on the outputs similarly to intensity in classical interference. If $\varphi = 0$, then the second term of $|\Psi\rangle_{\text{out}}$ vanishes, meaning that the particles in the pair become separated:

$$|\Psi\rangle_{\text{out}} = \frac{i}{\sqrt{2}}(|c, d\rangle + |d, c\rangle) \tag{52}$$

The $|\Psi\rangle_{\text{in}}$ wave function can be the result of e.g. the process of spontaneous parametric down conversion. By placing an appropriate non-linear crystal in a Sagnac loop, it gets pumped from both directions, see Figure 32, providing the required $|\Psi\rangle_{\text{in}}$ input to the BS. In case of an ideal (lossless) and perfectly symmetrical Sagnac loop, the above introduced phase is $\varphi = \pi/2$ (corresponding to the complex value of ρ , see above), which should be compensated for to get an integer multiple of 2π that produces the separated state expressed by Eq. (52).

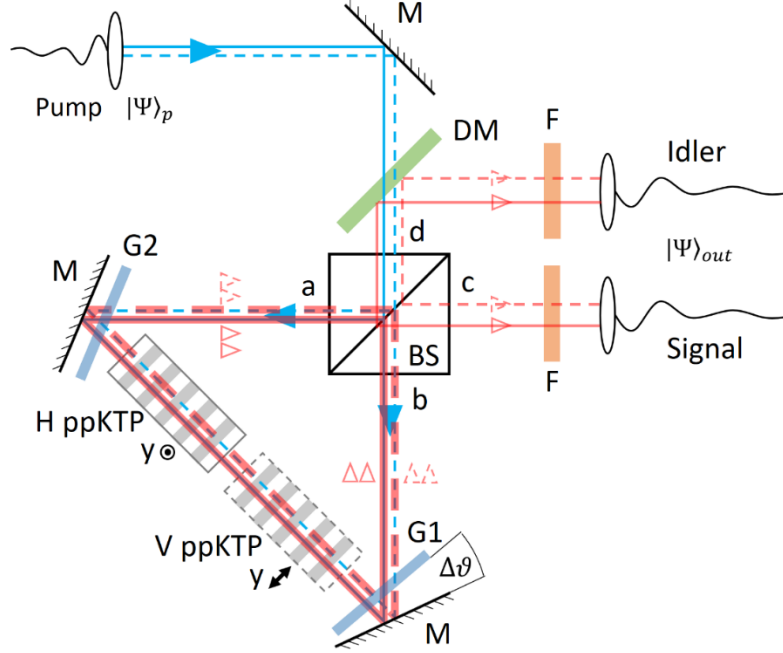


Figure 32. Layout of the experimental setup. Solid (dashed) blue line: H (V) polarized pump beam, solid (dashed) red line: H (V) polarized down-converted beam. Triangular arrows indicate the direction of propagation of the pump, signal and idler beams. The y -crystalline axis of the applied ppKTP crystal is given for reference. M: mirror, DM: dichroic mirror, BS: 50% neutral beam splitter, G1, G2: 2 mm thick N-BK7 glass plate, F: 810 ± 5 nm bandpass filter.

7.2 Phase tuning via dispersion

Since the Sagnac loop is a common-path interferometer, it is not straightforward how to adjust the phase difference φ between the two paths. In this interferometer, the $|a\rangle$ wave function of SPDC light propagates clockwise, while $|b\rangle$ in the opposite direction; consequently, any asymmetry introduced between these two paths will affect φ . In the SPDC process, the pumping and down-converted beams are phase-matched, and the phase acquired by each of them during its propagation in any non-dispersive media is equal. However, in a material that exhibits a wavelength-dependent refractive index, a difference arises. Accordingly, I introduced a glass plate at one point in the beam path of the loop as depicted in Figure 33. For the clockwise-propagating beam it is only the pump that passes through it affecting $|a\rangle$, while for the counterclockwise beam it is the down-converted light, which produces the required asymmetry by altering only $|b\rangle$. The glass plate thus causes a difference in the optical path lengths (see $\Lambda(\alpha)$ in Figure 33) for the pump and signal/idler waves, depending on the incident angle α of the beam. In Figure 32 this glass plate is designated by G1, and its orientation (hence the angle of incidence) is adjustable by tilting to fine-tune the phase difference between the pump and down-converted light, i.e. between the two propagation directions. In order to reduce the phase offset caused by this glass plate I also added a second one denoted by G2 in a symmetrical position to the Sagnac interferometer. Its orientation is fixed corresponding to the position of G1 when it is parallel to the mirror, thus the asymmetry in the loop now comes only from the angular difference $\Delta\theta$ of the two plates.

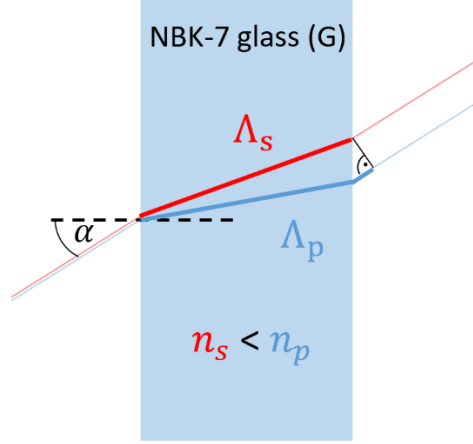


Figure 33. The optical path length difference (hence the acquired phase) between pump and down-converted beam is tunable by tilting a glass plate with respect to the incident beam.

Below I am going to determine the phase difference between the two propagation directions of the Sagnac interferometer as a function of the angle of incidence α . Considering a degenerate state, the wavelengths are related such that: $\lambda_s = \lambda_i = 2\lambda_p$. In this case, the refractive indices of the glass n_s , n_i and hence $\Lambda_s(\alpha)$, $\Lambda_i(\alpha)$ are equal for the signal and idler beams. Consequently, the phase difference between the pump and the down-converted beam passing through the plate is:

$$\Delta\xi(\alpha) = \frac{2\pi}{\lambda_p} (\Lambda_p(\alpha) - \Lambda_s(\alpha)) \quad (53)$$

Following geometrical considerations one can derive:

$$\Delta\xi(\alpha) = \frac{2\pi}{\lambda_p} d \left(\sqrt{n_p^2 - \sin^2(\alpha)} - \sqrt{n_s^2 - \sin^2(\alpha)} \right) \quad (54)$$

where d denotes the glass thickness. A similar calculation presented for a single wavelength in [76] sheds light to all the details.

The beams corresponding to $|a\rangle$ and $|b\rangle$ must occupy the same spatial mode after the BS to interfere properly. The problem is that by tilting a glass plate I do not only adjust the phase difference, but also introduce a parallel shift between the incident and transmitted beams, see Figure 33. Therefore, by simply putting a glass plate into the Sagnac loop thick enough to properly tune the HOM interference causes such a large parallel beam shift that would completely spoil the effect.

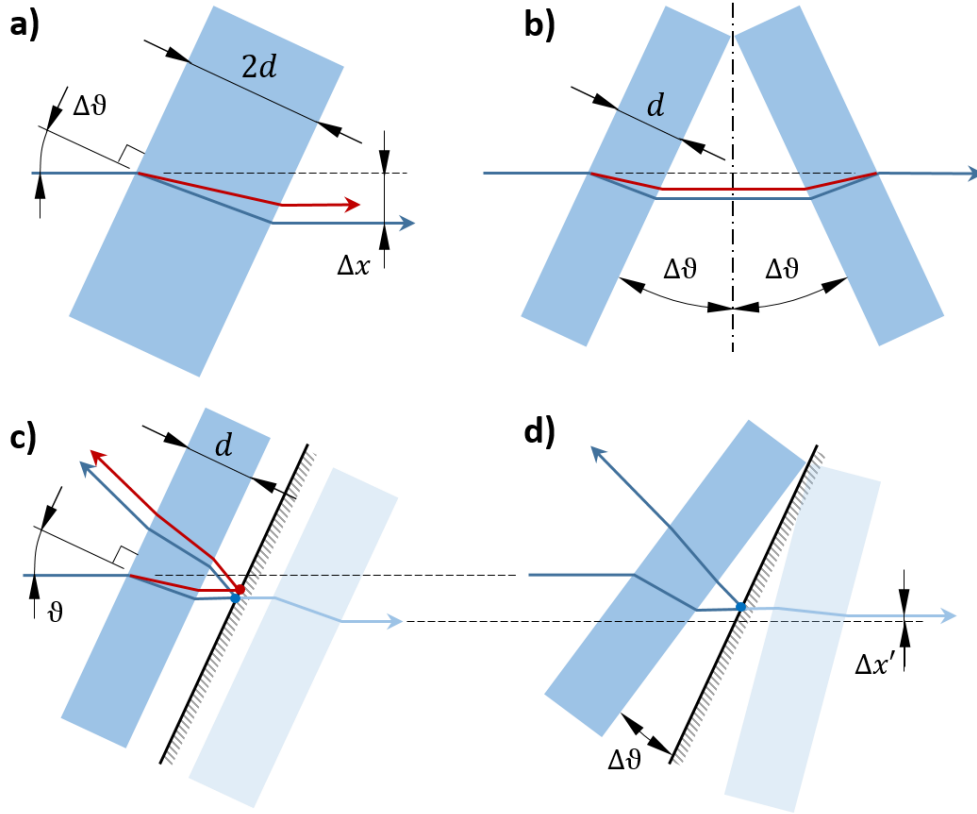


Figure 34. Variations for the implementation of phase tuning in a Sagnac loop by using tilted glass plates. Blue arrows represent the pump, and red arrows represent the down-converted beam. a) is the simplest solution but causes an unwanted parallel beam shift Δx . b) results $\Delta x = 0$ for any wavelength if the incident beam is perpendicular to the symmetry axis of the plates. It requires a special mount that tilts both plates maintaining their symmetry. c) uses a mirror to imitate the symmetrically placed plates. If the mirror has an offset tilt of ϑ , the beam shift Δx corresponding to $\Delta\vartheta$ cannot be zero, see subfigure d), however it is reduced by more than one order of magnitude relative to a).

Figure 34 shows some possibilities for the implementation of a tilted glass plate inside the Sagnac loop. Figure 34.a depicts the trivial solution with one plate inserted. The beam shift caused by a $2d$ -thick plate is denoted by Δx . This value can be reduced to zero independently of the wavelength by using two glass plates of thickness d , as shown in Figure 34.b, where the two plates of equivalent thickness are tilted symmetrically. Since the realization of a mounting gauge being capable of the symmetrical tilt is challenging, I propose a third solution, presented in Figure 34.c. In this method I can imitate the symmetrically tilted plates by inserting the glass in front of the folding mirrors of the interferometer so that each beam passes it two times. This solution does cause zero beam shift indeed, but only when the mirrors are perpendicular to the incident beam, while the incident angle that is optimal for a Sagnac loop is $\vartheta = 22.5^\circ$. Fortunately, the second glass plate indicated by G2 in Figure 32 also corrects for this beam shift, thus it is only the effect of the $\Delta\vartheta$ tilt used for phase tuning that should be taken into account. The difference relative to case a) is illustrated in Figure 34.d. Calculations detailed in Subsection 10.2 of the Appendix revealed that $\Delta x'$ is one order of magnitude less than Δx , which affects the Sagnac interference only to a negligible extent.

In case of my solution presented in Figure 34.c the angle of incidence used in Eq. (54) for the tiltable mirror G1 is $\alpha = \vartheta + \Delta\vartheta$ whereas for the fixed plate G2 it is: $\alpha = \vartheta$. Using these relations in a more general description in the following section, in Eq. (70) I can show that the phase difference φ of the inverse HOM interference can be expressed in terms of $\Delta\xi(\alpha)$ as follows:

$$\varphi = \frac{\pi}{2} - \Delta\xi(\vartheta + \Delta\vartheta) - \Delta\xi(\vartheta - \Delta\vartheta) + 2\Delta\xi(\vartheta) \quad (55)$$

From this equation one can calculate how much they need to tilt a given glass plate to achieve the prescribed phase modulation. I applied a Schott NBK-7 glass plate of $d = 2$ mm thickness with $n_p = 1.5302$, $n_{s(i)} = 1.5106$ refractive indices, for which the tilt range of $\Delta\vartheta \in [0^\circ, 9^\circ]$ provides a phase modulation between 0 and 2π .

7.3 Adjustment process and experimental results

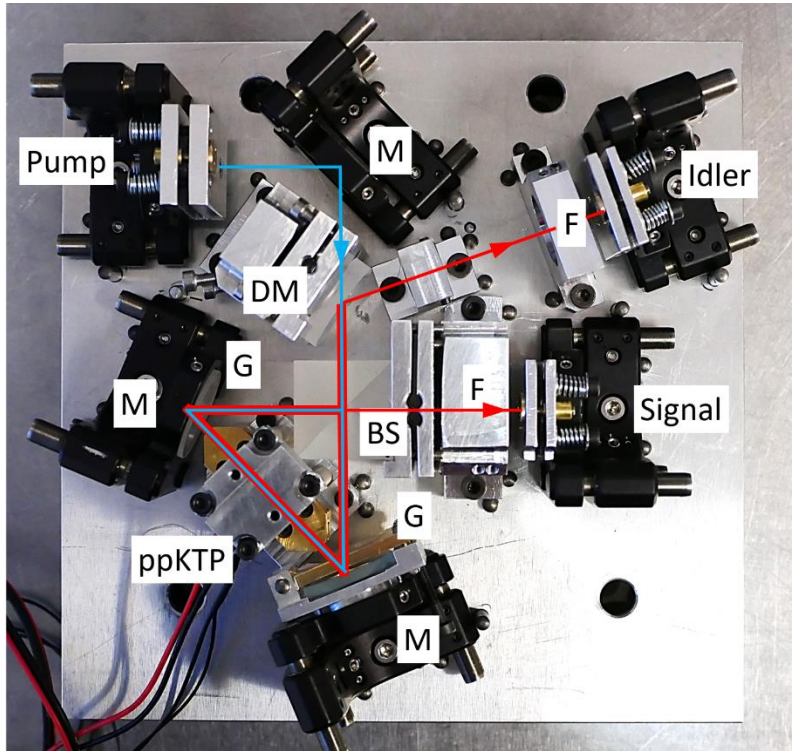


Figure 35. Realized experimental setup of the schematics from Figure 32.

To perform any measurements with the setup the realization of which is depicted in Figure 35, first, I had to align the Sagnac interferometer itself, following a method similar to that described in Subsection 5.4. The ppKTP crystals are located in a temperature stabilized mount, the temperature of which was maintained with $\pm 0.05^\circ\text{C}$ precision by a peltier thermo-electric controller. Ideally, all beams should be focused at the center of the two-crystal arrangement. To achieve this, I designed a custom mechanical component that precisely places small apertures with a diameter of $250 \mu\text{m}$ (matching the pump beam size at that position) on either side of the crystals in symmetric positions. I then adjusted the pump beam and one of the interferometer mirrors (mirror M in Figure 32) until I observed maximum pump throughput in the

clockwise direction. The transmitted intensity through the apertures was measured using a power meter.

To reach the absolute maximum, I also fine-tuned the pump outcoupler lens to shift the beam waist precisely to the center of the crystal arrangement, which ensures maximum throughput through the symmetric apertures. I then repeated the alignment process in the counter-clockwise direction by adjusting the beamsplitter (BS) and the other interferometer mirror.

Next, I examined the pump beam reflected along the idler path (without the F filter and the idler coupling optics) and projected the free space propagating beam onto a camera (AVT Manta MG-201B). The camera image revealed the spatial overlap of the clockwise and counter-clockwise propagating pump beams. When properly aligned, only a small angular difference remains between them, resulting in interference fringes visible on the camera. By fine-tuning the interferometer mirrors, I was able to eliminate these fringes, thereby achieving interferometric alignment of the Sagnac loop for the pump beam.

To ensure that both the signal and idler coupling optics are also aligned with the pump beam path, I launched 809 nm laser light (Coherent Surelock LM-808-PLR-120-3) backward through the fibers connected to the signal and idler outputs. Using the same method with the apertures in place, I adjusted the kinematic mounts of the signal and idler paths until maximum throughput was again observed through the apertures. This ensures that the down-converted signal and idler photons are immediately coupled into the fibers, providing a feedback signal that helps further optimize and fine-tune their alignment.

I could analyze inverse HOM interference through investigating the coincidence probability \mathbb{P}_c of the photon source as a function of φ , which can be controlled by tilting one of the glass plates (G1). First the $|\psi\rangle_{\text{out}}$ state should be projected to its coincidence subspace by applying the \widehat{M} projector:

$$\widehat{M} = |c, d\rangle\langle c, d| + |d, c\rangle\langle d, c|, \quad (56)$$

then the output wave function describing only coincidence events can be written as:

$$|\psi\rangle_{\text{out},c} = \widehat{M}|\psi\rangle_{\text{out}} \quad (57)$$

\mathbb{P}_c can be expressed by $|\psi\rangle_{\text{out},c}$ and the total (propagation and detection) loss L in the system as:

$$\mathbb{P}_c = L \|\psi\rangle_{\text{out},c}\|^2 = \frac{L}{2} (\cos \varphi + 1), \quad (58)$$

where I substituted Eq. (51) into $|\psi\rangle_{\text{out}}$. I implemented the phase tuning by using a lever mechanism and a micrometer screw, rotating it in a controlled manner to change the tilt angle of the G1 plate. In a real experiment one can never exactly know how much phase shift they introduce due to systematic errors occurring in the process. These are caused by various effects, such as the inaccurate value of the refractive index or the thickness of the glass plates, the pitch error of the actuator screw, lever length,

and so on. All of these result in an approximately linear scaling of φ in the argument of Eq. (58). Therefore, it is straightforward to introduce a fitting function for \mathbb{P}_c , that can properly account for all experimental imperfections by separating the amplitude of the modulated part A from that of the losses L , and inserting a phase stretching factor γ .

$$\mathbb{P}_c = A \cos(\gamma(\varphi - \varphi_0)) + \frac{L}{2} \quad (59)$$

Since the total loss L is unnecessary to quantify the success of modulating the HOM interference, I normalized Eq. (59) with L to obtain the final form:

$$\mathbb{P}_c = \frac{L}{2} \left(\frac{2A}{L} \cos(\gamma(\varphi - \varphi_0)) + 1 \right) \quad (60)$$

I tested the experimental setup by setting the pump polarization so to excite only one ppKTP crystal at a time; the results can be seen in Figure 36, the best-fit parameters are summarized in Table 11. The measurement agrees well with the predicted cosine shape: the root-mean-square error for the difference between the measured points and the fitting curve is $6.82 \cdot 10^{-4}$, while the γ coefficient is only 7.5% less than unity, i.e. the ideal value.

	H	V
$2A/L$	0.820 ± 0.0102	0.720 ± 0.0072
γ	0.925 ± 0.0079	0.955 ± 0.0045
φ_0	4.95 ± 0.057	3.16 ± 0.028

Table 11. Fitted parameters of inverse HOM interference.

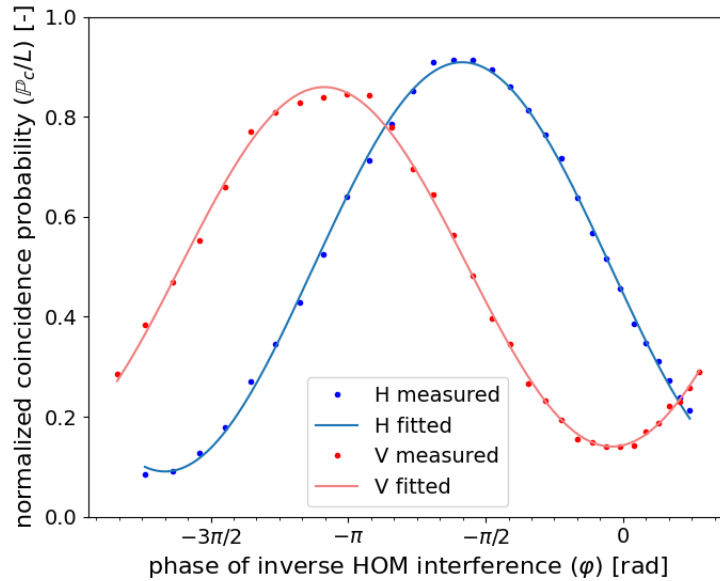


Figure 36. Normalized coincidence probability of the photon pair source as a function of the φ phase of the inverse HOM interference tuned by tilting the G1 glass plate. The normalizing factor is L , the total loss of the system. Non-linear regression was made by using Eq. (60), best-fit parameters are listed in Table 11.

Visibility of the curves ($2A/L$) does not reach unity for either excitation, which can be explained by two effects. On the one hand, the pump laser has a finite coherence length, in our case about $33750 \times 2\pi$ expressed in radians. When using only H- or V-excitation, the “unused” crystal introduces a $3400 \times 2\pi$ phase difference between the two oppositely propagating photon states (see details in Section 8.1), which is not negligible relative to the coherence length, causing the visibility of inverse HOM interference to drop. On the other hand, in my calculations I assumed a perfect beam splitter, whose real-life imperfections (losses, non-uniform splitting ratio) also decrease the visibility.

7.4 Summary and Thesis 3

My work has successfully demonstrated the phase tunability of inverse HOM interference utilizing the wavelength dispersion of isotropic optical glass. The phenomenon was demonstrated in a Sagnac interferometer-based SPDC photon pair source, and was shown to be a useful tool for separating frequency-degenerate photon pairs, when the down-converted photons and the pump co-propagate.

Thesis 3:

For the phase tuning of inverse Hong-Ou-Mandel interference in a Sagnac loop I proposed a simple and reliable method based on the wavelength dispersion of optical glass, described its theoretical background and experimentally demonstrated the effect in a custom-built photon pair source by using it for the separation of frequency-degenerate correlated photon pairs. [H5]

8 Polarization entanglement utilizing inverse HOM interference

Many applications in quantum optics require the generation of entangled photon pairs [1][2][44][45]. Once created, practical usability demands that their members (called signal and idler photons) can be spatially separated from each other. For this task, several schemes are known utilizing polarization elements, dichroic filters [10][63], Dense Wavelength Division Multiplexer [42][46] or spatial filters [H2]. There are situations when the signal and idler photons have to be of identical energy: this so-called frequency degeneracy is crucial, for example, in quantum teleportation [4] and quantum repeaters [5]. In these applications polarization entanglement is often involved, too. Isolating polarization-entangled signal and idler photons while maintaining their common spectral distribution is challenging to this day. The trivial solution is to use a neutral beam splitter, but it comes at a price of 50% separation efficiency. Better performance can be achieved by more elaborate methods, e.g. the one using a polarization beam splitter in a Sagnac interferometer and spontaneous parametric down-conversion (SPDC) of type-II phase matching [36], or utilizing wavefront-splitting interference combined with non-collinear type-I phase matching [H4]. My aim is to present an alternative solution for photon separation utilizing the inverse HOM effect introduced in Section 7, that may work even in other types of SPDC sources. Being a direct continuation of the preceding section, the below derivations will use the notation terminology presented there without any alteration.

8.1 Working principles

In order for the inverse HOM to work, the generated twin photons should also have the same polarization. This means that one has to choose a non-linear crystal of either type-0 or type-I phase matching, which is not effective if polarization entanglement is a requirement.

However, by placing two such crystals in the Sagnac loop oriented orthogonally relative to each other, the creation and separation of polarization-entangled frequency degenerate photon pairs become possible. In my optical system I use periodically-poled potassium titanyl phosphate (ppKTP) crystals that have biaxial optical anisotropy, hence their three crystalline axes should be distinguished. Let the beams propagate along the x-axis of the crystal, and y/z denote the two other mutually orthogonal axes: Figure 32 shows the orientation of the two crystals by indicating their y-axis.

So that I could incorporate the polarization state in the wave function, I introduce a notation in the equations to indicate the horizontal (H) or vertical (V) linear polarization of each photon. From the above paragraph it follows that to have photons in both polarization states simultaneously in one propagation direction of the interferometer, each crystal has to be pumped at the same time. The $|H\rangle$ component of the pump undergoes down-conversion in the H-oriented ppKTP, whereas the $|V\rangle$ component does the same in the V-orientation ppKTP. For this reason, the polarization of the pump beam before the beam splitter must be set properly. Another consequence

of the two-crystal arrangement is an intrinsic asymmetry in the system, the effects of which are discussed in the next paragraphs.

For the sake of completeness, I discuss the evolution of the wave function in the whole system starting from the pump. The Sagnac loop is pumped from the “d” port of the beam splitter, the corresponding wave function $|\psi\rangle_p$ is formulated as

$$|\psi\rangle_p = \frac{|dH\rangle + qe^{i\phi}|dV\rangle}{\sqrt{1+q^2}}, \quad (61)$$

where q is the pump polarization amplitude ratio and ϕ is the phase difference between the $|H\rangle$ and $|V\rangle$ polarization states. The beam splitter transforms the field entering this port as

$$|d\rangle \rightarrow \rho|a\rangle + \tau|b\rangle. \quad (62)$$

Given an ideal 50% BS, the split pump propagating in the loop is:

$$|\psi\rangle_p = \frac{i|aH\rangle + |bH\rangle + iqe^{i\phi}|aV\rangle + qe^{i\phi}|bV\rangle}{\sqrt{2+2q^2}}, \quad (63)$$

According to phase matching, the connection between wave vectors is $k_p = k_s + k_i$. As a consequence, the phase difference between the pump and SPDC lights is zero in a non-dispersive medium, which is valid to a very good approximation for the air-filled regions of the Sagnac loop. This is true for both the $|H\rangle$ polarization in the H-orientation ppKTP, and the $|V\rangle$ in the V-orientation ppKTP. However, all beams acquire some phase difference propagating in the other crystal. E.g., when a H-pump passes through the V-ppKTP it acquires $2\pi n_{y,p}l/\lambda_p$ phase, where λ_p is the pump wavelength, $n_{y,p}$ is the refractive index of the crystal for the polarization parallel to the y-crystallographic axis at the pump wavelength, and l is the length of the crystals. Such a phase shift can be determined similarly for every beams.

After a full orbit in the loop and down-conversion in the crystals, the $|a\rangle$ and $|b\rangle$ ports get interchanged (i.e. $|aH\rangle \rightarrow |bH, bH\rangle$), and the $|\psi\rangle_{in}$ wave function of the inverse HOM interference can be written as:

$$|\psi\rangle_{in} = \frac{1}{\sqrt{2+2q^2}} (e^{i\delta_1}|bH, bH\rangle + e^{i\delta_2}|aH, aH\rangle + qe^{i\delta_3}|bV, bV\rangle + qe^{i\delta_4}|aV, aV\rangle), \quad (64)$$

where

$$\begin{aligned} \delta_1 = & \frac{\pi}{2} + \frac{2\pi}{\lambda_p} 2\Lambda_p(\vartheta) + \frac{2\pi}{\lambda_s} n_{y,s}l + \frac{2\pi}{\lambda_i} n_{y,i}l + \frac{2\pi}{\lambda_s} (\Lambda_s(\vartheta - \Delta\vartheta) + \Lambda_s(\vartheta + \Delta\vartheta)) + \\ & \frac{2\pi}{\lambda_i} (\Lambda_i(\vartheta - \Delta\vartheta) + \Lambda_i(\vartheta + \Delta\vartheta)). \end{aligned} \quad (65)$$

The terms in δ_1 can be easily resolved by following the beam path in Figure 32:

- Pump reflecting on BS: $\pi/2$
- Pump passing through G2 glass plate: $(2\pi/\lambda_p) \cdot 2\Lambda_p(\vartheta)$

- Down-conversion in H ppKTP
- Signal and idler passing through V ppKTP: $(2\pi/\lambda_s)n_{y,s}l + (2\pi/\lambda_i)n_{y,i}l$
- Signal and idler passing through G1 glass plate:
 $(2\pi/\lambda_s) \cdot (\Lambda_s(\vartheta - \Delta\vartheta) + \Lambda_s(\vartheta + \Delta\vartheta)) + (2\pi/\lambda_i) \cdot (\Lambda_i(\vartheta - \Delta\vartheta) + \Lambda_i(\vartheta + \Delta\vartheta))$

Similarly, one can work out the other phase coefficients in Eq. (64):

$$\delta_2 = \frac{2\pi}{\lambda_p} (\Lambda_p(\vartheta + \Delta\vartheta) + \Lambda_p(\vartheta - \Delta\vartheta)) + \frac{2\pi}{\lambda_p} n_{y,p}l + \frac{2\pi}{\lambda_s} 2\Lambda_s(\vartheta) + \frac{2\pi}{\lambda_i} 2\Lambda_i(\vartheta) \quad (66)$$

$$\delta_3 = \frac{\pi}{2} + \phi + \frac{2\pi}{\lambda_p} 2\Lambda_p(\vartheta) + \frac{2\pi}{\lambda_p} n_{y,p}l + \frac{2\pi}{\lambda_s} (\Lambda_s(\vartheta - \Delta\vartheta) + \Lambda_s(\vartheta + \Delta\vartheta)) + \frac{2\pi}{\lambda_i} (\Lambda_i(\vartheta - \Delta\vartheta) + \Lambda_i(\vartheta + \Delta\vartheta)). \quad (67)$$

$$\delta_4 = \phi + \frac{2\pi}{\lambda_p} (\Lambda_p(\vartheta + \Delta\vartheta) + \Lambda_p(\vartheta - \Delta\vartheta)) + \frac{2\pi}{\lambda_s} n_{y,s}l + \frac{2\pi}{\lambda_i} n_{y,i}l + \frac{2\pi}{\lambda_s} 2\Lambda_s(\vartheta) + \frac{2\pi}{\lambda_i} 2\Lambda_i(\vartheta). \quad (68)$$

In order to comply with the form of Eq. (49) I multiply out $e^{i\delta_2}$ from Eq. (64). The phase differences like $\delta_2 - \delta_1$ in $|\Psi\rangle_{\text{in}}$ arise from the asymmetry of the clockwise and counterclockwise paths, and originate from two distinct sources:

- Phase shift φ caused by the asymmetric placement of the G1, G2 glass plates.
- Phase shift κ induced by the wavelength dispersion of the crystals.

The value of the latter can be determined in the degenerate case when $\lambda_s = \lambda_i = 2\lambda_p$, therefore $n_{y,s} = n_{y,i}$ as follows:

$$\kappa = \frac{2\pi}{\lambda_p} l (n_{y,s} - n_{y,p}) \quad (69)$$

Using the expression of $\Delta\xi(\alpha)$ from Eq. (53) and κ I can formulate the phase differences in $|\Psi\rangle_{\text{in}}$ as:

$$\delta_1 - \delta_2 = \frac{\pi}{2} - \Delta\xi(\vartheta + \Delta\vartheta) - \Delta\xi(\vartheta - \Delta\vartheta) + 2\Delta\xi(\vartheta) + \kappa = \varphi + \kappa \quad (70)$$

From which follows the aforementioned expression of φ in Eq. (55).

Similarly, $\delta_4 - \delta_2 = \phi + \kappa$ and $\delta_3 - \delta_2 = \phi + \varphi$. Omitting the global phase $e^{i\delta_2}$, this formalism results in the input state:

$$|\Psi\rangle_{\text{in}} = \frac{1}{\sqrt{2 + 2q^2}} (|aH, aH\rangle + e^{i(\varphi+\kappa)} |bH, bH\rangle + qe^{i(\varphi+\kappa)} |aV, aV\rangle + qe^{i(\phi+\varphi)} |bV, bV\rangle) \quad (71)$$

After passing through the BS again, and applying Eq. (50), the output wave function can be written as follows:

$$\begin{aligned}
|\Psi\rangle_{\text{out}} = & \frac{1}{\sqrt{8+8q^2}} [(|cH, cH\rangle + i|cH, dH\rangle + i|dH, cH\rangle - |dH, dH\rangle) + \\
& e^{i(\varphi+\kappa)}(-|cH, cH\rangle + i|cH, dH\rangle + i|dH, cH\rangle + |dH, dH\rangle) + \\
& e^{i(\varphi+\phi)}(-|cV, cV\rangle + i|cV, dV\rangle + i|dV, cV\rangle + |dV, dV\rangle) + \\
& e^{i(\phi+\kappa)}(|cV, cV\rangle + i|cV, dV\rangle + i|dV, cV\rangle - |dV, dV\rangle)]. \tag{72}
\end{aligned}$$

This expression implies that H- and V-polarized photon pairs cannot be perfectly separated simultaneously using the present crystal arrangement: if $\varphi = -\kappa$, then H-polarization separates, when $\varphi = \kappa$, then it is V. Hereupon I examine only those photon pairs that became separated. Therefore, I apply the projection to the coincidence subspace according to Eq. (56). If we do not distinguish between the $|c, d\rangle$ and $|d, c\rangle$ separated pairs, then the state after this projection can be written as:

$$|\Psi\rangle_{\text{out},c} = \widehat{M}|\Psi\rangle_{\text{out}} = ie^{i(\frac{\varphi+\kappa}{2})} \frac{\cos\left(\frac{\varphi+\kappa}{2}\right)|H, H\rangle + qe^{i\phi}\cos\left(\frac{\varphi-\kappa}{2}\right)|V, V\rangle}{\sqrt{1+q^2}}. \tag{73}$$

According to this, by setting the phase shift in the Sagnac loop to $\varphi := -\kappa$ and the amplitude ratio of the two polarization states of the pump to $q := 1/|\cos\kappa|$, a perfectly correlated Bell state can be attained, though due to the above-described problem there will always be a certain ratio of V-state photons that do not become separated. The phase difference ϕ can be varied by a polarization compensator placed either directly into the pump beam or after the output of the photon source.

8.2 Experimental demonstration

The complete setup I used for the demonstration is depicted in Figure 32. The pump is implemented by coupling an Omicron (LDM405.120.CWA.L.WS) laser of $\lambda_p = 405$ nm wavelength and $33750 \times \lambda_p$ coherence length into a single-mode fiber to exert spatial filtering. The polarization parameters of the pump (q, ϕ) are controlled by fiber-loop-type phase retarders (see Subsection 4.6.3). After outcoupling from the fiber the pump is directed towards the Sagnac loop by a mirror. The interferometer consists of a 50% neutral beam splitter (BS), two mirrors (M) with the above-mentioned glass plates (G1, G2) in front of them, and two type-0 collinearly phase-matched ppKTP crystals of 20 mm length. In case of this crystal $\kappa \approx 3400 \times 2\pi$, according to Eq. (69). Down-converted light is separated from the pump by a dichroic mirror (DM) and bandpass filters (F) of 10 nm bandwidth centered at $\lambda_s = \lambda_i = 810$ nm. Finally, both signal and idler beams are coupled into single-mode fibers.

The analysis for the \mathbb{P}_c coincidence probability in Section 7.3 is still valid here with some amendment. Now \mathbb{P}_c is expressed by:

$$\mathbb{P}_c = L \|\Psi\rangle_{\text{out},c}\|^2 = L \frac{\cos(\varphi + \kappa) + q^2 \cos(\varphi - \kappa)}{2 + 2q^2} + \frac{L}{2} \tag{74}$$

It is easy to derive that \mathbb{P}_c can always be expressed as a single cosine function, with amplitude A and φ_0 phase constants. Hence, the fitting function of Eq. (60) can also

be applied here with its parameters given by the following formulae (see Subsection 10.3 of Appendix):

$$A = \frac{L}{2 + 2q^2} \sqrt{1 + q^4 + 2q^2 \cos(2\kappa)} \quad (75)$$

$$\varphi_0 = \text{atan} \left(\tan(\kappa) \frac{q^2 - 1}{q^2 + 1} \right). \quad (76)$$

I could determine the value of κ from the measurement. Mathematically, the H-excitation can be expressed by $q = 0$, see Eq. (61), which gives $\varphi_0 = -\kappa$ according to Eq. (76). Similarly, for the V-excitation $q \rightarrow \infty$, and $\varphi_0 = +\kappa$. The phase difference between the two cases thus equals exactly 2κ , and its modulo is clearly visible in the curves in Figure 36. According to the fitted-phase offset values in Table 11, my measurement provides:

$$c_H \varphi_{0,H} - c_V \varphi_{0,V} = 2\kappa \text{ mod } 2\pi = 1.56 \text{ [rad]} \quad (77)$$

I also wanted to examine the properties of polarization entanglement. In order to do it, I adjusted the setup so that it produced the $|\Phi^-\rangle$ Bell state. The process I performed was the following:

- 1) To begin with, the photon source was pumped with only $|H\rangle$ polarization and the tilt of G1 was tuned until maximum coincidence count rate in the $|H, H\rangle$ basis was achieved. This setting satisfies the criterion of $\varphi = -\kappa$.
- 2) The direction of polarization of the pump field was rotated until the coincidence count rates in the $|H, H\rangle$ and $|V, V\rangle$ bases became equalized, which complies with $q = 1/|\cos \kappa|$.
- 3) Finally, I altered ϕ with a Berek compensator in the signal beam until coincidence count rate in the $|D, D\rangle$ (i.e. diagonal-diagonal) basis was minimized, corresponding to $\phi = \pi$, hence attaining the required $|\Phi^-\rangle$ state.

To verify the effectiveness of the above adjustment procedure, I conducted full polarization state tomography [24] on the photon pair source. A graphic representation of the resulting density matrix ρ is depicted in Figure 37.

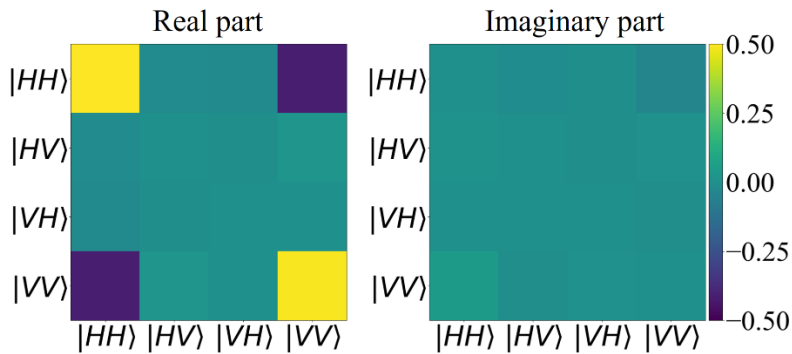


Figure 37. Reconstructed density matrix ρ of the separated photon pairs.

The $|\Phi^-\rangle$ state is characterized by a theoretical density matrix of $\sigma = |\Phi^-\rangle\langle\Phi^-|$. State fidelity towards σ was calculated according to the definition given by Eq. (13), optical properties measured during entangled-state preparation are listed in Table 12.

Brightness	533 ± 22.5 pairs/s/mW/nm
Heralding efficiency	$7.0 \pm 0.16\%$
Output bandwidth	10 nm
State fidelity	91.4%

Table 12. Optical properties of the photon pair source adjusted to produce the $|\Phi^-\rangle$ entangled state. All values are corrected for detector efficiency, the errors indicated correspond to $1\times$ standard deviation.

The obtained fidelity value is sufficiently high to clearly justify the claim that I have reached the required polarization entanglement. Its difference from unity is best explained by the imperfections of the beam splitter applied, since any deviation from the ideal 50% ratio causes amplitude and phase changes, both affecting the outcome of inverse HOM interference. My BS was a stock product having polarization- and wavelength-dependent transmission, reflection, absorption and non-uniform splitting ratio, neither of which were included in the analytical discussion of my study to keep it simple and straightforward. It is also apparent that the brightness and heralding efficiency (aka. heralding ratio) of the photon source are low, given that I used ppKTP crystals. The reason for this is that I built our arrangement to convincingly demonstrate the phase-tunable inverse HOM interference, and not strove for the effective coupling of down-converted light into the single-mode fibers. However, this is only a technical problem that can be solved by further optimizing the setup.

8.3 Potential possibilities for improvement

It is even possible to completely overcome the photon pair-separation problem imposed by the phase shift κ . By replacing the two crystals with three, according to Figure 38, and following a similar analysis as above, one can prove that due to the symmetrical placement of the crystals, the disturbing phase factor κ vanishes.

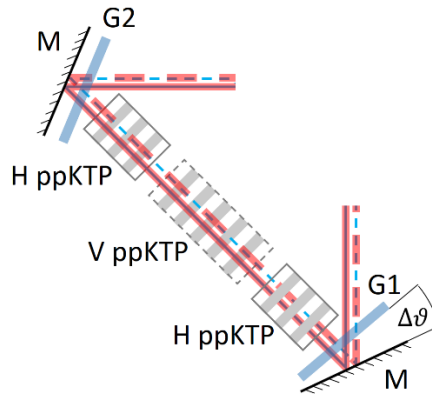


Figure 38. Ideal, symmetrical placement of nonlinear crystals in a Sagnac loop resulting $K = 0$. (Modified detail of the whole setup presented in Figure 32.)

8.4 Summary and Thesis 4

I proposed an adjustment scheme by which polarization-entangled photon pairs could be generated and separated. The experiments were carried out with stock optical elements not having been optimized for the task, resulting in only 91.4% state fidelity. Another consequence of my specific implementation is that the temporal delay corresponding to the phase shift (κ) caused by the asymmetric arrangement of the applied crystals is comparable to the coherence time of the pump laser, decreasing the visibility of the interference. In Section 8.3 I also gave a solution to this problem by a special symmetric crystal placement. In spite of the moderate optical properties of my experimental setup I hope that by demonstrating an advanced application of inverse HOM interference my work may contribute to the field of photon pair sources.

Thesis 4:

I described an approach to implement polarization entanglement with two, consecutively placed type-0 collinearly phase-matched nonlinear crystals in a Sagnac interferometer without the need of (dual-wavelength) polarization optics utilizing the inverse Hong-Ou-Mandel effect, and experimentally demonstrated its operation by tuning the source of Thesis 3) to produce a Bell state with $F = 0.914$ fidelity. [H5]

9 Conclusions

During the course of my doctoral work, I focused on the experimental realization and engineering of correlated photon pair sources based on spontaneous parametric down-conversion (SPDC). Beginning with fundamental studies, I explored various nonlinear crystals, phase-matching configurations, and experimental geometries, gradually progressing toward the development of compact and functional photon sources. My overarching goal was the generation of polarization-entangled photon pairs using modular and practical systems suitable for both laboratory and applied contexts.

Over the span of the project, I designed and constructed three distinct SPDC-based photon sources. The design process encompassed both theoretical modeling and hands-on engineering, including optical layout planning, mechanical component design, and precise assembly. Two of these sources were developed with special attention to engineering challenges, such as environmental robustness, fiber compatibility, and compactness — qualities necessary for out-of-laboratory deployment. All my sources utilize single-mode fiber coupling to facilitate straightforward interfacing with existing quantum optical systems.

One of these devices — presented in Section 6 — is currently operating in an experimental quantum key distribution setup at the Department of Networked Systems and Services, Faculty of Electrical Engineering and Informatics, Budapest University of Technology and Economics (BME). This confirms not only the practical usability but also the application-readiness of the developed photon source, thereby achieving technology readiness level 5 (TRL 5).

Beyond source engineering, I proposed and experimentally demonstrated two distinct methods for generating polarization entanglement. The first converts transverse momentum correlation into polarization entanglement using wavefront-splitting interferometry. This method requires minimal optical components and no active phase stabilization, offering a simple yet effective configuration for entangled photon generation. The second approach, more unconventional, applies the inverse Hong-Ou-Mandel effect within a Sagnac interferometer using two consecutively placed, type-0 nonlinear crystals — completely avoiding the use of polarization optics. While the latter was constrained by the limitations of available components, the concept was successfully demonstrated, and a feasible path toward improved fidelity was proposed.

Furthermore, I introduced a technique for separating frequency-degenerate polarization-entangled photon pairs using the dispersion properties of optical glass to control the phase of inverse HOM interference. This method was integrated into a custom-built source and expands the functionality of HOM-based devices by enabling fine control over photon pair separation.

Taken together, my research addresses both foundational and applied aspects of photon pair source design. By introducing new entanglement-generation strategies and improving system compactness, fiber compatibility, and robustness, I hope to contribute to the broader field of quantum optics. My results provide building blocks for future technologies in quantum communication and computation, and I trust they

will serve as a stepping-stone for continued development of versatile and high-performance quantum photonic systems.

Acknowledgement

I would like to thank my family and friends for the support they provided throughout the preparation of this work.

I am also grateful to my colleagues, and especially to my supervisor at the BME Faculty of Natural Sciences, Department of Atomic Physics, for their guidance, advice, and collaboration throughout the research.

I am thankful to the staff of the mechanical and optical workshops of the Department, who fabricated all the custom components used in my experiments.

Parts of my research were supported by the:

- National Research, Development, and Innovation Fund of Hungary within the Quantum Technology National Excellence Program as part of project 2017-1.2.1-NKP-2017-00001
- TKP2021 grant of NKFIH Hungary as a part of Project No. BME-NVA-02,
- Quantum Informatics National Laboratory project, NKFIH-873-4/2020.
- Ministry of Culture and Innovation and the National Research, Development and Innovation Office within the Quantum Information National Laboratory of Hungary (Grant No. 2022-2.1.1-NL-2022-00004)

References

Own publications connected to the theses:

- [H1] **Cs. T. Holló**, G. Erdei, and T. Sarkadi (2020, September). Increasing the correlation level of polarization entangled photon pairs generated by type-II SPDC in BBO, in *Laser Science* (Optica Publishing Group, Washington, DC, 2020), pp. JTh4A-36.
- [H2] **Cs. T. Holló**, T. Sarkadi, M. Galambos, D. Bíró, A. Barócsi, P. Koppa, and G. Erdei, Compact, single-mode fiber-coupled, correlated photon pair source based on type-I beta-barium borate crystal, *Opt. Eng.* 61, 025101 (2022).
- [H3] **Cs. T. Holló**, T. Sarkadi, M. Galambos, B. Bodrog, A. Barócsi, P. Koppa, and G. Erdei, Compact, portable, fiber-coupled correlated photon pair source with enhanced performance, in *Quantum 2.0 Conference and Exhibition* (Optica Publishing Group, Washington, DC, 2022), p. QTu2A.18.
- [H4] **Cs. T. Holló**, T. Sarkadi, M. Galambos, A. Barócsi, P. Koppa, V. Hanyecz, and G. Erdei, Conversion of transverse momentum correlation of photon pairs into polarization entanglement by using wavefront-splitting interference, *Physical Review A* 106, 063710 (2022).
- [H5] **Cs. T. Holló**, T. Sarkadi, A. Barócsi, P. Koppa, and G. Erdei, Phase-tunable inverse Hong-Ou-Mandel interference: principles and demonstration in a photon pair source, *Physical Review A* 111.1, 013531 (2025)

Other own publications:

- [H6] **Cs. T. Holló**, K. Miháلتz, M. Kurucz, A. Csorba, K. Kránitz, I. Kovács, Z. Zs. Nagy, G. Erdei, Objective quantification and spatial mapping of cataract with a Shack-Hartmann wavefront sensor, *Scientific Reports* 10 (1), 1-10, 2020.

External references:

- [1] A. K. Ekert, Quantum cryptography based on Bell's theorem, *Phys. Rev. Lett.* 67, 661 (1991)
- [2] J. Pseiner, L. Achatz, L. Bulla, M. Bohmann, and R. Ursin, Experimental wavelength-multiplexed entanglement based quantum cryptography, *Quantum Sci. Technol.* 6, 035013 (2021)
- [3] J. L. O'brien, "Optical quantum computing," *Science* 318(5856), 1567–1570 (2007)
- [4] D. Bouwmeester et al., "Experimental quantum teleportation," *Nature* 390(6660), 575–579 (1997)

- [5] Z.-D. Li et al., “Experimental quantum repeater without quantum memory,” *Nat. Photonics* 13(9), 644–648 (2019)
- [6] D. P. Ornelas-Huerta et al., “On-demand indistinguishable single photons from an efficient and pure source based on a Rydberg ensemble,” *Optica* 7(7), 813–819 (2020)
- [7] X.-L. Chu, S. Götzinger, and V. Sandoghdar, “A single molecule as a high-fidelity photon gun for producing intensity-squeezed light,” *Nat. Photonics* 11(1), 58–62 (2017)
- [8] Y.-M. He et al., “Deterministic implementation of a bright, on-demand single-photon source with near-unity indistinguishability via quantum dot imaging,” *Optica* 4(7), 802–808 (2017)
- [9] Couteau, Christophe. "Spontaneous parametric down-conversion." *Contemporary Physics* 59.3, 291-304. (2018)
- [10] J. Szlachetka, K. Joarder, and P. Kolenderski, Ultrabright source of non-degenerate polarization-entangled photon pairs based on off-the-shelf polarization optics, *Applied Physics Letters* 123 (2023).
- [11] Kwiat, P. G., Waks, E., White, A. G., Appelbaum, I., & Eberhard, P. H. Heralded single-photon sources. *Physical Review A*, 63(2), 022303. (2001)
- [12] Aurea TPS_1550, <https://www.aureatechnology.com/photonics-instruments/> accessed: 2025.06.18.
- [13] Oz Optics Polarization entangled photon sources, <https://www.ozoptics.com/products/polarization-entangled-photon-sources.html>, accessed: 2025.06.18.
- [14] Thorlabs Correlated photon-pair sources, https://www.thorlabs.com/newgrouppage9.cfm?objectgroup_id=13675, accessed: 2025.06.18.
- [15] Saleh, Bahaa E. A., and Malvin Carl Teich. *Fundamentals of Photonics*. 3rd ed., Wiley, Section: Nonlinear Optics (2019)
- [16] Boyd, R. W. *Nonlinear Optics* (4th ed.). Academic Press. Chapter 2, Section 2.2, "Phase Matching." (2020)
- [17] Fejer, M. M., Magel, G. A., Jundt, D. H., & Byer, R. L. Quasi-Phase-Matched Second Harmonic Generation: Tuning and Tolerances. *IEEE Journal of Quantum Electronics*, 28(11), 2631–2654. (1992)
- [18] Powers, P. E., & Haus, J. W. *Fundamentals of Nonlinear Optics* (2nd ed.). Chapter 5, CRC Press. (2017)

- [19] Saleh, Bahaa E. A., and Malvin Carl Teich. *Fundamentals of Photonics*. 3rd ed., Wiley, Section: 6.3 Optics of Anisotropic Media (2019)
- [20] H. D. L. Pires, F. M. G. J. Coppens, and M. P. Van Exter, "Type-i spontaneous parametric down-conversion with a strongly focused pump," *Phys. Rev. A* 83(3), 033837 (2011)
- [21] Dirac, Paul Adrien Maurice. "A new notation for quantum mechanics." *Mathematical proceedings of the Cambridge philosophical society*. Vol. 35. No. 3. Cambridge University Press, (1939)
- [22] Fox, Mark. *Quantum Optics: An Introduction*. Oxford University Press, Chapter 2 (2006)
- [23] Nielsen, Michael A., and Isaac L. Chuang. *Quantum Computation and Quantum Information*. Cambridge University Press, Chapter 2, "Quantum Mechanics in Hilbert Space," and Chapter 4, "Quantum Entanglement." (2000)
- [24] Altepeter, Joseph B., Evan R. Jeffrey, and Paul G. Kwiat. "Photonic state tomography." *Advances in atomic, molecular, and optical physics* 52 105-159. (2005)
- [25] Kwiat group online Polarization Tomography Interface, <https://tomography.web.engr.illinois.edu/TomographyDemo.php>, accessed 17.06.2025.
- [26] Snyder, A. W., and J. D. Love. *Optical Waveguide Theory*. Springer, (1983)
- [27] Siegman, Anthony E. *Lasers*. University Science Books, (1986)
- [28] Marcuse, Dietrich. *Theory of Dielectric Optical Waveguides*. 2nd ed., Academic Press, (1991)
- [29] Ansys Zemax opticstudio, <https://www.ansys.com/products/optics/ansys-zemax-opticstudio>, accessed 09.12.2024.
- [30] Sang Min Lee, Heonoh Kim, Myoungsik Cha, and Han Seb Moon, "Polarization-entangled photon-pair source obtained via type-II non-collinear SPDC process with PPKTP crystal," *Opt. Express* 24, 2941-2953 (2016)
- [31] Shin Arahira, Tadashi Kishimoto, and Hitoshi Murai, "1.5- μm band polarization entangled photon-pair source with variable Bell states," *Opt. Express* 20, 9862-9875 (2012)
- [32] C.H.Bennett, "Quantum cryptography using any two nonorthogonal states" *Phys.Rev.Lett* 68, 3121(1992)
- [33] Aspect, Alain, Philippe Grangier, and Gérard Roger. "Experimental tests of realistic local theories via Bell's theorem." *Physical review letters* 47.7 460 (1981)

- [34] P. G. Kwiat, et al., New High-Intensity Source of Polarization-Entangled Photon Pairs, *Phys. Rev. Lett.* 75, 4337 (1995)
- [35] P. G. Kwiat, et al., Ultrabright source of polarization-entangled photons, *Phys. Rev. A* 60, R773 (1999)
- [36] T. Kim, M. Fiorentino, and F. N. C. Wong, Phase-stable source of polarization-entangled photons using a polarization Sagnac interferometer, *Phys. Rev. A* 73, 012316 (2006)
- [37] Fedrizzi, Alessandro, et al. "A wavelength-tunable fiber-coupled source of narrowband entangled photons." *Optics Express* 15.23 15377-15386 (2007)
- [38] Fiorentino, Marco, et al. "Spontaneous parametric down-conversion in periodically poled KTP waveguides and bulk crystals." *Optics express* 15.12 7479-7488 (2007)
- [39] König, Friedrich, et al. "Efficient and spectrally bright source of polarization-entangled photons." *Physical Review A—Atomic, Molecular, and Optical Physics* 71.3 033805 (2005)
- [40] Fiorentino, Marco, et al. "Generation of ultrabright tunable polarization entanglement without spatial, spectral, or temporal constraints." *Physical Review A—Atomic, Molecular, and Optical Physics* 69.4 041801 (2004)
- [41] F. Steinlechner, et al., A high-brightness source of polarization-entangled photons optimized for applications in free space, *Opt. Express* 20, 9640 (2012)
- [42] H. Kim, O. Kwon, and H. S. Moon, Pulsed Sagnac source of polarization-entangled photon pairs in telecommunication band, *Sci. Rep.* 9, 5031 (2019)
- [43] Y.-H. Li, Z.-Y. Zhou, Z.-H. Xu, L.-X. Xu, B.-S. Shi, and G.-C. Guo, Multiplexed entangled photon-pair sources for all-fiber quantum networks, *Physical Review A* 94, 043810 (2016).
- [44] R. Ursin, et al., Entanglement-based quantum communication over 144 km, *Nat. Phys.* 3, 481 (2007)
- [45] S. P. Neumann, A. Buchner, L. Bulla, M. Bohmann, and R. Ursin, Continuous entanglement distribution over a transnational 248 km fiber link, *Nature Communications* 13, 6134 (2022)
- [46] S. P. Neumann, M. Selimovic, M. Bohmann, and R. Ursin, Experimental entanglement generation for quantum key distribution beyond 1 gbit/s, *Quantum* 6, 822 (2022)
- [47] Yin, Juan, et al. "Satellite-to-ground entanglement-based quantum key distribution." *Physical review letters* 119.20 200501 (2017)

- [48] Yin, Juan, et al. "Entanglement-based secure quantum cryptography over 1,120 kilometres." *Nature* 582.7813 501-505 (2020)
- [49] Ulrich, R., S. C. Rashleigh, and W. Eickhoff. "Bending-Induced Birefringence in Single-Mode Fibers." *Optics Letters*, vol. 5, no. 6, pp. 273–275. (1980)
- [50] A. Dragan, "Efficient fiber coupling of down-conversion photon pairs," *Phys. Rev. A* 70(5), 053814 (2004)
- [51] H. Kuniyil and K. Durak, "Efficient coupling of down-converted photon pairs into single mode fiber," *Opt. Commun.* 493, 127038 (2021)
- [52] H. Vanherzeele and C. Chen, "Widely tunable parametric generation in beta barium borate," *Appl. Opt.* 27(13), 2634–2636 (1988)
- [53] A. Anwar, "Characterization of quantum sources of light generated by parametric downconversion processes," PhD dissertation, Mohanlal Sukhadia University, Ahmedabad, India (2018)
- [54] J.-C. Lee and Y.-H. Kim, "Spatial and spectral properties of entangled photons from spontaneous parametric down-conversion with a focused pump," *Opt. Commun.* 366, 442–450 (2016)
- [55] L. Mandel and E. Wolf, *Optical Coherence and Quantum Optics*, in *Photoelectric Counting Statistics of a Fluctuating Field*, Cambridge University Press, New York (1995)
- [56] M. Avenhaus et al., "Photon number statistics of multimode parametric down-conversion," *Phys. Rev. Lett.* 101(5), 053601 (2008)
- [57] H. E. Guilbert and D. J. Gauthier, "Enhancing heralding efficiency and biphoton rate in type-i spontaneous parametric down-conversion," *IEEE J. Sel. Top. Quantum Electron.* 21(3), 215–224 (2014)
- [58] K. G. Katamadze et al., "Broadband biphotons in a single spatial mode," *Phys. Rev. A* 92(2), 023812 (2015)
- [59] Y.-C. Jeong et al., "Deterministic secure quantum communication on the bb84 system," *Entropy* 22(11), 1268 (2020)
- [60] J. Lee et al., "Symmetrical clock synchronization with time-correlated photon pairs," *Appl. Phys. Lett.* 114(10), 101102 (2019).
- [61] C.-K. Hong, Z.-Y. Ou, and L. Mandel, "Measurement of subpicosecond time intervals between two photons by interference," *Phys. Rev. Lett.* 59, 2044 (1987)
- [62] N. Takanashi, et al., "All-optical phase-sensitive detection for ultra-fast quantum computation," *Opt. Express* 28, 34916 (2020)

- [63] A. Villar, A. Lohrmann, and A. Ling, Experimental entangled photon pair generation using crystals with parallel optical axes, *Opt. Express* 26, 12396 (2018)
- [64] F. Steinlechner, et al., Efficient heralding of polarization-entangled photons from type-0 and type-II spontaneous parametric downconversion in periodically poled KTiOPO₄, *J. Opt. Soc. Am. B* 31, 2068 (2014)
- [65] A. Lohrmann, C. Perumangatt, A. Villar, and A. Ling, Broadband pumped polarization entangled photon-pair source in a linear beam displacement interferometer, *Appl. Phys. Lett.* 116, 021101 (2020)
- [66] C. Perumangatt, A. Lohrmann, and A. Ling, Experimental conversion of position correlation into polarization entanglement, *Phys. Rev. A* 102, 012404 (2020)
- [67] E. Knill, R. Laflamme, and G. J. Milburn, A scheme for efficient quantum computation with linear optics, *Nature (London)* 409, 46 (2001)
- [68] J. Chen, K. F. Lee, C. Liang, and P. Kumar, Fiber-based telecom-band degenerate-frequency source of entangled photon pairs, *Opt. Lett.* 31, 2798 (2006)
- [69] D. E. Zelmon, D. L. Small, D. Jundt. Infrared corrected Sellmeier coefficients for congruently grown lithium niobate and 5 mol.% magnesium oxide-doped lithium niobate. *J. Opt. Soc. Am. B* 14, 3319-3322 (1997)
- [70] Willey, Ronald R. *Field Guide to Optical Thin Films*. SPIE Press, (2006)
- [71] Hendrych, Martin, and R. Filip. "Simple optical measurement of the overlap and fidelity of quantum states." *Physical Review A*, vol. 71, no. 6, p. 062310 (2005)
- [72] C. Erven, C. Couteau, R. Laflamme, and G. Weihs, Entangled quantum key distribution over two free-space optical links, *Opt. Express* 16, 16840 (2008).
- [73] C.-K. Hong, Z.-Y. Ou, and L. Mandel, Measurement of subpicosecond time intervals between two photons by interference, *Physical review letters* 59, 2044 (1987)
- [74] J. Chen, K. F. Lee, and P. Kumar, Deterministic quantum splitter based on time-reversed hong-ou-mandel interference, *Physical Review A—Atomic, Molecular, and Optical Physics* 76, 031804 (2007)
- [75] Y. Chen, S. Ecker, S. Wengerowsky, L. Bulla, S. K. Joshi, F. Steinlechner, and R. Ursin, Polarization entanglement by time-reversed hong-ou-mandel interference, *Physical Review Letters* 121, 200502 (2018)

[76] G. S. Monk, *Light: principles and experiments*, 1st ed. (McGraw-Hill, 1937) pp. 376–380.

10 Appendix

10.1 Probabilities computed with Poissonian distribution

As mentioned in Subsection 5.3, if the laser I use for pumping the photon pair source is a coherent, continuous-wave source, and the integration time corresponding to my measurements is much greater than the coherence time of SPDC light, then the photon statistics at fiber outputs can be regarded as Poissonian [55][56].

If a random variable X follows a Poissonian distribution that has an expected value of λ , then the probability of $X = k$ can be calculated as

$$P(X = k) = \frac{\lambda^k \exp(-\lambda)}{k!}. \quad (78)$$

In my case X is the number of photons counted during the integration time.

Eq. (24) in Subsection 5.3 shows the pump photon-related random coincidence flux Φ_p^r in the case when the τ coincidence window (i.e. the integration time) contains one or more photons of any kind at one fiber output and at least one pump photon at the other (with down-converted photons excluded).

To obtain this result I have to calculate the probabilities of three independent events:

1. τ contains one or more photons of any kind at one fiber output.

The expected value of such an event is $\lambda = (\Phi_s + \Phi_p)\tau$, since I have to take both pump and SPDC photons into account. I am looking for $P(X > 0)$ that can be calculated substituting into Eq. (78) as

$$P(X > 0) = 1 - P(X = 0) = 1 - \exp(-(\Phi_s + \Phi_p)\tau). \quad (79)$$

2. τ contains at least one pump photon at the other fiber output.

Now the expected value is $\lambda = \Phi_p\tau$, and the desired probability is again

$$P(X > 0) = 1 - P(X = 0) = 1 - \exp(-\Phi_p\tau). \quad (80)$$

3. τ contains no down-converted photons at the other fiber output.

For which the expected value is $\lambda = \Phi_s\tau$, but now the probability I want to calculate is

$$P(X = 0) = \exp(-\Phi_s\tau). \quad (81)$$

Since these three are independent of each other the probability of having all at once is the product of each individual probability. In a coincidence window maximum one

coincidence event can be measured. So to obtain the Φ_p^r flux value of Eq. (24) I have to divide the product with the τ temporal width of the coincidence window.

A similar reasoning applies to Eq. (29) of Subsection 5.5 which shows the random coincidence detection rate. These random coincidences occur when two independent photons hit the two detectors within the same τ time window. I consider those photons as independent, whose pair were not coupled into the other output fiber. The probability of coupling and detecting a photon in the output, given that its pair was already detected is $\mathbb{P}_h \cdot \eta_{\text{det}}$. Therefore not detecting the pair of an already detected photon yields $1 - \mathbb{P}_h \cdot \eta_{\text{det}}$ probability. If \mathcal{R}_s is the detection rate on one detector, then $\mathcal{R}_s \cdot (1 - \mathbb{P}_h \cdot \eta_{\text{det}})$ is the rate of photons on this same detector, whose pair was not detected. Hence, the expected value of detecting a photon in a τ coincidence window, whose pair was not detected is $\lambda = \mathcal{R}_s \cdot (1 - \mathbb{P}_h \cdot \eta_{\text{det}}) \cdot \tau$. We have to substitute this into Eq. (78) to obtain the probability of detecting at least one photon without detecting its pair as

$$P(X > 0) = 1 - P(X = 0) = 1 - \exp(-\mathcal{R}_s \cdot (1 - \mathbb{P}_h \cdot \eta_{\text{det}}) \cdot \tau). \quad (82)$$

These kind of events are independent on the two detectors, so I have to square this probability to derive the probability of a random coincidence count, and divide it with the coincidence window to obtain \mathcal{R}_s^r the random coincidence detection rate of Eq. (29).

10.2 Parallel beam shift of tilted glass plate

Figure 34 of Subsection 7.2 presents possible solutions for tuning the phase of the inverse HOM interference. To justify my choice from the listed arrangements in Figure 34, here I present the detailed calculation concerning the parallel beam shift in case a) and d). Figure 39 shows how a beam is refracted during propagation through a plane-parallel plate made of a material with greater refractive index than its environment. I assumed the refractive index of the surrounding air to be 1.0, while the refractive index of the applied Schott NBK-7 glass for the wavelength of the pump laser $\lambda_p = 405$ nm is $n_p = 1.5302$.

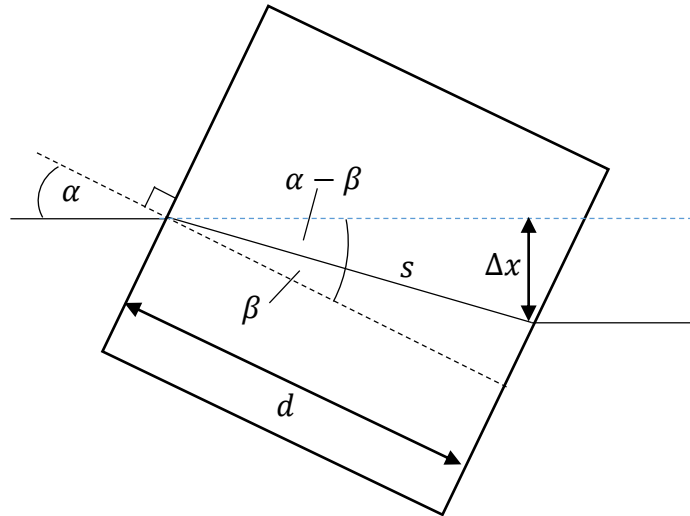


Figure 39. Parallel beam shift for α angle of incidence when the beam is propagating through a plane-parallel plate.

The connection between the angle of incidence α and refraction β is given by Snell's law

$$\sin \alpha = n_p \cdot \sin \beta. \quad (83)$$

Therefore, the angle of refraction is

$$\beta = \arcsin\left(\frac{\sin \alpha}{n_p}\right). \quad (84)$$

The length of the beam path inside the glass s can be calculated from a simple trigonometric expression

$$s = \frac{d}{\cos \beta}. \quad (85)$$

So the Δx parallel beam shift for a given α angle of incidence and d thickness of the plate is calculated as

$$\Delta x(d, \alpha) = s \cdot \sin(\alpha - \beta) = \frac{d}{\cos\left(\arcsin\left(\frac{\sin \alpha}{n_p}\right)\right)} \sin\left(\alpha - \arcsin\left(\frac{\sin \alpha}{n_p}\right)\right). \quad (86)$$

In the simplest case of a) in Figure 34, one can calculate the result simply substituting $\alpha = \vartheta$ and $2d$ thickness, namely $\Delta x(2d, \Delta\vartheta)$.

However, in case d) of Figure 34, with the glass plate in front of the mirror, the beam shift caused by the $\Delta\vartheta$ tilt should be compared to the case when the glass plate is initially parallel to the mirror. In the parallel position (see c) in Figure 34) the angle of incidence is $\alpha = \vartheta = 22.5^\circ$ and later, when the plate is tilted $\Delta\vartheta$ modifies the value. Since the beam is reflected on the mirror, two shifts have to be calculated. One with the angle of incidence $\alpha = \vartheta - \Delta\vartheta$ and one with $\alpha = \vartheta + \Delta\vartheta$. These two add up, and should be compared to the initial $\alpha = \vartheta$ state. Therefore the remnant parallel displacement of this setup $\Delta x'$ can be calculated as

$$\Delta x'(d, \Delta\vartheta) = \Delta x(d, \vartheta - \Delta\vartheta) + \Delta x(d, \vartheta + \Delta\vartheta) - 2\Delta x(d, \vartheta). \quad (87)$$

Case a) and case d) of Figure 34 should be compared. In case a) the beam shift equals $\Delta x(2d, \Delta\vartheta)$, while in case d) it is $\Delta x'(d, \Delta\vartheta)$. Both expressions are plotted in Figure 40. From the graph it is clear that in the range of $\Delta\vartheta \in [0^\circ, 9^\circ]$ necessary to properly tune the inverse HOM interference, $\Delta x'$ remains one order of magnitude less than Δx .

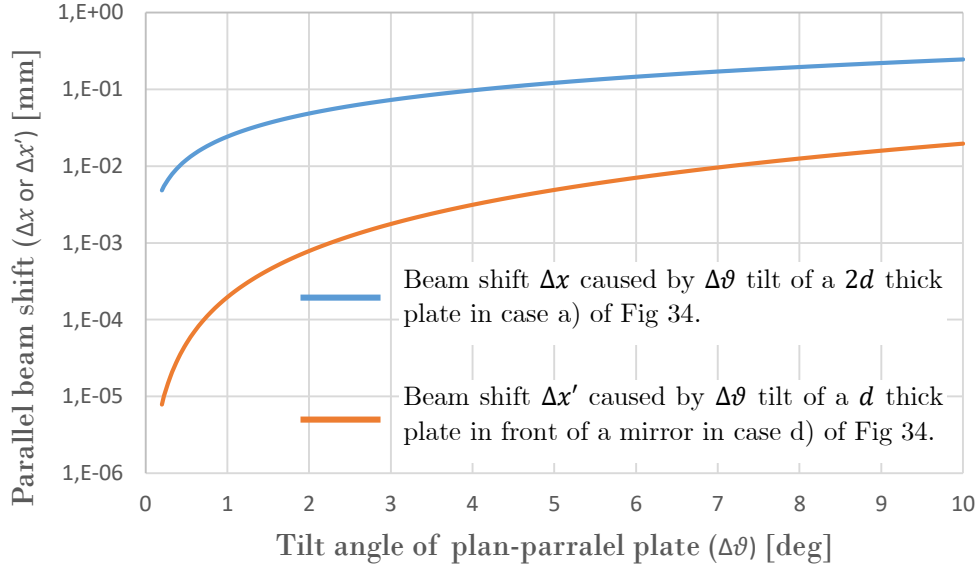


Figure 40. Parallel beam shift caused by propagating a beam through a tilted plane-parallel glass plate. Blue curve corresponds to case a) of Figure 34, while orange curve to case d).

10.3 Transforming fitting function parameters

Here I present how Eq. (74) of Subsection 8.2 can be transformed to Eq. (60), the actual function fitted on the measurement data, by using the parameter definitions Eq. (75) and (76).

Eq. (74) consists of a sum of two cosine functions, and my goal is to transform it to a single cosine curve fitted on the data, by connecting the A amplitude and φ_0 phase of the fitting function Eq. (60) to the q , κ and L parameters of Eq. (74). This can easily be done by representing all cosine terms with their corresponding phasor on the complex plane with $\varphi = 0$ constraint in Eq. (74), see Figure 41.

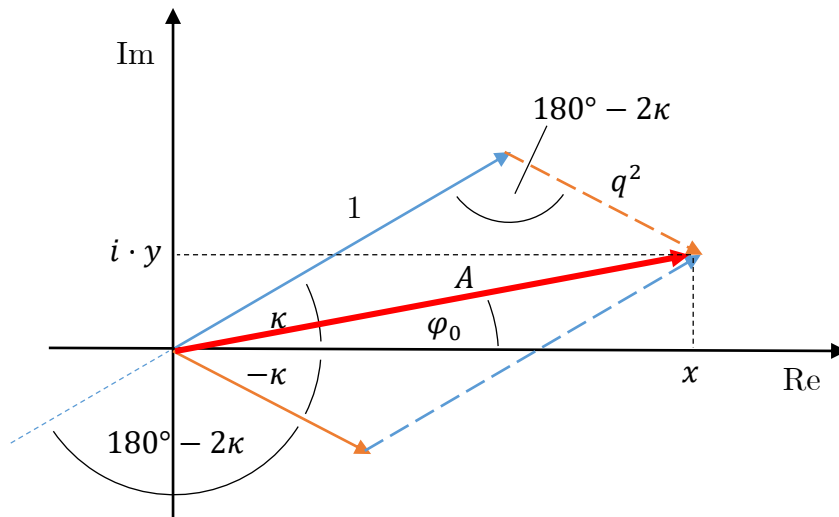


Figure 41. The blue and orange are the phasor representations of the two cosine functions in Eq. (74), while the thick red is their sum, corresponding to the cosine in Eq. (60).

The magnitude A of the resultant phasor can be calculated using the cosine law for the triangle formed by the solid blue, dashed orange and solid red triangle.

$$A = \sqrt{1^2 + q^4 - 2 \cdot 1 \cdot q^2 \cdot \cos(180^\circ - 2\kappa)} \quad (88)$$

This can be further simplified utilizing the properties of the cosine function to

$$A = \sqrt{1^2 + q^4 + 2q^2 \cos(2\kappa)}. \quad (89)$$

The normalization constant $L/(2 + 2q^2)$ is omitted in this derivation for simplicity, but of course is part of the full expression of A in Eq. (75).

The x and y coordinates of the sum can be calculated by simply summing the corresponding projections of the blue and orange phasors:

$$x = \cos(\kappa) + q^2 \cos(-\kappa) = \cos(\kappa)(1 + q^2) \quad (90)$$

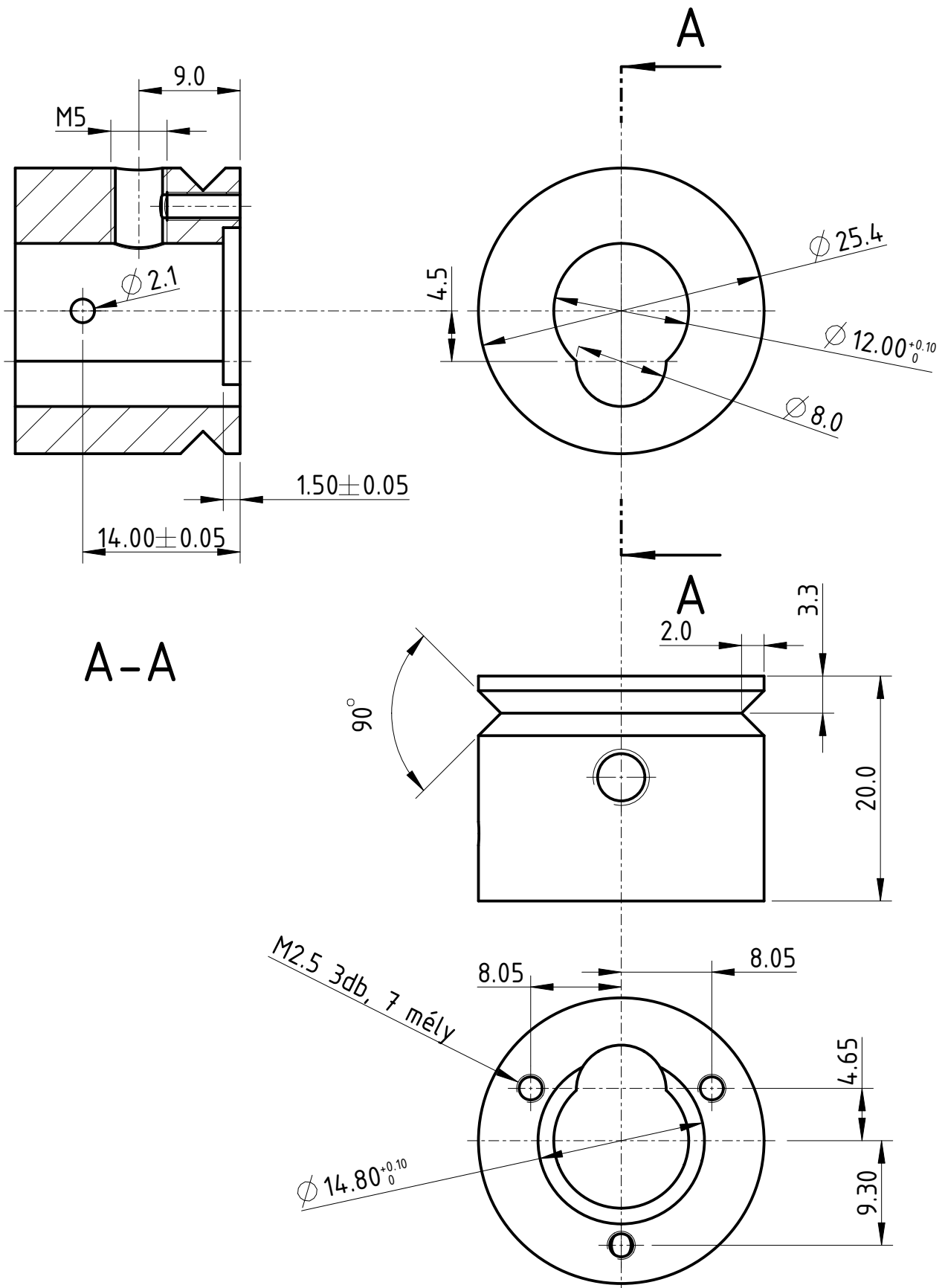
$$y = \sin(\kappa) + q^2 \sin(-\kappa) = \sin(\kappa)(1 - q^2) \quad (91)$$

Therefore, the resulting phase is

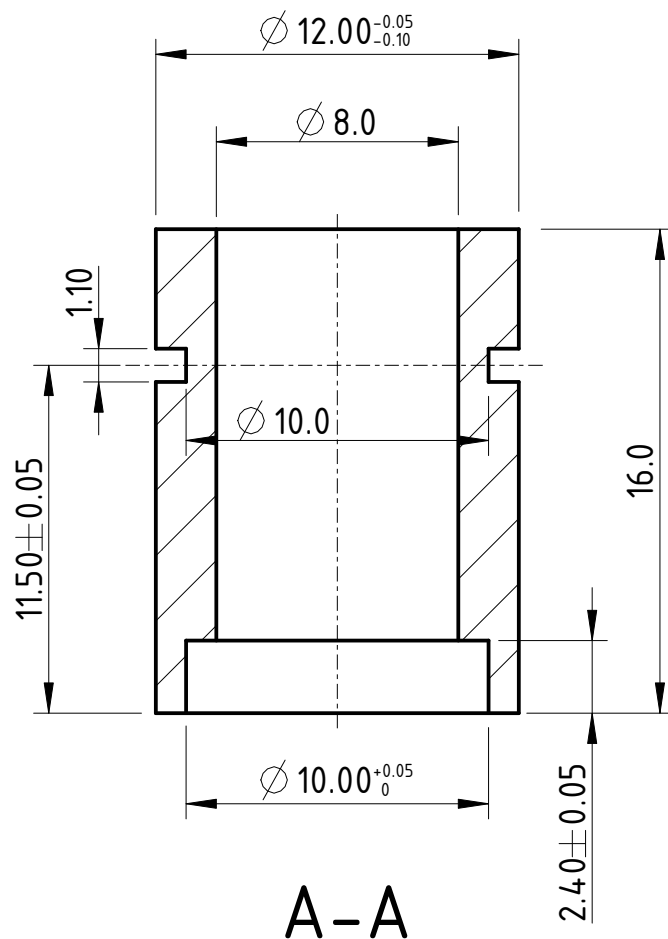
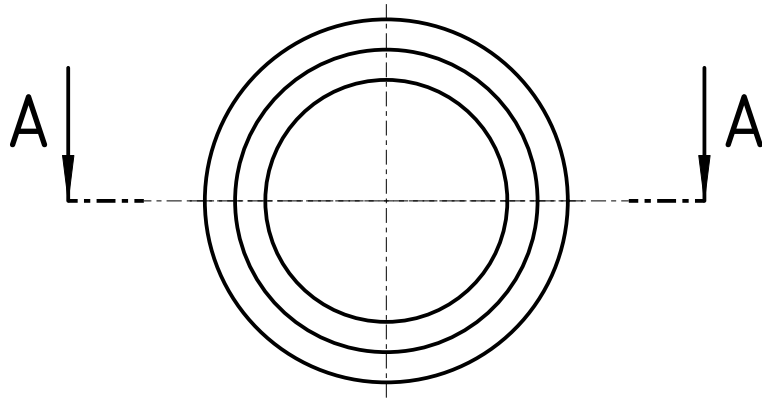
$$\varphi_0 = \operatorname{atan}\left(\frac{y}{x}\right) = \operatorname{atan}\left(\frac{\sin(\kappa)(1 - q^2)}{\cos(\kappa)(1 + q^2)}\right) = \operatorname{atan}\left(\tan(\kappa) \frac{(1 - q^2)}{(1 + q^2)}\right) \quad (92)$$

10.4 Manufacturing drawings

As an example, I provide here the manufacturing drawings of the custom mechanical elements I designed for the source shown in Figure 19 (excluding the also self-designed custom-made stiff base). All other source implementations, as well as certain measurement setups (e.g., SPAD fiber adapters and the HOM measurement retarder), required the design of custom parts of comparable number and complexity.

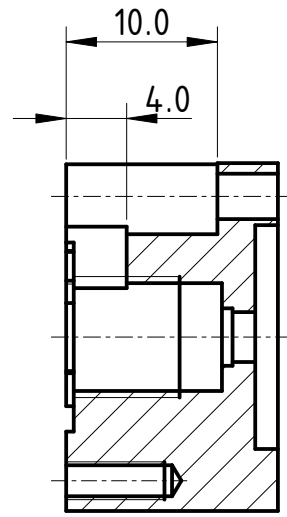
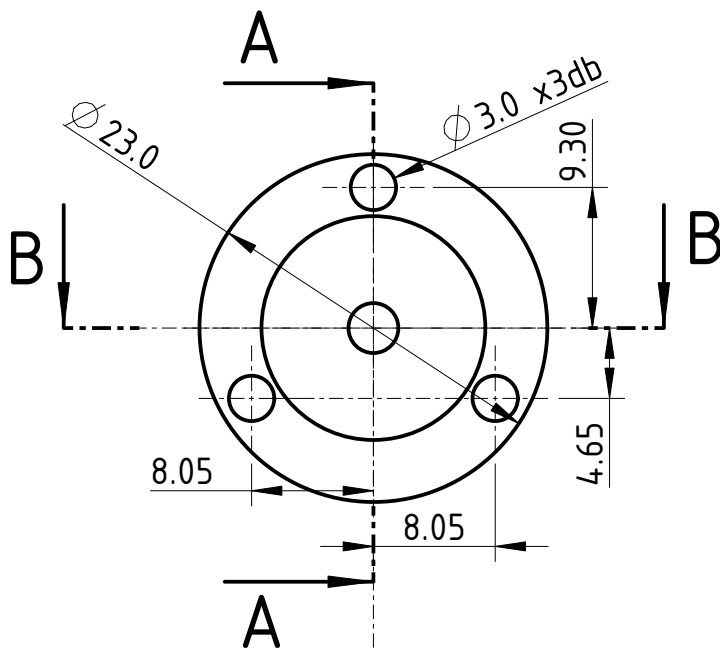


	Név:	Dátum:	Megnev.: lezer lencse tartó
Tervező:	?	2021/01/11	Projekt: SPDC szalcsatoló
Rajzoló:	-	-	Rajzszt.: - db: 1
Ellenőr:	-	-	M 2:1 Anyag: AlMgSi Oldal: 1/1

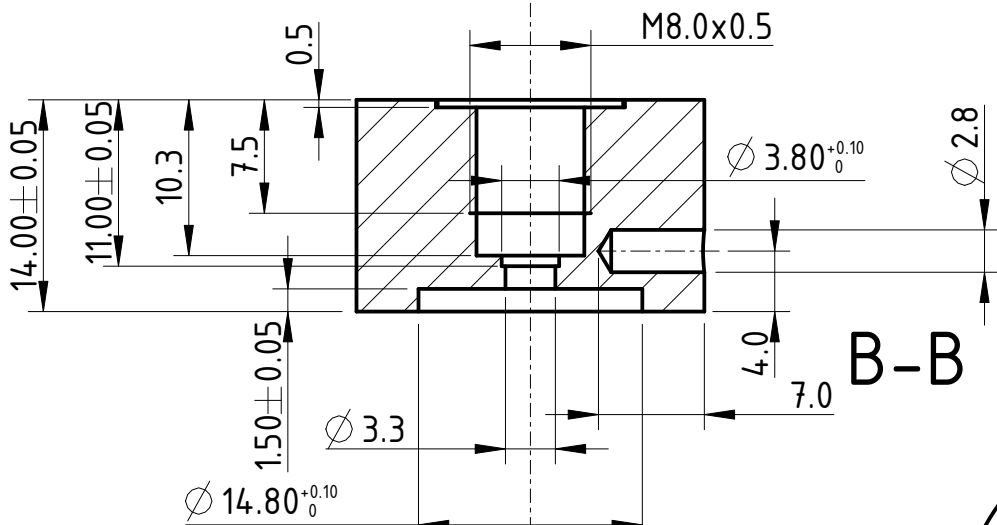


A-A

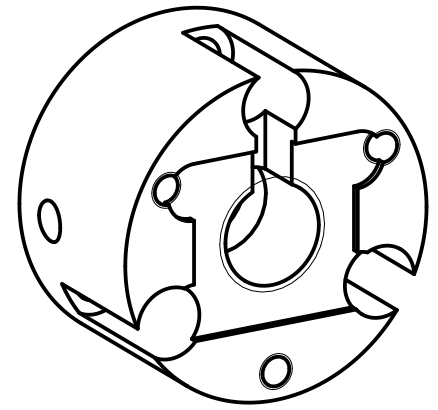
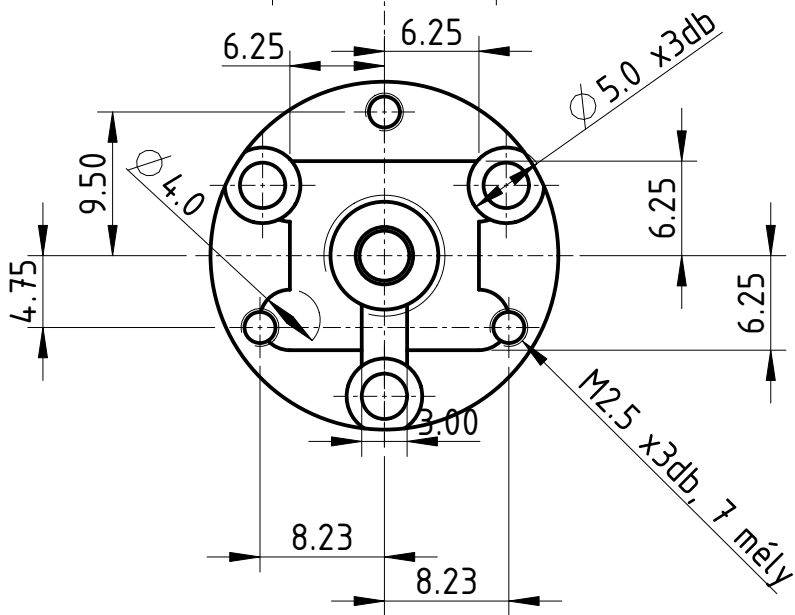
	Név:	Dátum:	Megnev.: lezer lencse tubus	
Tervező:	?	2021/01/11	Projekt: SPDC szalcsatólo	
Rajzoló:	-	-	Rajzsz.: -	db: 1
Ellenőr:	-	-	M 4:1	Anyag: AlMgSi Oldal: 1/1



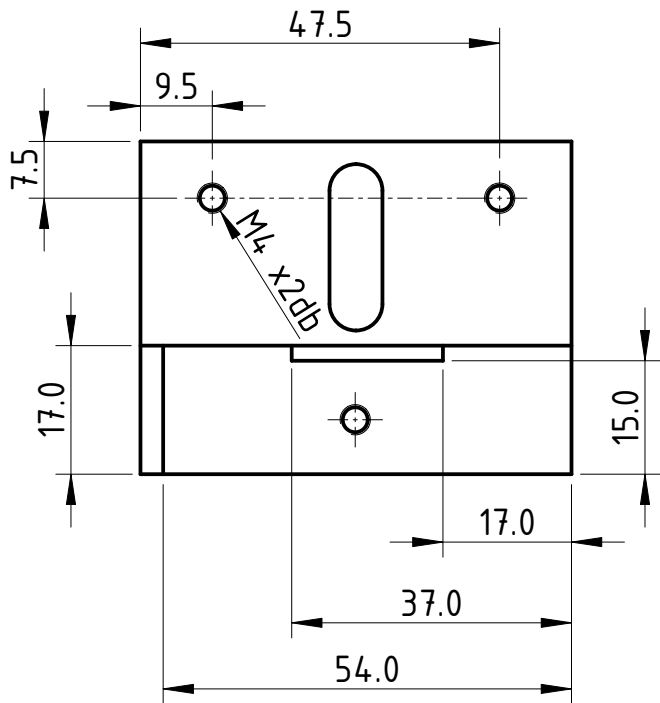
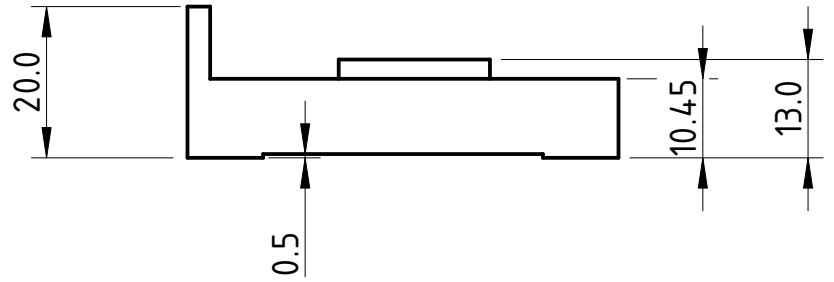
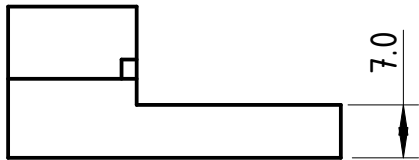
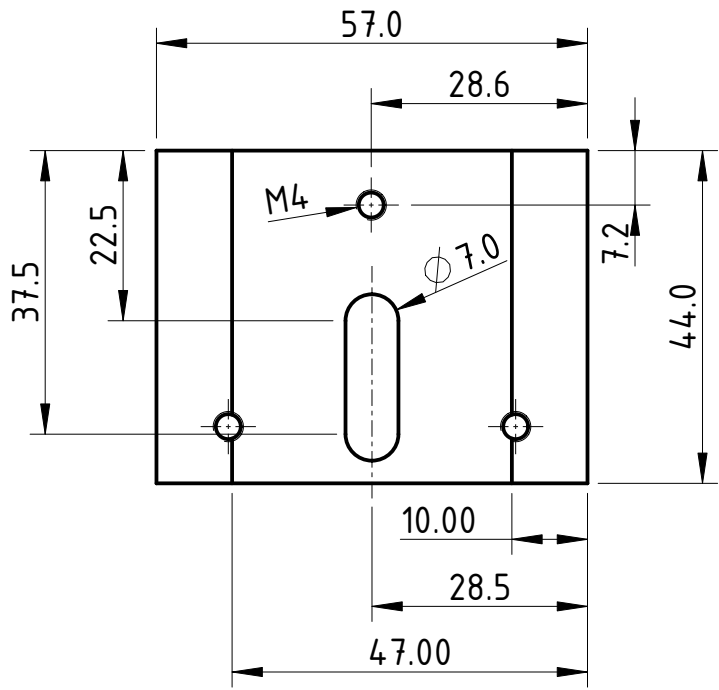
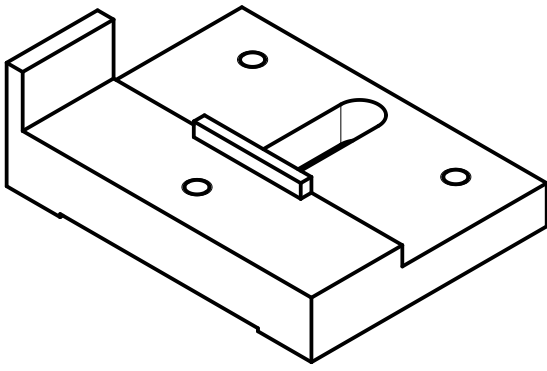
A-A



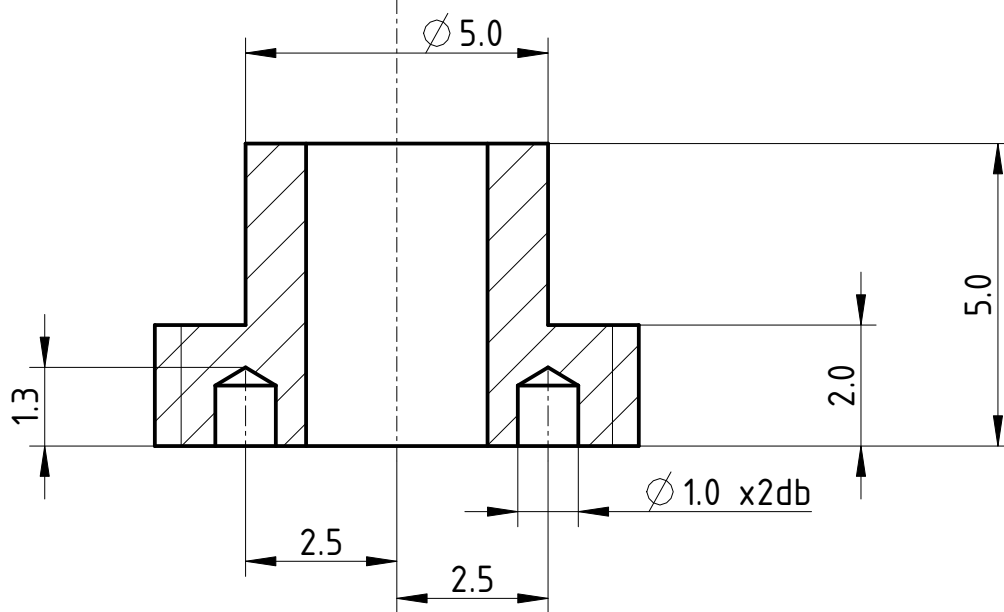
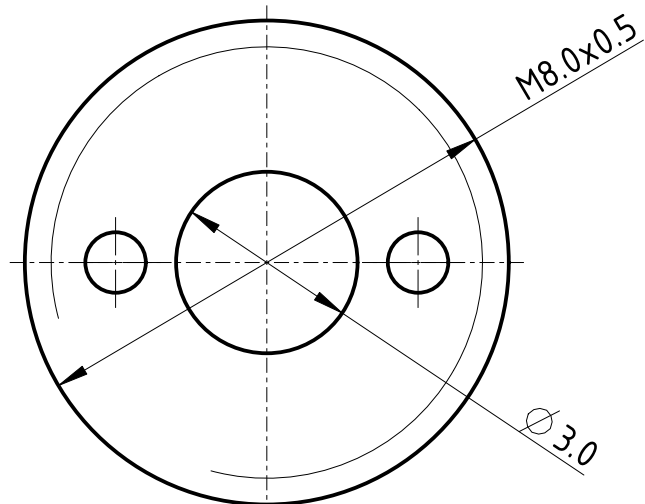
B-B



	Név:	Dátum:	Megnev.:	lezerdioda tartó
Tervező:	?	2021/01/12	Projekt:	SPDC szalcsatoló
Rajzoló:	-	-	Rajzsz.:	-
Ellenőr:	-	-	M 2:1	Anyag: sárgaréz
			db:	1
			Oldal:	1/1

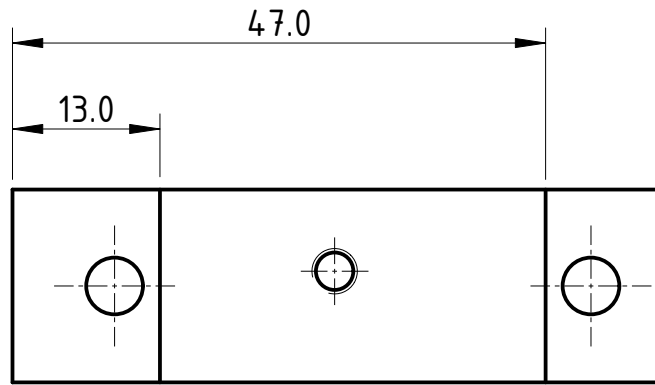
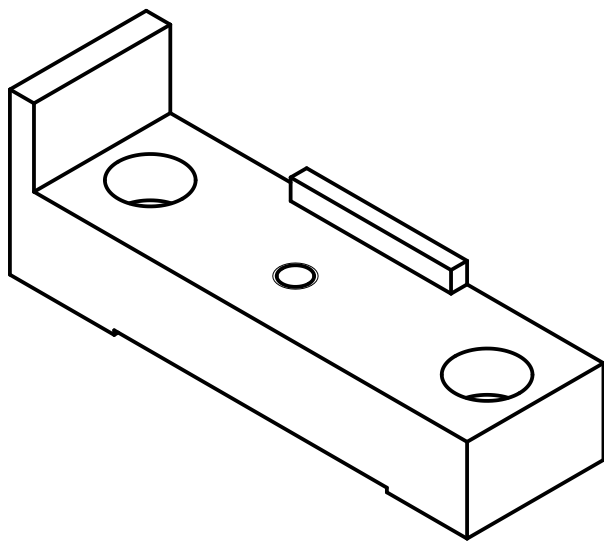


	Név:	Dátum:	Megnev.: lezer tologathato talp	
Tervező:	?	2021/01/12	Projekt: SPDC szalcsatolo	
Rajzoló:	-	-	Rajzsz.: -	db: 1
Ellenőr:	-	-	M 3:2	Anyag: AlMgSi Oldal: 1/1

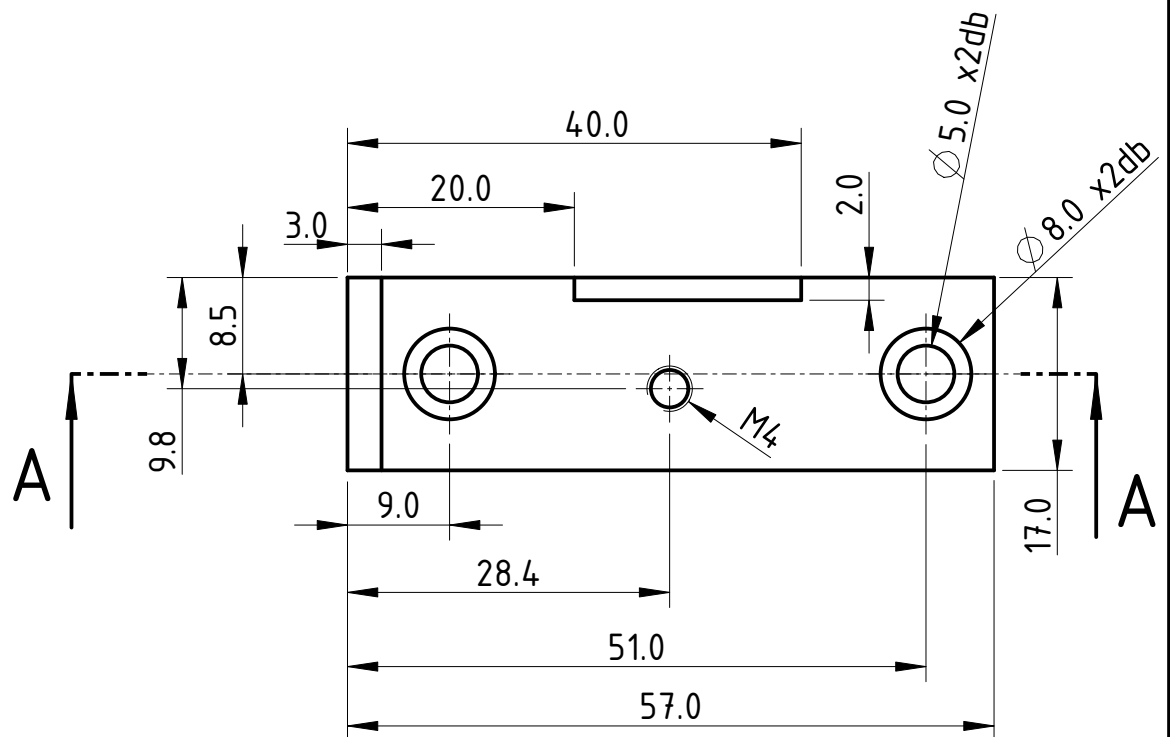
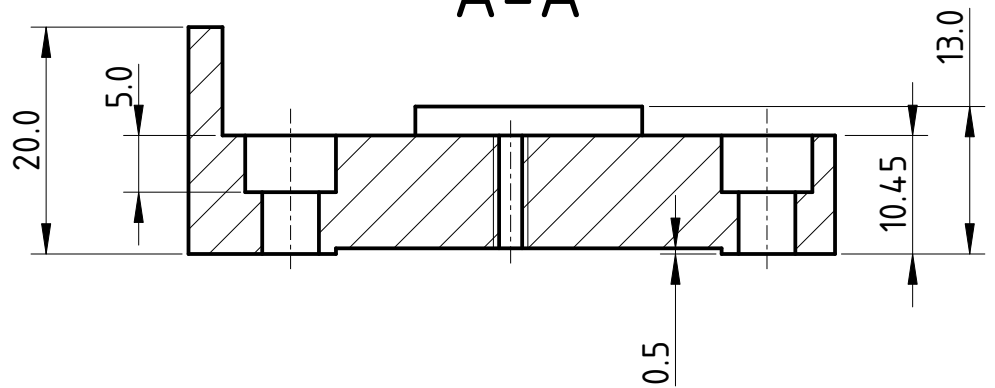


A-A

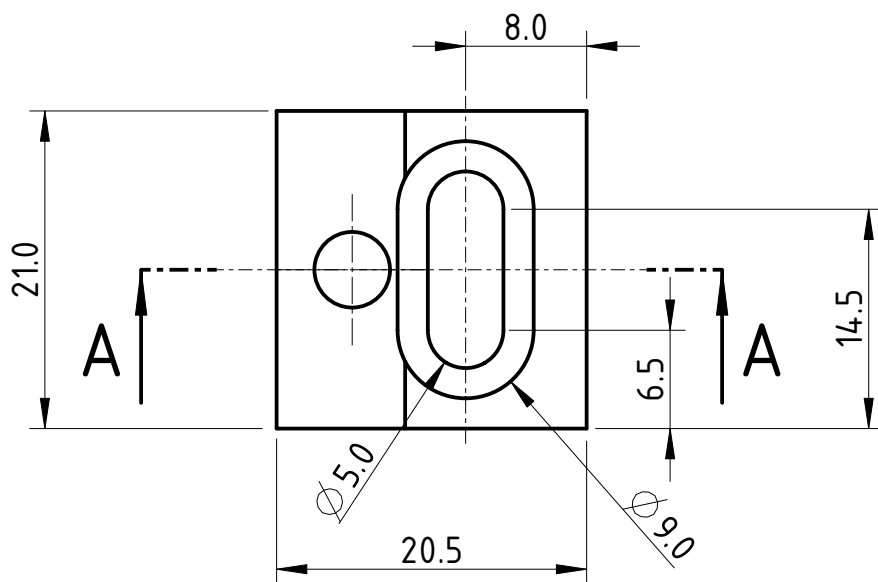
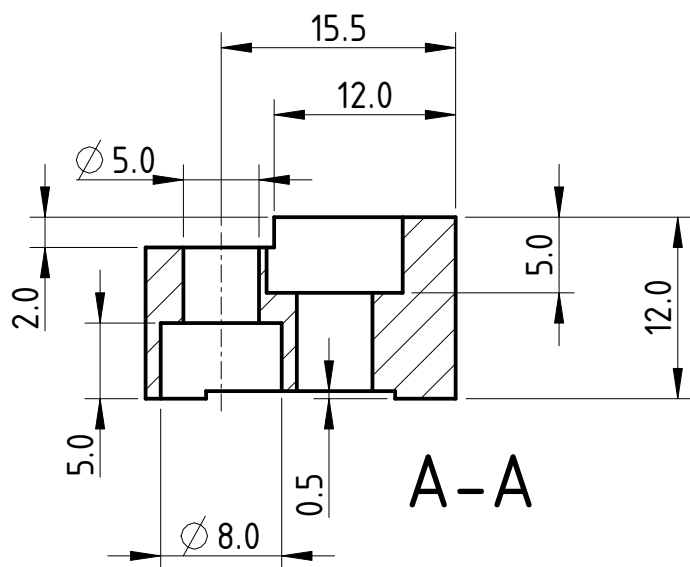
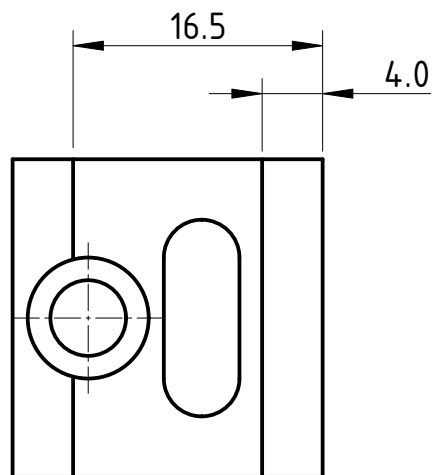
	Név:	Dátum:	Megnev.: lezer leszorító	
Tervező:	?	2021/01/11	Projekt: SPDC szalcsatóló	
Rajzoló:	-	-	Rajzsz.: -	db: 1
Ellenőr:	-	-	M 8:1	Anyag: sargarez Oldal: 1/1



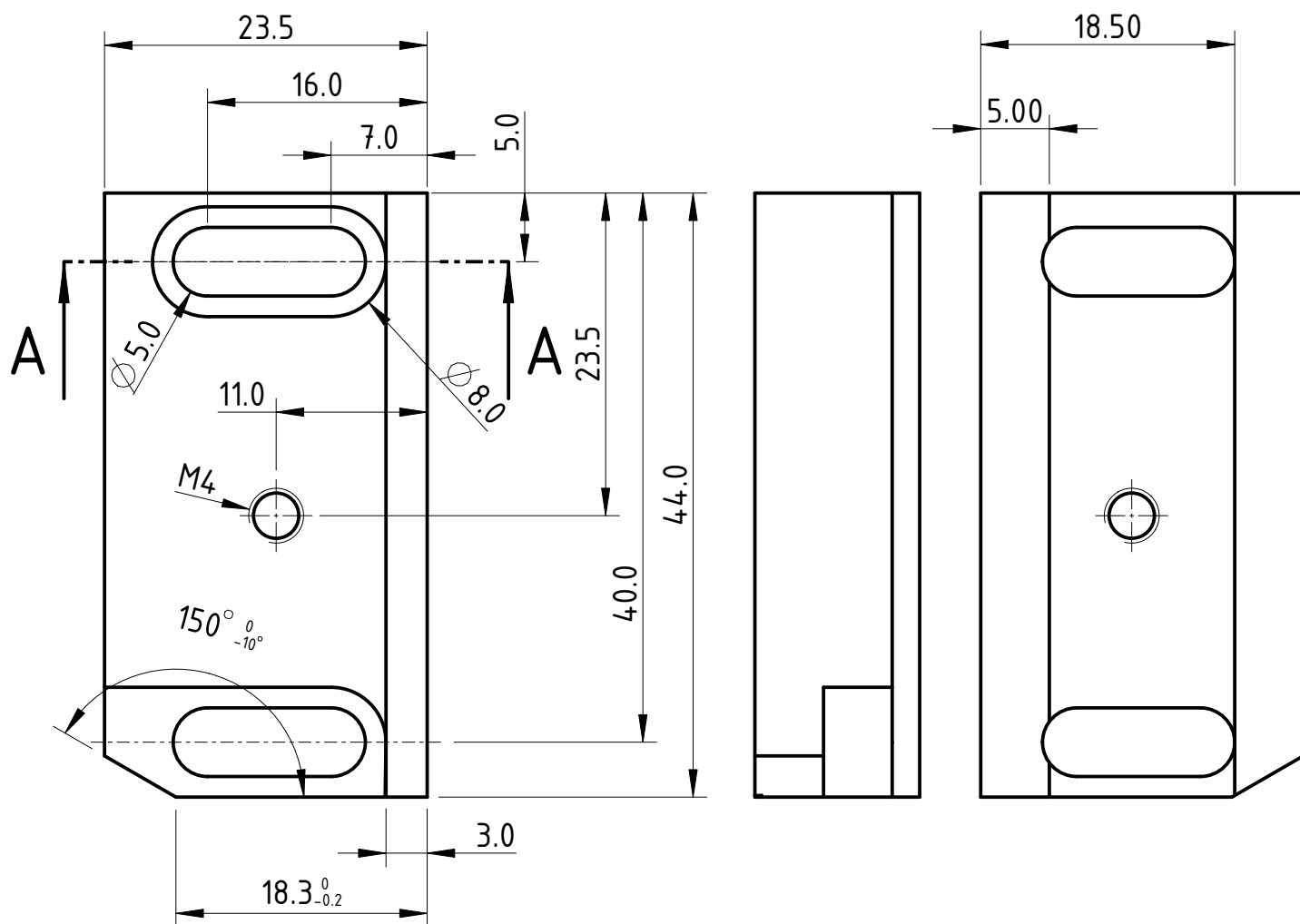
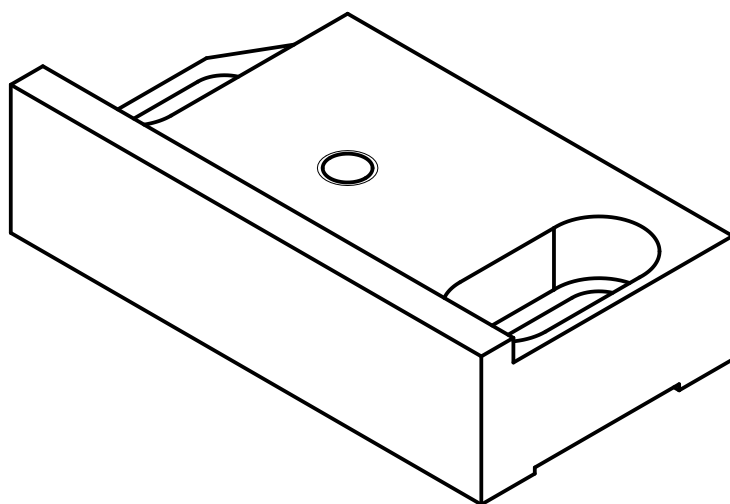
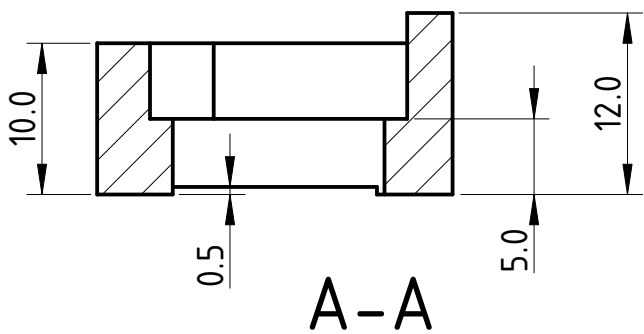
A-A



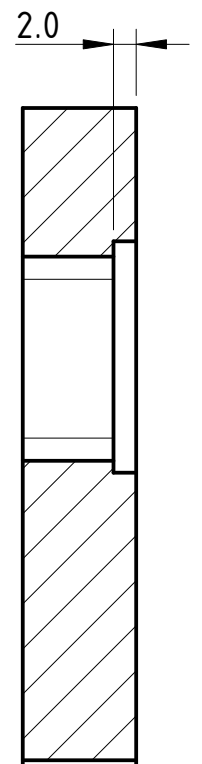
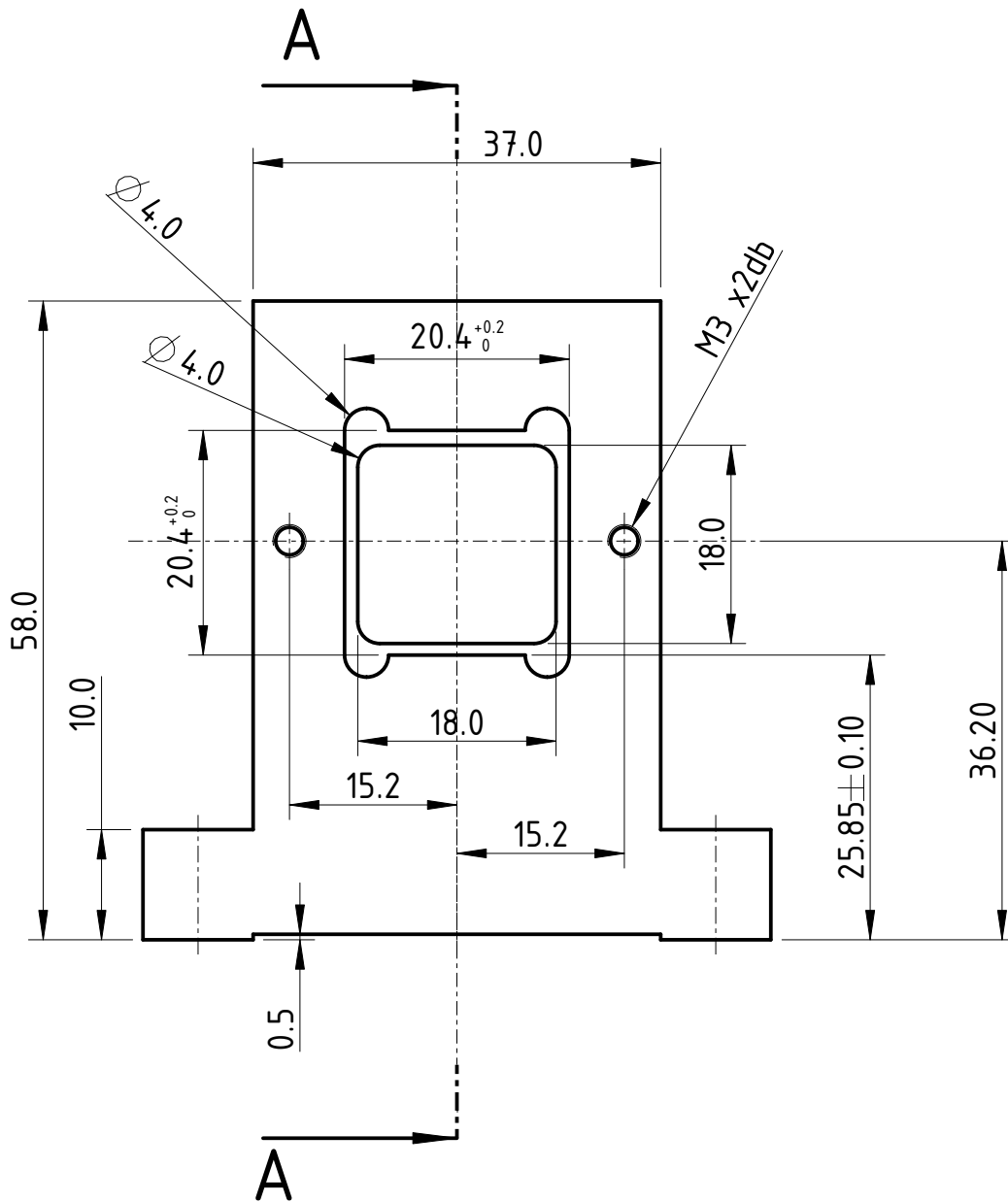
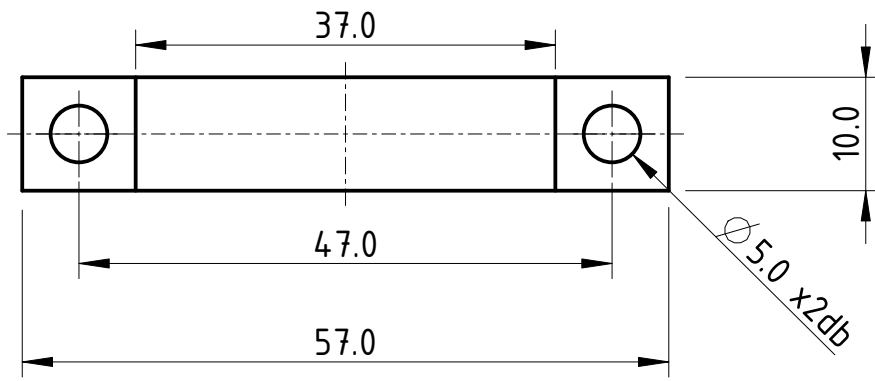
	Név:	Dátum:	Megnev.: dontogeto alap	
Tervező:	?	2020/07/14	Projekt: SPDC szalcsatolo	
Rajzoló:	-	-	Rajzsz.: -	db: 4
Ellenőr:	-	-	M 3:2	Anyag: AlMgSi Oldal: 1/1



	Név:	Dátum:	Megnev.: kis tukor tartó talp I	
Tervező:	?	2021/01/14	Projekt: SPDC szalcsatólo	
Rajzoló:	-	-	Rajzsz.: -	db: 2
Ellenőr:	-	-	M 2:1	Anyag: AlMgSi Oldal: 1/1

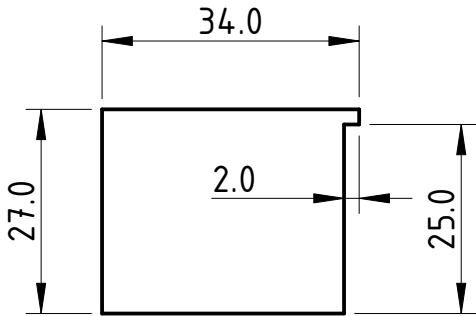
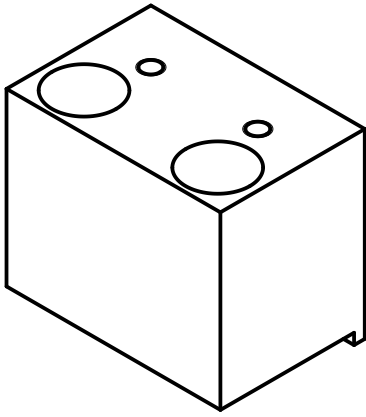


	Név:	Dátum:	Megnev.: kis tukortarto talp 2 (bal)	
Tervező:	?	2021/01/14	Projekt: SPDC szalcsatolo	
Rajzoló:	-	-	Rajzsz.: -	db: 1
Ellenőr:	-	-	M 2:1	Anyag: AlMgSi Oldal: 1/1

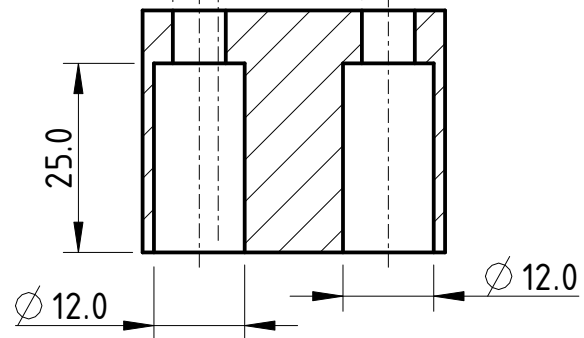
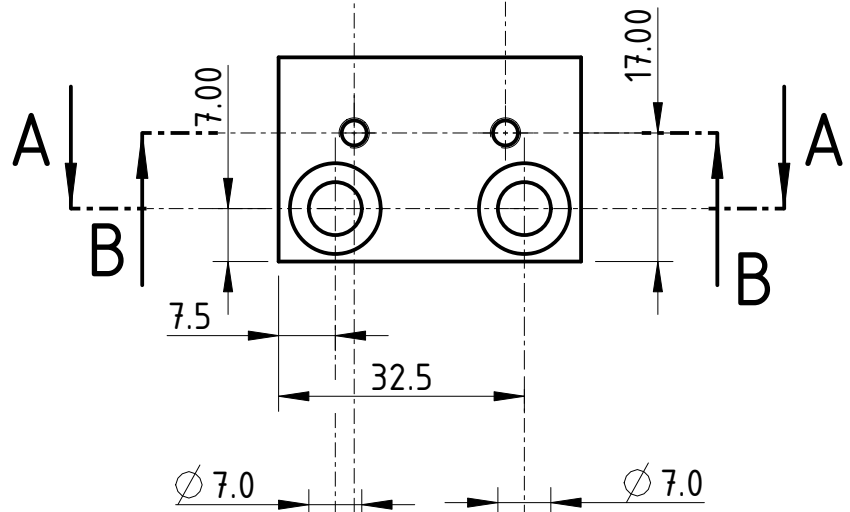
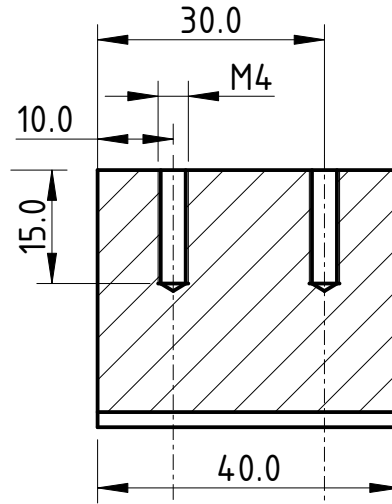


A-A

	Név:	Dátum:	Megnev.: lambda feles lemez tarto	
Tervező:	?	2021/01/12	Projekt: SPDC szalcsatolo	
Rajzoló:	-	-	Rajzsz.: -	db: 2
Ellenőr:	-	-	M 3:2	Anyag: AlMgSi Oldal: 1/1

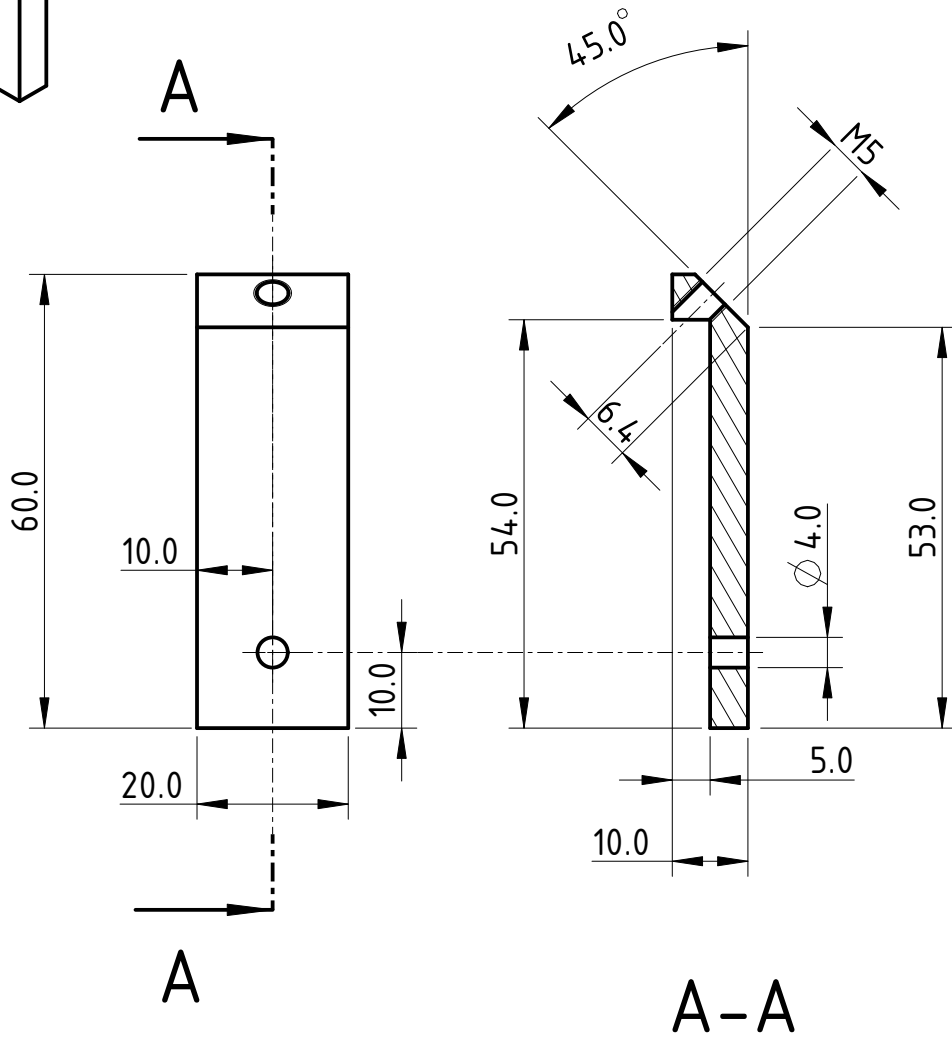
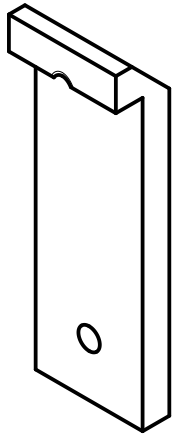


B-B

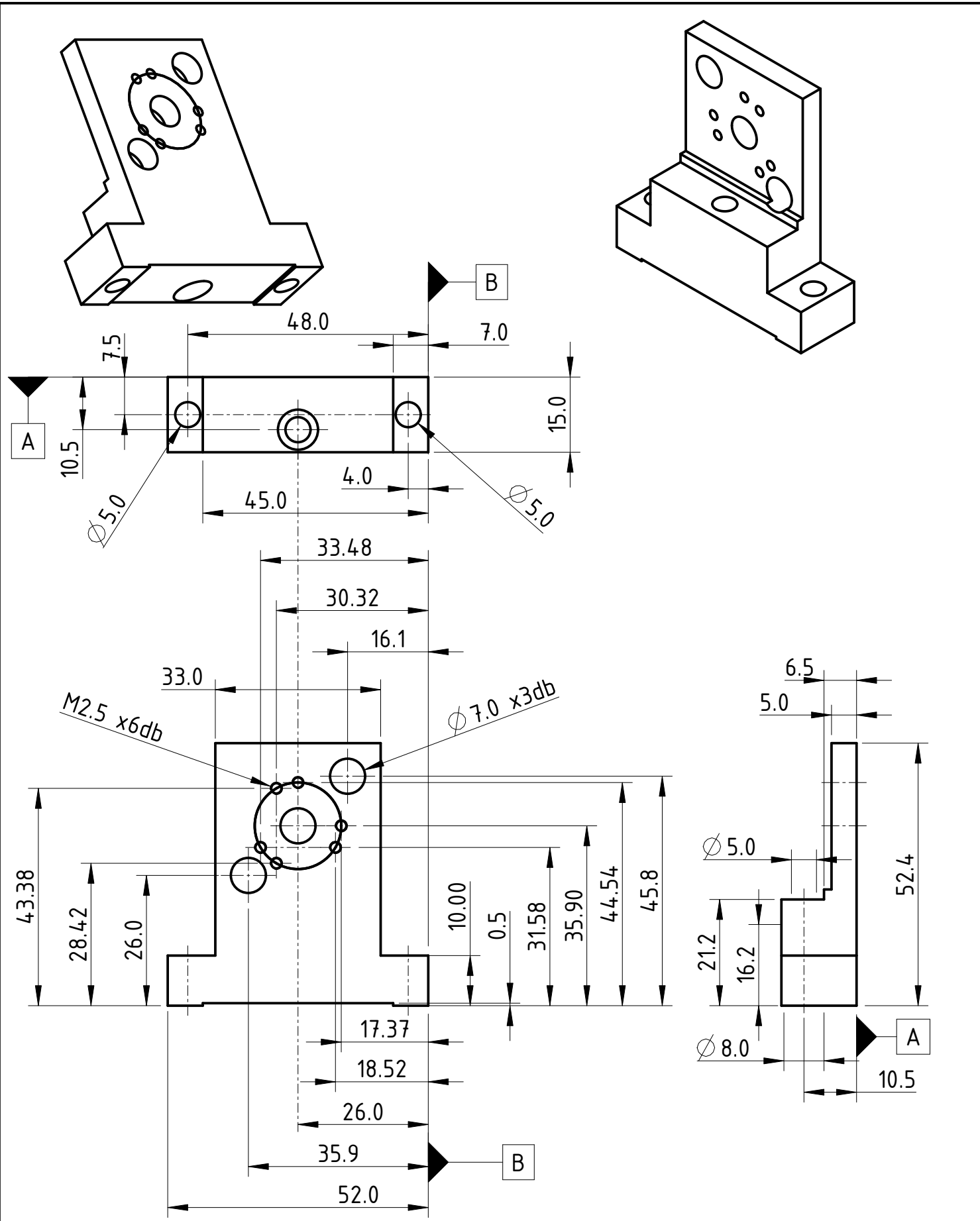


A-A

	Név:	Dátum:	Megnev.: lencse tartó oldal	
Tervező:	?	2020/06/29	Projekt: SPDC szálcsatoló	
Rajzoló:	-	-	Rajzsz.: -	db: 1
Ellenőr:	-	-	M :	Anyag: AlMgSi Oldal: 1/1



	Név:	Dátum:	Megnev.: lencse pár szorító teteje	
Tervező:	?	2009/06/29	Projekt: SPDC szálcsatoló	
Rajzoló:	-	-	Rajzsz.: -	db: 1
Ellenőr:	-	-	M :	Anyag: AlMgSi Oldal: 1/1



	Név:	Dátum:	Megnev.:	PP lemez és szál foglalat tartó
Tervező:	?	2020/06/30	Projekt:	SPDC szálcsatló
Rajzoló:	-	-	Rajzsz.:	-
Ellenőr:	-	-	M :	Anyag: AlMgSi
			db:	4
			Oldal:	1/1